A 449 MHZ MODULAR WIND PROFILER RADAR SYSTEM

by

BRADLEY JAMES LINDSETH

B.S., Washington University in St. Louis, 2002

M.S., Washington University in St. Louis, 2005

A thesis submitted to the

Faculty of the Graduate School of the

University of Colorado in partial fulfillment

of the requirement for the degree of

Doctor of Philosophy

Department of Electrical, Computer, and Energy Engineering

2012

This thesis entitled:

A 449 MHz Modular Wind Profiler Radar System

written by Bradley James Lindseth

has been approved for the Department of Electrical, Computer, and Energy Engineering

_____

Prof. Zoya Popović

_____

Dr. William O.J. Brown

Date_____

The final copy of this thesis has been examined by the signatories, and we

Find that both the content and the form meet acceptable presentation standards

Of scholarly work in the above mentioned discipline.

Lindseth, Bradley James (Ph.D., Electrical Engineering)

A 449 MHz Modular Wind Profiler Radar System

Thesis directed by Professor Zoya Popović and Dr. William O.J. Brown

This thesis presents the design of a 449 MHz radar for wind profiling, with a focus on modularity, antenna sidelobe reduction, and solid-state transmitter design. It is one of the first wind profiler radars to use low-cost LDMOS power amplifiers combined with spaced antennas. The system is portable and designed for 2-3 month deployments. The transmitter power amplifier consists of multiple 1-kW peak power modules which feed 54 antenna elements arranged in a hexagonal array, scalable directly to 126 elements. The power amplifier is operated in pulsed mode with a 10% duty cycle at 63% drain efficiency. The antenna array is designed to have low sidelobes, confirmed by measurements. The radar was operated in Boulder, Colorado and Salt Lake City, Utah. Atmospheric wind vertical and horizontal components at altitudes between 200m and 4km were calculated from the collected atmospheric return signals.

Sidelobe reduction of the antenna array pattern is explored to reduce the effects of ground or sea clutter. Simulations are performed for various shapes of compact clutter fences for the 915-MHz beam-steering Doppler radar and the 449-MHz spaced antenna interferometric radar. It is shown that minimal low-cost hardware modifications to existing compact ground planes of 915-MHz beam-steering radar allow for reduction of sidelobes of up to 5dB. The results obtained on a single beam-steering array are extended to the 449 MHz triple hexagonal array spaced antenna interferometric radar. Cross-correlation, transmit beamwidth, and sidelobe levels are evaluated for various clutter fence configurations and array spacings. The resulting sidelobes are as much as 10 dB below those without a clutter fence and can be incorporated into existing and future 915 and 449 MHz wind profiler systems with minimal hardware modifications.

Dedication

To May Britt, Mom, Dad, and Ashlea.

Acknowlegements

Special thanks go to Professor Zoya Popovic for encouraging me to continue graduate school, welcoming me into the Microwave and RF Research Group, and supporting my efforts to improve wind profiler radars. Dr. Bill Brown at NCAR deserves many thanks for supporting my effort to finish graduate school and for numerous discussions about wind profiler radar strategies. Thanks to Dr. John Kitching at NIST for giving me the initial opportunity to come to CU and work on magnetometers. Thanks to Dr. Nestor Lopez (now at MIT Lincoln Laboratory) for much advice during my first amplifier prototypes. My committee members Professor Gasiewski, Professor Thayer, and Professor Palo deserve thanks for their feedback and constructive criticism.

I wish to thank Warner Ecklund, Jim Jordan, and Dan Law at NOAA, Terry Hock, Steve Cohn, Charlie Martin, Lou Verstraete, Jennifer Standridge, and Tim Lim at NCAR, and also Mike Roberg and John Hoversten at CU, for suggestions on the 449 MHz wind profiler project. Many others deserve thanks for their help including Alan Brannon, Vishal Shah, Matt Eardley, Luke Sankey, Mike Elsbury, Erez Falkenstein, Frank Trang, Dan Kuester, and Rohit Sammeta. Thanks to all of the past and present members of the CU Microwave and RF research group for their friendship and help.

I also want to thank Leo Hollberg, Peter Schwindt and Ying-Ju Wang all formerly at NIST for their discussions on magnetometer operation. The Chip Scale Atomic Magnetometer work was done with Peter Schwindt, Svenja Knappe, and John Kitching at NIST.

Contents

Chapter 1

Introduction

1.1 The Atmosphere and Atmospheric Measurements

This topic of this thesis is a 449 MHz radar system for atmospheric wind profiling. Wind profiler radars are used to observe the horizontal and vertical wind direction and velocity from ground level up to an altitude of 10-15 km depending on the system characteristics. Figure 1.1 shows the altitudes of various layers of the atmosphere. The jet stream is typically between 7-16 km. The planetary boundary layer is the lowest part of the atmosphere and it is influenced by the Earth surface. Boundary layer wind profilers typically observe winds in the atmosphere between 0-4 km.

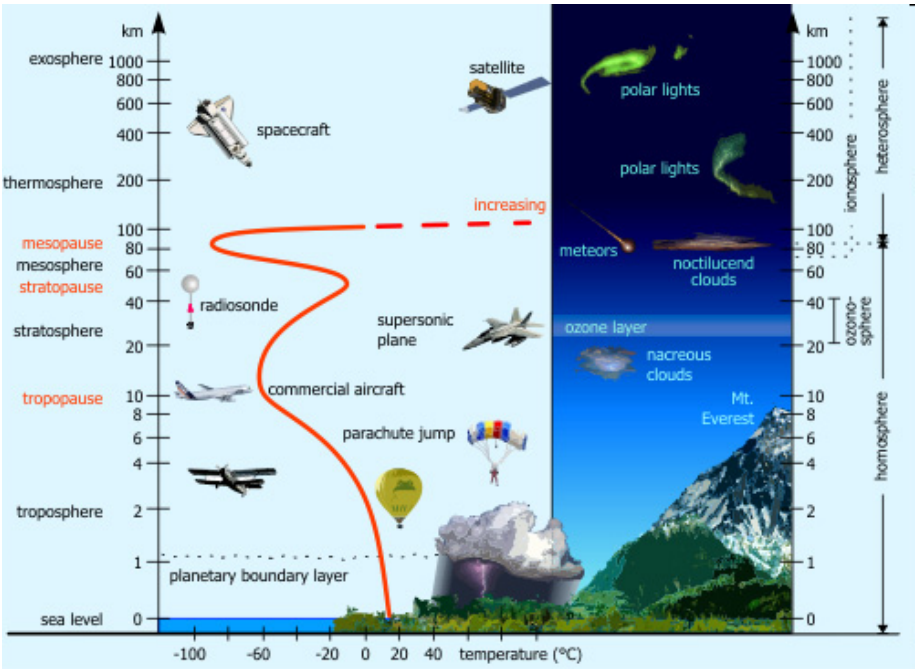

Figure 1.1. The Earth atmosphere with labeled altitudes and typical temperatures [1].

Wind profilers primarily observe horizontal winds at every altitude within their range. Large permanent wind profilers at 50 MHz and 449 MHz can observe winds up to about 17 km. An example of wind profiler data is given in Figure 1.2.

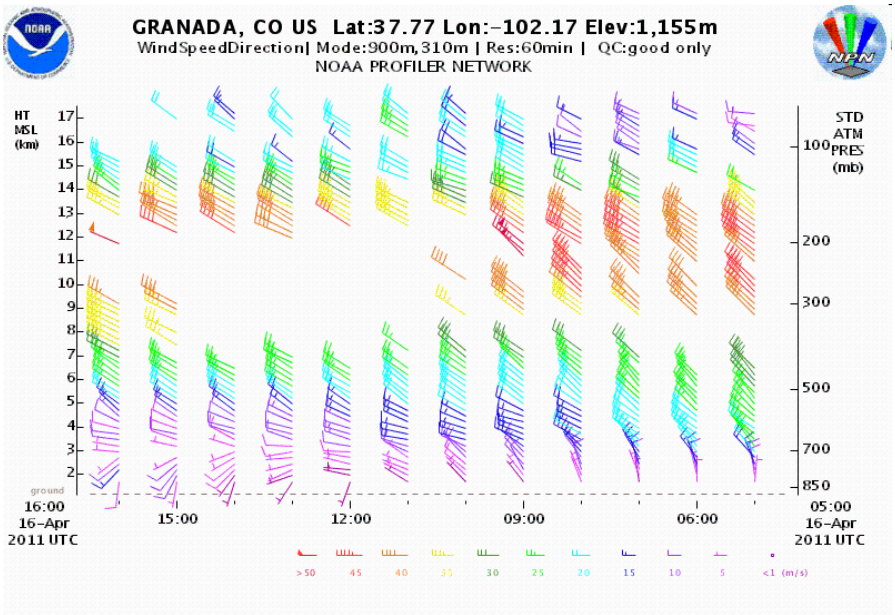

Figure 1.2. Example of wind profiler data from the Granada, Colorado station of the NOAA National Profiler Network.

This data is provided by the NOAA National Profiler Network which consists of about 20 permanent wind profiler installations. The data is displayed in a plot of altitude in km vs. time in hours for April 16, 2011 at the Granada, Colorado station in southeast Colorado. The horizontal wind data at each altitude is displayed as a wind barb. The wind velocity is indicated by the color code and also by the number of segments at the end of the barb. For example, red barbs are 45 m/s, blue barbs are 15 m/s. Figure 1.3 shows an example wind barb. This example wind barb shows a 15 m/s wind from the Northeast. The tail of the barb indicates the direction the wind is coming from.

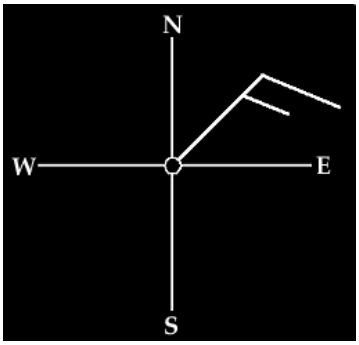

Figure 1.3. Example of a wind barb showing a 15 m/s wind from the Northeast.

Uses for wind profiler data include improving forecast models, improving climate models, and air pollution studies. An example of wind profiler data use is given in Figure 1.4 from Benjamin et al.[2]. The figure shows a three hour precipitation forecast using the Rapid Update Cycle (RUC) model over the Kansas and Oklahoma area between 03-06UT on 9 Feb 2001. On the left is the forecast model run with wind profiler and on the right is without wind profiler data. The color scale indicates precipitation in mm. There is a significant difference of about 5 mm in forecasted precipitation in some areas of Kansas and Oklahoma.

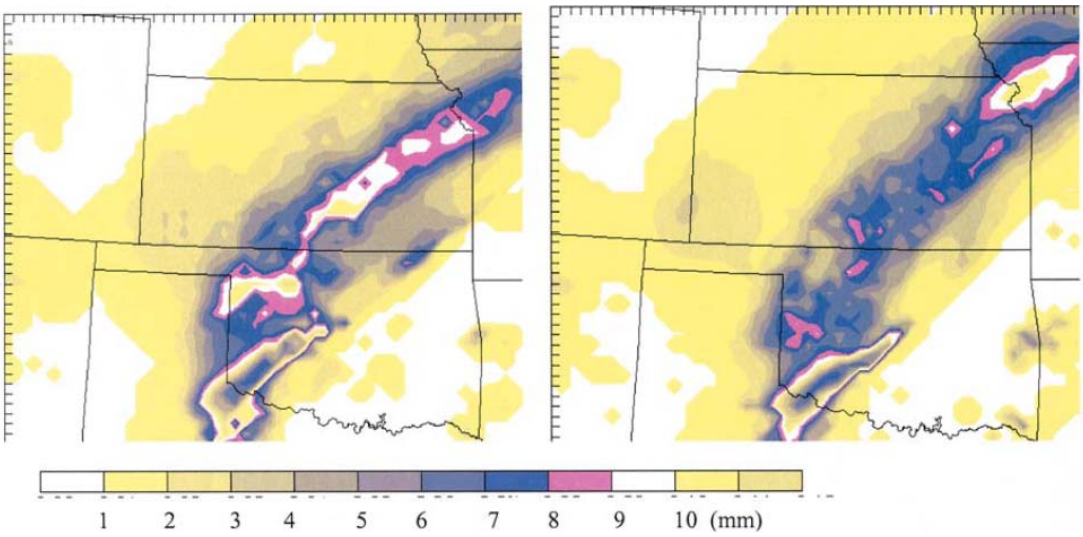

Figure 1.4. Rapid Update Cycle (RUC) 3h precipitation forecast run with profiler data (left) and without (right), 03-06 UT, 9 Feb 2001 [2]

The basic atmospheric measurements that can be recorded by any instrument are temperature, pressure, humidity, precipitation, and wind. The gold standard for measuring these parameters is the radiosonde, which most people know as the weather balloon, Figure 1.5. There is a worldwide network of stations that launch at least one or two radiosondes per day. The radiosonde has pressure, temperature, and humidity sensors contained in an instrument package attached to the balloon. Since the horizontal velocity of the balloon is equal to the wind speed, a GPS receiver within the instrument package allows computation of the horizontal winds at each altitude. This method is labor and resource intensive however, and does not provide a continuous profile like wind profiler radar.

Figure 1.5. The author launching a radiosonde aboard the R/V Roger Revelle in the Indian Ocean as part of the DYNAMO project.

1.2 Existing Atmospheric Radars and Principles

The most common weather radar in the United States is the WSR-88D NEXRAD Radar. It operates in the 2.7-3.0 GHz band with a 750 kW transmit power. The radar scans in azimuth from 0-20 degrees in elevation. The target for this radar is Rayleigh scatter from precipitation. The return signal for a NEXRAD radar is 30-40 dB above that of clear air winds. Probably 90% of the atmospheric radar data the public sees is of this type. Figure 1.6 shows a picture of a NEXRAD radar tower and a map of base reflectivity of a Colorado storm in April 2011.

The most common wind profiler radars are similar to the Vaisala LAP-3000. This radar operates at 915 MHz, with a 500W transmit power using a 2m x 2m square patch array. This radar can detect winds from 120m to 4km. The major users of this system are NOAA, the FAA, airports, and air pollution organizations. This system commonly includes a clutter fence and a Radio Acoustic Sounding System (RASS). A picture of this system is shown in Figure 1.7.

The existing wind profiler systems at NCAR consist of three deployable boundary layer 915 MHz wind profilers shown in Figure 1.8. These portable systems provide winds up to about 3km, with 60-100m height resolution and 30

minute time resolution. The wind profiler radars are part of a larger deployable instrument called the Integrated Sounding System, first described by Parsons et al. [98] which includes a GPS-based radiosonde station and a surface meteorological station. The existing Multiple Antenna Profiler Radar (MAPR) uses a spaced antenna method for detecting horizontal winds. This system is capable of 1 minute time resolution because the radar beam is focused in a single location. The Mobile Integrated Sounding System (MISS), is capable of rapid deployment with only a 1 hour setup time.

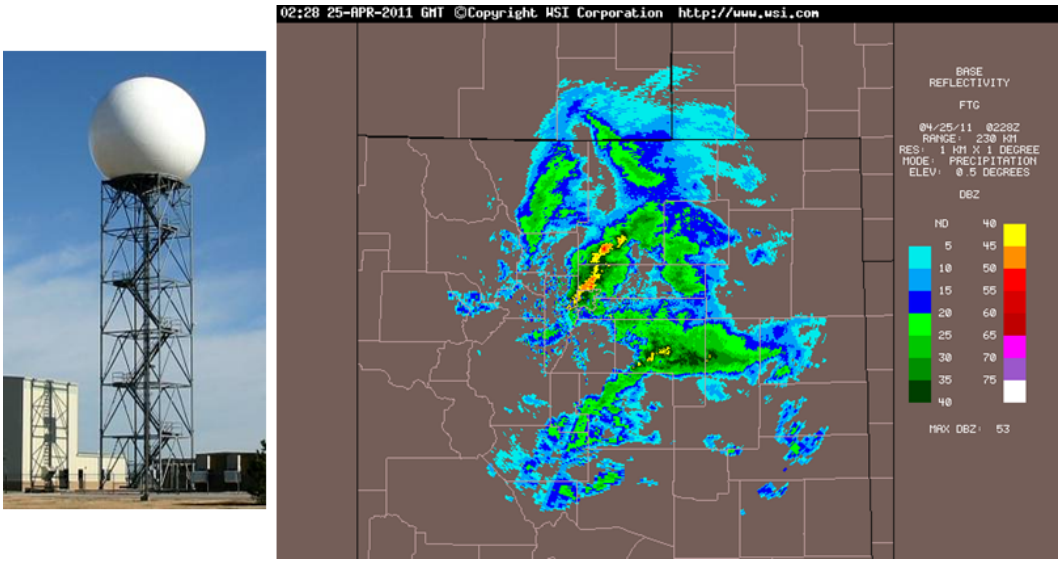

Figure 1.6. NEXRAD radar. Left: tower with radome. Right: map of base reflectivity of a Colorado storm in April 2011.

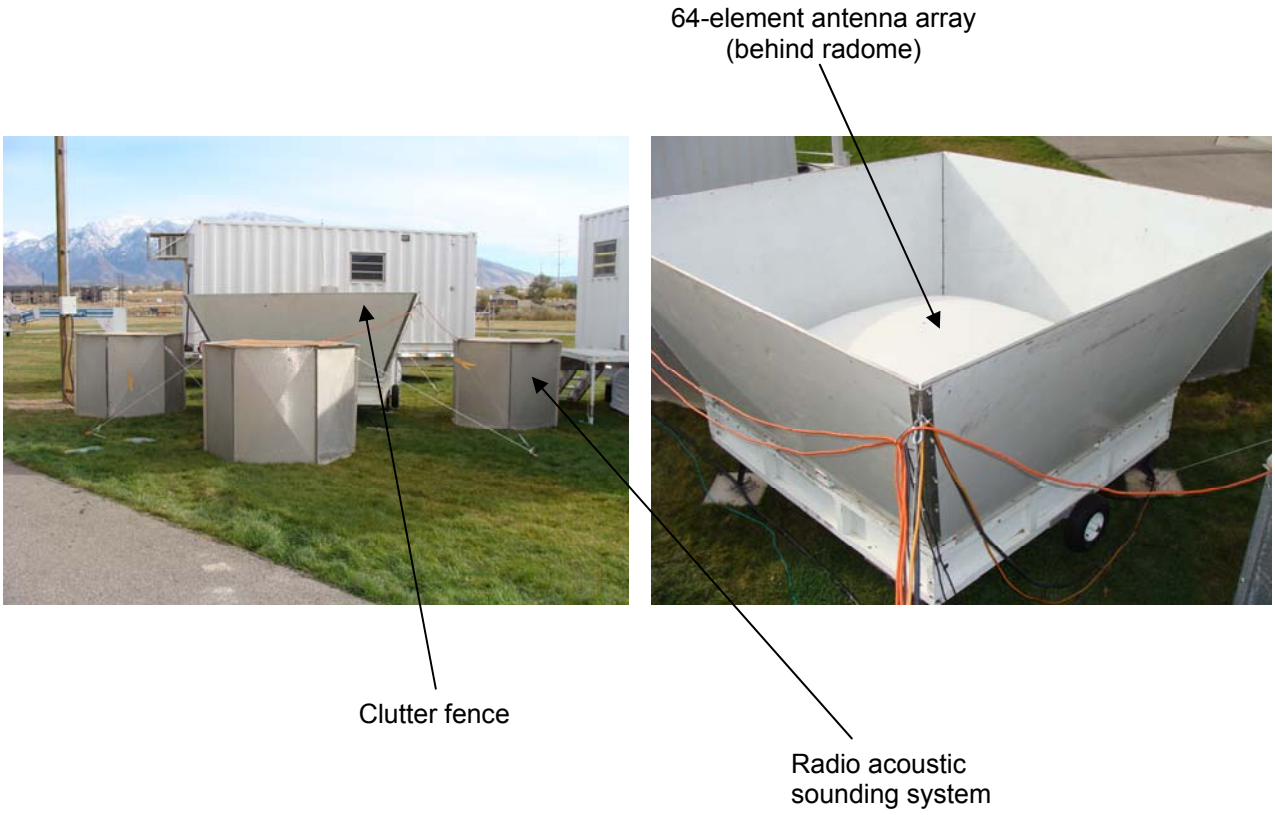

Figure 1.7. The most common wind profiler radar which is used to observe the boundary layer. This radar operates at 915 MHz with a transmit power of 500W and a 2m x 2m square patch antenna array.

(a)

(b)

(c)

Figure 1.8. Existing wind profiler radars at NCAR. All of the existing systems operate at 915 MHz. (a) The Mobile Integrated Sounding System (MISS). (b) The Multiple Antenna Profiler Radar (MAPR) uses the spaced antenna method. (c) The Integrated Sounding System (ISS).

The primary target of a wind profiler radar is atmospheric turbulence. An illustration of atmospheric turbulence eddies is given in Figure 1.9. Energy is fed into the turbulent eddies at the outer scale (~1 – 100 m), L_o. When eddies become less than the inner scale l_v (~1 cm) viscosity becomes significant and the energy is dissipated into heat [3-4,99]. The inner scale becomes larger with colder temperatures (air is more viscous).

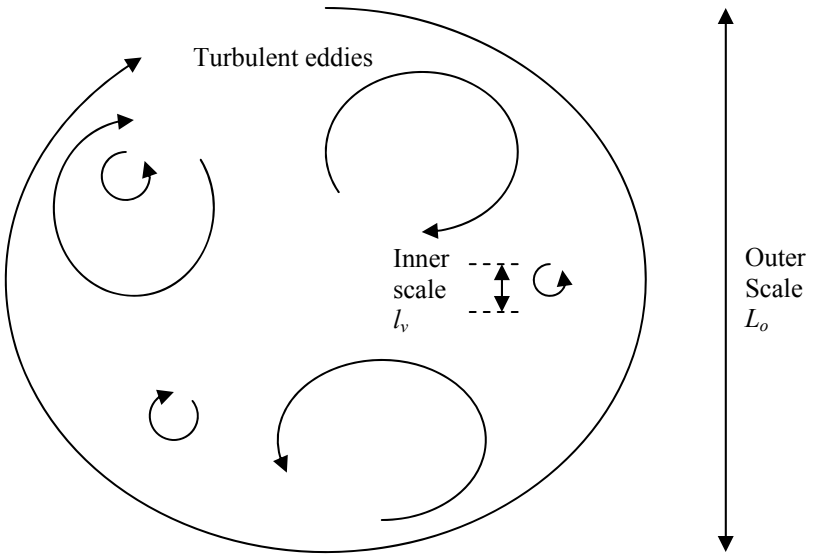

Figure 1.9. Diagram of atmospheric turbulence eddies illustrating the inner scale and the outer scale [3-4].

Bragg scatter occurs when refractive index gradients with a size of half of the radar wavelength will scatter with constructive interference as illustrated in Figure 1.10. Because λ=66 cm, we are most sensitive to the 33 cm scale. For the 915 MHz wind profilers λ/2 is 16cm (getting close to inner scale). Because the inner scale becomes larger with colder temperatures, longer wavelength 449 or 50 MHz radars will work better in cold conditions.

The atmospheric refractive index determines the degree to which scatter will be produced by a turbulent eddy. Atmospheric refractive index is given by [3,100]:

$$n = 1 + \frac{77.6 \times 10^{-6} p}{T} + \frac{.373e}{T^2} - \frac{N_e}{2N_c}$$

Where p is the atmospheric pressure in millibars, T is the temperature in K, e is the partial pressure of water vapor in millibars, N_e is the number density of electrons, N_c is the critical plasma density (N_e/N_c is only significant above 50 km). The term on the left is called the dry term and the term on the right is the wet term. Table 1.1 gives example

values of these parameters. Figure 1.11 shows how a single turbulence eddy forms a refractive index gradient. Note that volume Bragg scatter is not sensitive to polarization, so the orientation of the antenna polarization with respect to the prevailing winds is not an issue.

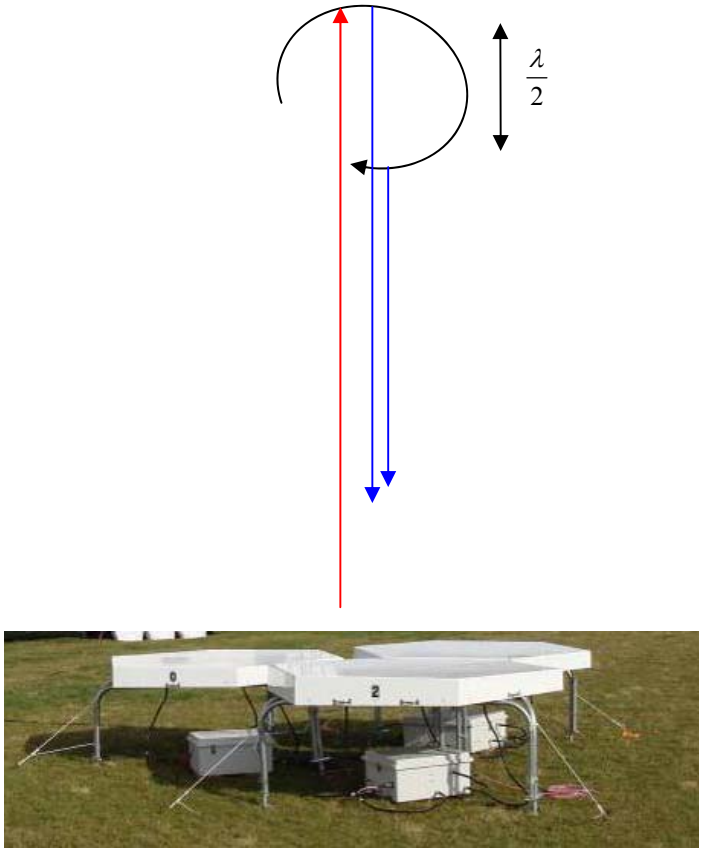

Figure 1.10. Diagram of a single turbulent eddy illustrating Bragg scatter at the distance of half a wavelength.

Table 1.1: Example values for parameters in the atmospheric refractive index equation

Parameter	Example value
T	290K
p	1013 mb
e	10.2 mb
n	1.0003 (sea level), 1.00026 (1 km)

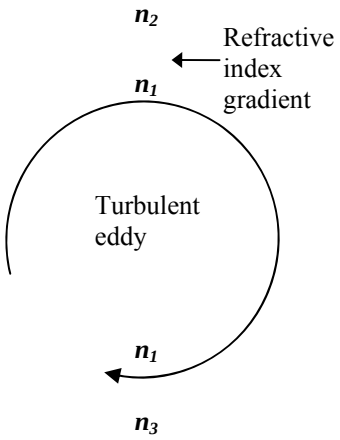

Figure 1.11. Diagram illustrating how a single turbulent eddy forms a refractive index gradient.

Another consideration is how strong the backscatter signal from wind will be relative to backscatter from precipitation. In general, with higher frequency, wind profilers become more sensitive to precipitation. Figure 1.12 from Ralph [23] shows this relationship. Bragg scatter is only weakly dependent on wavelength ($\lambda^{-1/3}$), but Rayleigh scatter from precipitation is strongly dependent on wavelength (λ^{-4}).

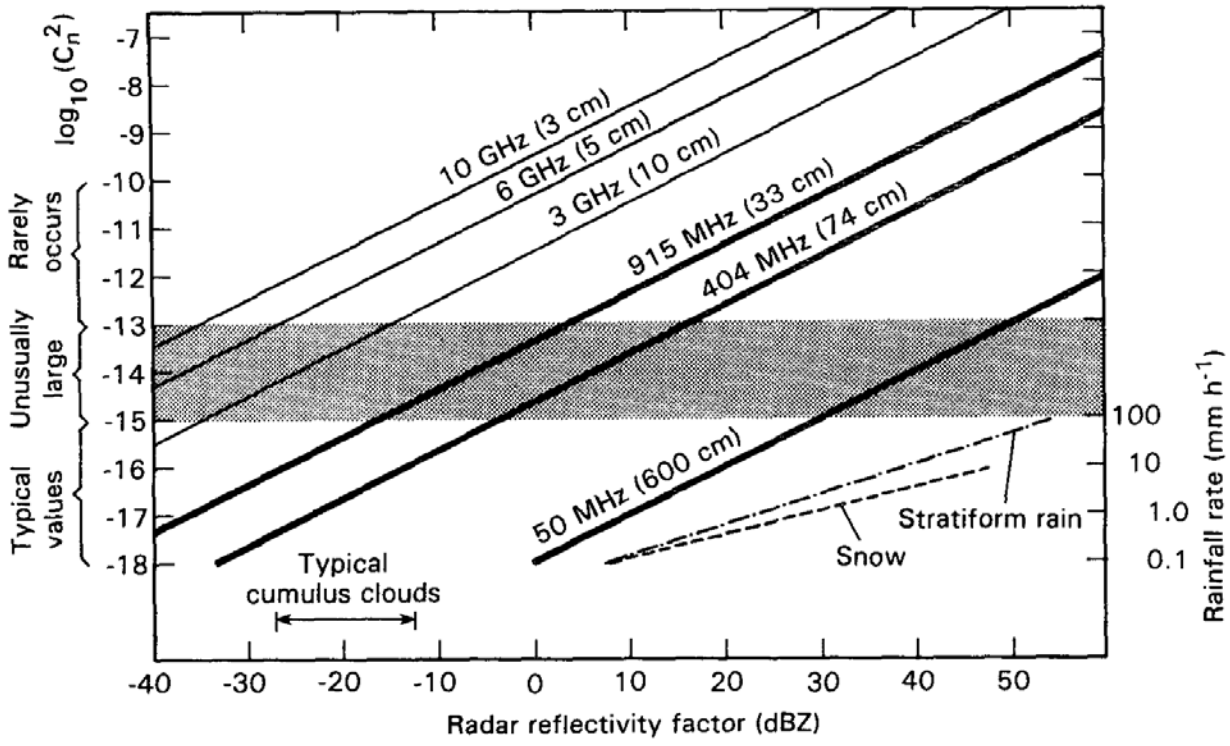

Figure 1.12. Relative level of precipitation backscatter vs. turbulence backscatter from winds from Ralph [23]. Solid lines show the amount of Bragg scatter that is equivalent to a given amount of Rayleigh scatter.

Figure 1.12 shows that for a C_n^2 aof about 10-15, the Bragg scatter signal will be equivalent to a -10 dBZ precipitation signal at 915 MHz, while at 404 MHz the Bragg scatter signal will be equivalent to a 0 dBZ precipitation signal. A conversion between rainfall rate and dBZ is also shown on the chart. This means that at 915 MHz the precipitation signal will be stronger and could make the Bragg scatter signal more difficult to detect than at 404 or 449 MHz.

The spatial variation of the refractive index gradient contributes directly to system Signal to Noise Ratio (SNR). SNR for wind profilers has been well studied [5]. The single pulse radar equation for SNR for Bragg scatter from a clear air target can be written as:

$$SNR = \frac{0.21 P_t \varepsilon_a A \Delta R^2}{4\lambda^{1/3} \pi c R^2 L k T_{sys}} C_n^2 \propto P_t A_e$$

$$\varepsilon_a A = A_e = \frac{G\lambda^2}{4\pi}$$

Where P_t is the transmitted power, ε_a is the aperture efficiency, A is the area of the antenna, ΔR is the range resolution, R is the range to the target, L is cable losses, T_{sys} is the system noise temperature, and C_n^2 is the refractive index structure parameter. It can be seen from the equation that going from 915 MHz to 449 MHz, we get 4 times the signal for an antenna with the same gain.

About 90% of wind profilers use a technique called Doppler Beam Steering [6]. An actively phased array or three antennas pointed in different directions can be used for this method. Figure 1.12(a) shows a diagram of a phased array wind profiler illustrating the three beams necessary to obtain a horizontal wind vector at each altitude. Wind profilers traditionally use a “high mode” with a long pulse for higher altitude coverage and a “low mode” with a short pulse for lower coverage with better height resolution. Figure 1.12(b) shows a picture of a Degreane Horizon wind profiler that uses three separate antenna arrays to observe the horizontal wind vector. This method allows for a simpler hardware design with no phase shifters, but with a larger overall system size.

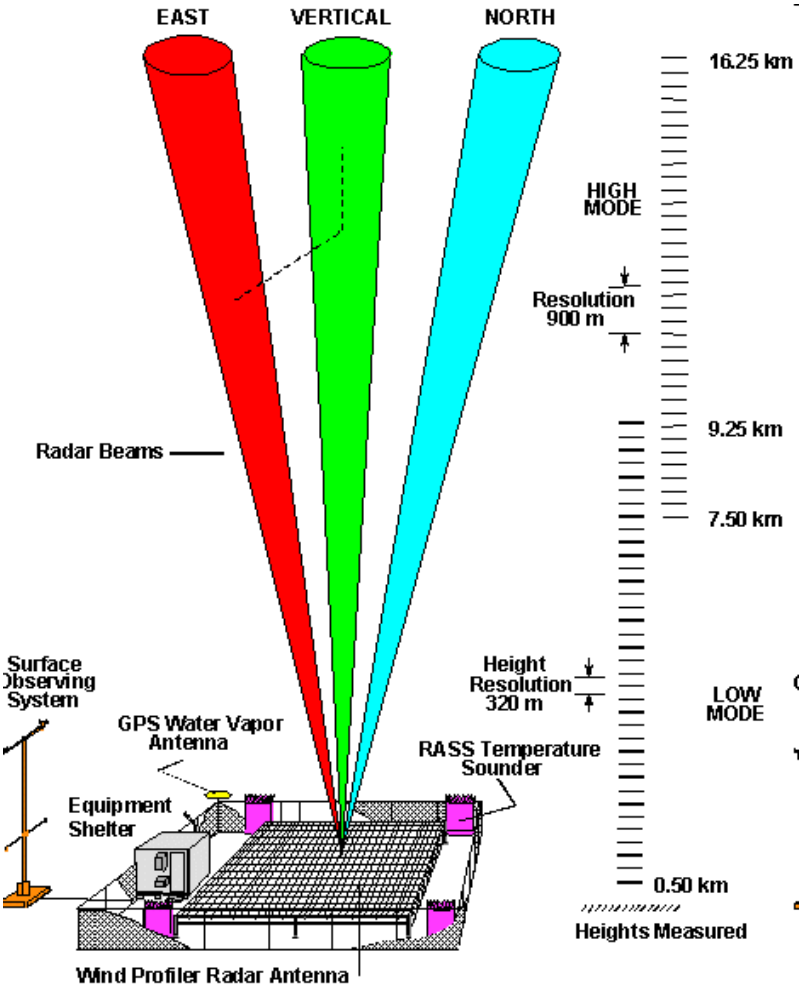

(a)

(b)

Figure 1.12. An illustration of Doppler Beam Steering (DBS) operation of a wind profiler radar. (a) The phased array points the beam in three different directions [6]. (b) Three different antennas are oriented in three different directions [7].

For the Doppler Beam Steering systems, the horizontal wind velocity is computed at each altitude. Referring to Figure 1.13 from Vaisala, Inc. [8], the equations for determining velocity are below. Where $w = -V_z$ is the vertical velocity determined directly from the Doppler shift of the vertical beam. u is the horizontal velocity in the x direction, and v is the horizontal velocity in the y direction.

$$u = -\left[\frac{V_x - V_z \sin\theta_x}{\cos\theta_x}\sin\theta_x\right] - \left[\frac{V_y - V_z \sin\theta_y}{\cos\theta_y}\sin\theta_y\right]$$

$$v = -\left[\frac{V_x - V_z \sin\theta_x}{\cos\theta_x}\cos\theta_x\right] - \left[\frac{V_y - V_z \sin\theta_y}{\cos\theta_y}\cos\theta_y\right]$$

$$w = -V_z$$

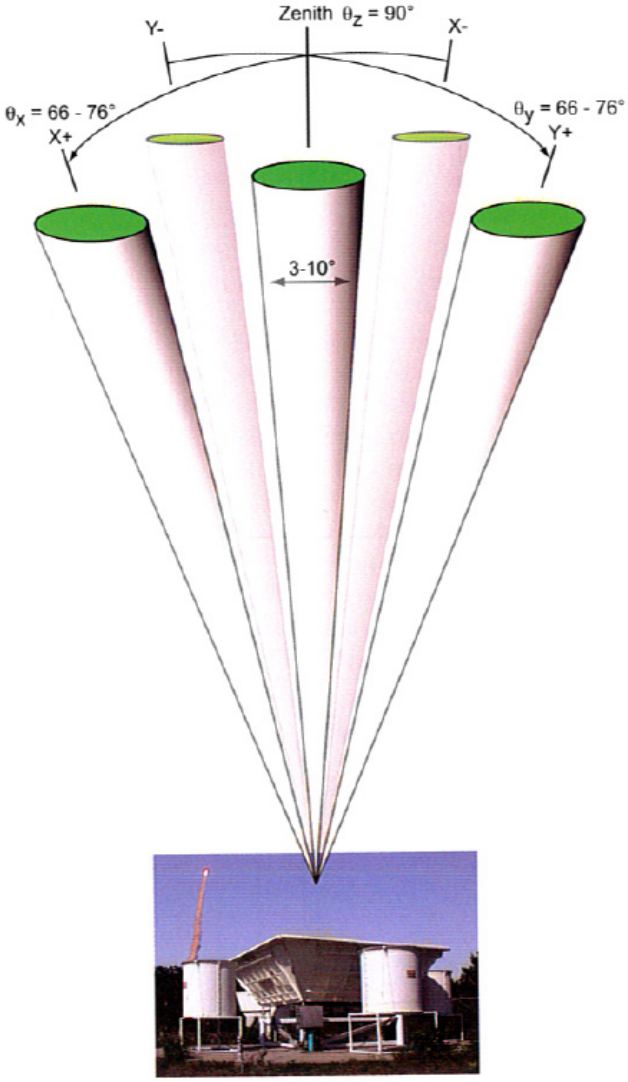

Figure 1.13. Doppler Beam Steering (DBS) horizontal wind computation [8].

The spaced antenna method is another method of wind profiler radar which involves 3 or more spaced receivers. The horizontal winds are calculated using cross-correlation between the signals from each of the receivers. The spaced antenna method is good for rapidly changing conditions like fronts and atmospheric gravity waves. The antennas always point at zenith, which has the benefit of not requiring phase shifters. Figure 1.14 from Cohn et al. shows Bragg scatter over 4 spaced receivers like the MAPR system [9,101].

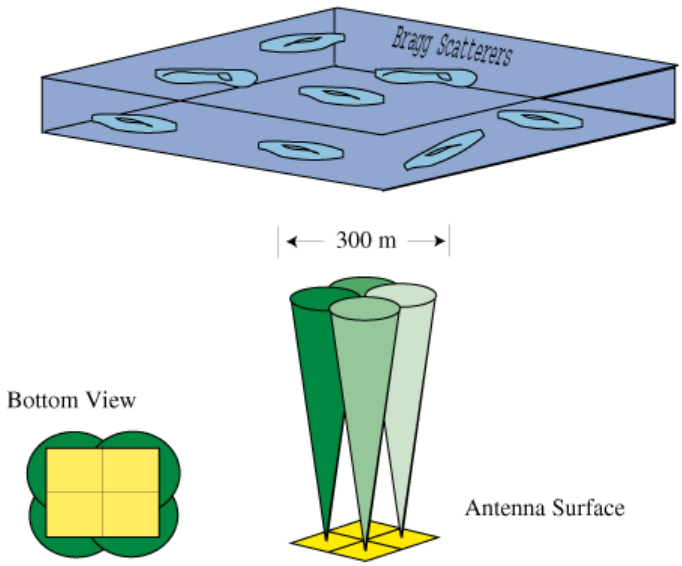

Figure 1.14. An illustration of spaced antenna (SA) operation of a wind profiler radar. Four spaced receivers are able to observe the horizontal wind as in the MAPR system from Cohn et al.[9,101].

Each receiver receives a time series of backscattered signals that is delayed in proportion to the velocity. Cross-correlations are computed between each receiver signal. Since the distance between receivers is known, the time lag between receiver pairs allows computation of the horizontal wind velocity. Figure 1.15 shows all baselines of the MAPR system and an example of the time lag between receivers.

To provide a historical background to wind profiler radar, early experiments demonstrating profiling of atmospheric winds will be reviewed. One of the earliest measurements of atmospheric winds was at the Jicamarca Radar in Peru, Figure 1.16 [102]. This radar was originally built for ionospheric studies in the 1960s. It operates at 50 MHz with a transmit power of 1.5 MW and an array of 18,432 dipoles with a size of 288 x 288m. In 1974, one of the first spaced antenna studies of atmospheric winds between 20-80 km in altitude was published using data from this radar [10]. The array is separated into subarrays for spaced antenna operation. Since the intended target at

Jicamarca is much higher than a boundary layer wind profiler, the location inside a mountain valley provides natural protection from clutter.

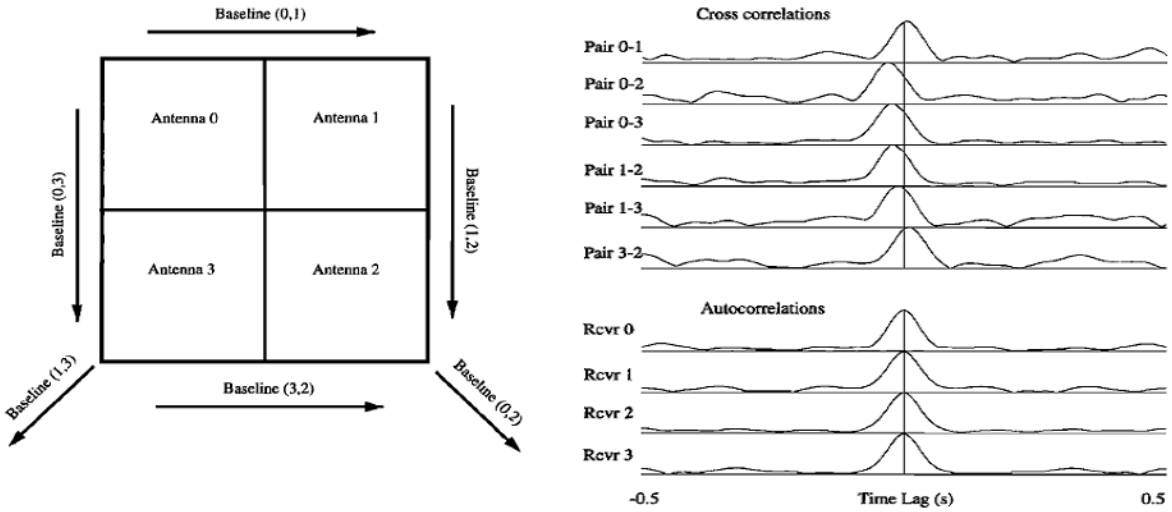

Figure 1.15. A spaced antenna radar with at least three baselines will allow cross-correlation to determine the horizontal wind vector. Left: Six independent baselines of the MAPR system. Right: Spaced antenna cross-correlations illustrating time lag between receivers. From Cohn et al. [9].

Figure 1.16. Jicamarca radar in Peru. The dimensions of the 18,432 element array are 288 x 288m [102].

Arecibo Observatory in Puerto Rico was also built in the 1960s for ionospheric studies. In 1979 a study was published of wind measurements at altitudes between 5-20 km [11]. This study used the Doppler Beam Steering technique. For this study, the radar was operated at 430 MHz, with a transmit power of 1.8 MW. As shown in Figure 1.17, the dish has a diameter of 308 m and a feed that can be rotated to steer the beam.

1.3 Atmospheric Radar Experiments at Arecibo Observatory

A brief mention of work at Arecibo Observatory will be made here. This work was part of the 2004 Polar Aeronomy and Radio Science Summer School. In 2004, observations were made of meteors and E-region electron density at the Arecibo Observatory using the 430 MHz radar with the line feed. The radar was configured to use a Barker code, and observations were made at ranges from 60 to 140 km. Figure 1.18 is a plot of altitude vs. time showing a return from a single meteor with a short duration of less than 0.05 sec. This meteor was observed on August 19, 2004 at 05:15:24 Atlantic Standard Time (AST).

Figure 1.19 shows data from a number of meteors. This data was collected from 05:14-05:27 AST. As shown in the data, most meteors observed have a velocity of 40-70 km/s and are found at an altitude of about 105-110 km. In general, observed velocities are lower at lower altitudes because of drag from the atmosphere.

Figure 1.17. Arecibo Observatory in Puerto Rico. Left: The author touring the feed of the radar in 2004. Right: Picture of the dish, feed, and observatory complex. The dish is 308m in diameter.

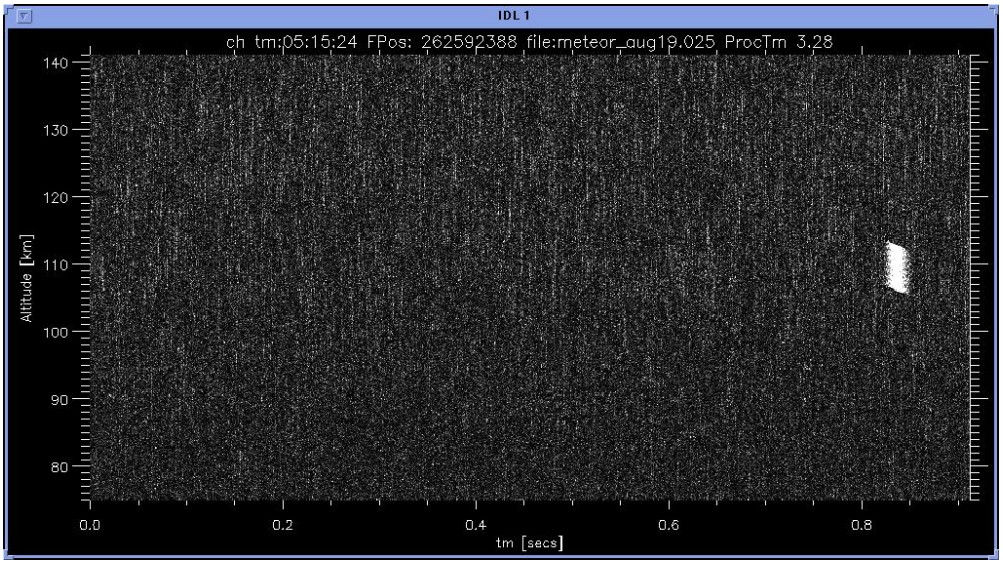

Figure 1.18. Plot of altitude vs. time showing a return from a single meteor at Arecibo Observatory.

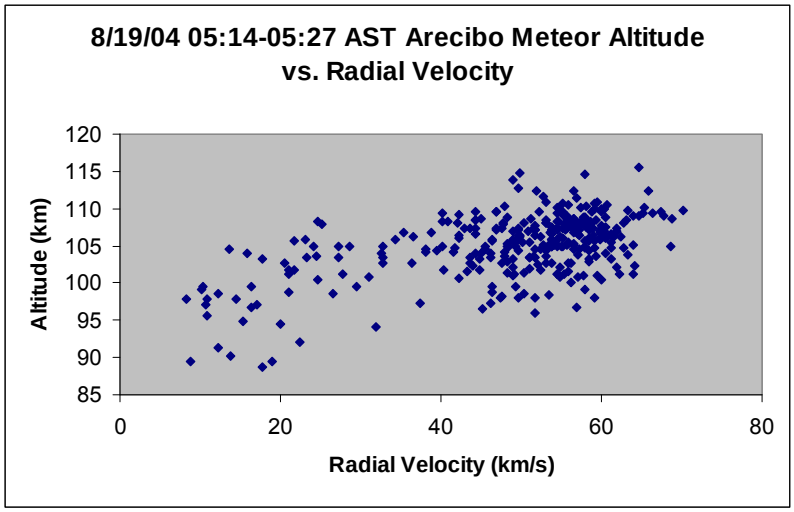

Figure 1.19. Plot of altitude vs. radial velocity of a number of meteors observed during 13 minutes of observation time.

Also observed later in the day was E-region electron density, shown in Figure 1.20. The solar wind pushes this layer towards the earth during the daytime, limiting radio wave propagation. During nighttime the solar wind pushes this layer further away from the earth thereby enhancing radio wave propagation. This layer is seen in the data at a range of 100-120 km but moved above the observation range about 18:00 AST. Some interference can be seen in the data. Interference mitigation for a radar with an antenna this size would need to be done in software. Changes to the antenna for this size of radar would be a major project.

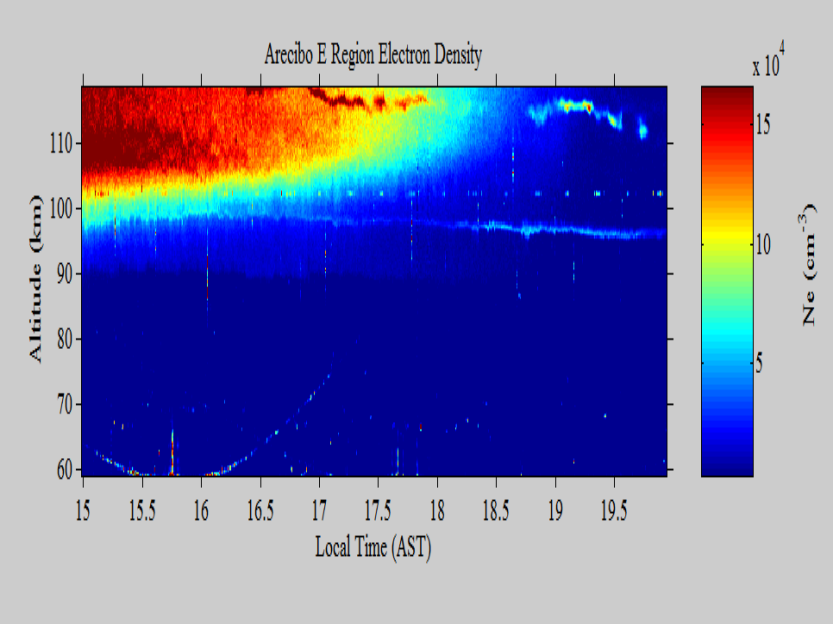

Figure 1.20. Plot of altitude vs. time showing E-region electron density and the transition from daytime into nighttime between 17-18 AST.

1.4 Other Significant Wind Profiler Radars

Another significant radar that influenced wind profiling is the MU (Middle and Upper Atmosphere) Radar in Japan that was built in 1984, Figure 1.21 [12]. This radar operates at 46.5 MHz, with a 1 MW peak power, 475 crossed Yagi antennas, and an overall diameter of 103m. This radar is reconfigurable and can be operated in either a DBS or a spaced antenna mode. There are earth berms and metal fences to prevent interference from clutter.

Figure 1.21. MU Radar in Japan. Built in 1984 and has a 103m overall diameter. Note the presence of an earth berm and metal fence for clutter reduction.

The University of Massachusetts Turbulent Eddy Profiler was a 915 MHz bistatic wind profiler with a 25 kW peak power that used a horn antenna for transmit and a hexagonal array of patch antennas for receive [13]. This profiler focused on imaging of the atmosphere. The first wind studies using this radar were published in 1998. It could use both the spaced antenna method or a receiver DBS method. To accomplish DBS, the receiver beam was steered. Figure 1.22 shows a diagram of this system from Mead et al.[13].

NOAA developed the Ronald Brown Wind Profiler in 2000. As shown in Figure 1.23 from Law et al., this radar uses a hexagonal phased array antenna design with a single 500W transmitter and the Doppler Beam Steering method [14]. This system is one of the few wind profiler radars that are deployed on a ship. In addition to beam steering, the electronic phase shifting system stabilized the beam to compensate for the motion of the ship. Using a wind profiler radar on a ship presents additional difficulties because moving waves in the ocean cause a high clutter environment.

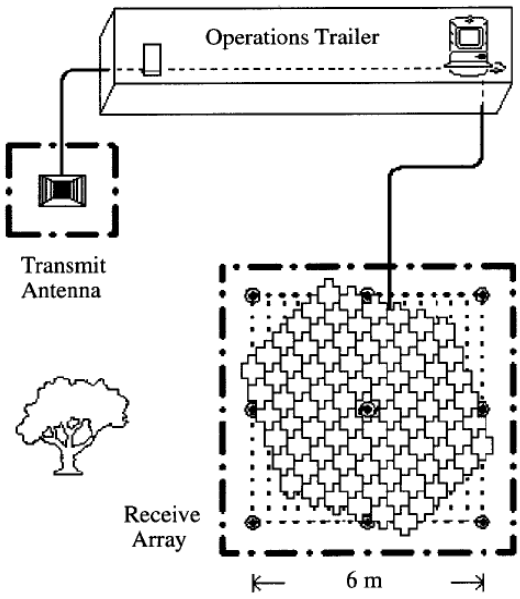

Figure 1.22. The UMass Turbulent Eddy Profiler. A bistatic radar with a modular hexagonal receive array from Mead et al.[13].

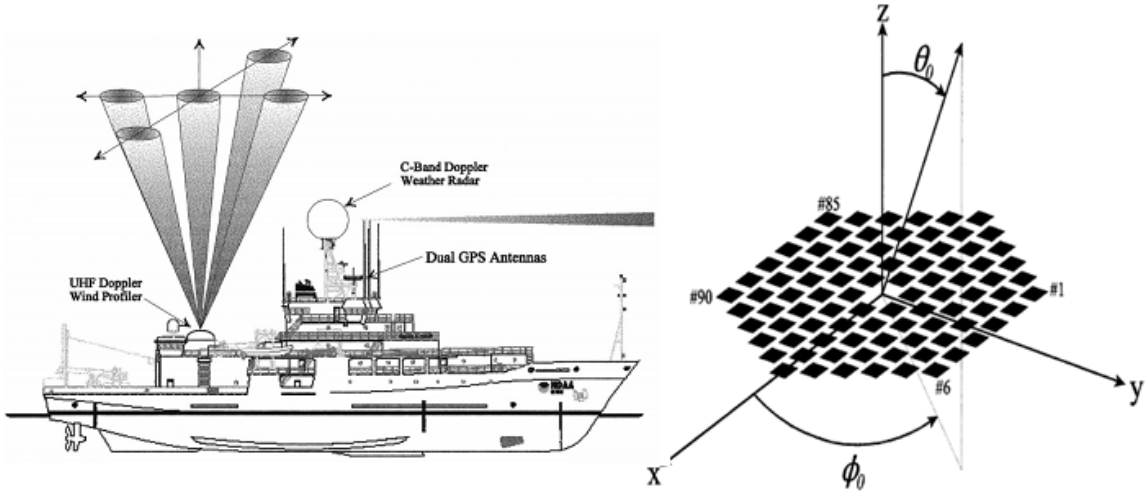

Figure 1.23. The NOAA Ronald Brown Wind Profiler. This is a ship-based wind profiler. Left: Position of the wind profiler on the ship. Right: Diagram of the 90 element 915 MHz patch antenna array from Law et al.[14].

1.5 Thesis Outline and Contributions

The previous sections presented an introduction to atmospheric measurements and existing atmospheric radars. This section gives an overview of each of the following chapters in the thesis.

Chapter 2 describes the 449 MHz modular wind profiler system design, the spaced antenna wind computation algorithm, and the first wind measurements taken by the system. The receiver is analyzed for adequate sensitivity and the architecture for the transmitter is presented. A 54% efficient 1 kW (peak, 10% duty cycle) UHF power amplifier with a 54 cents/Watt transistor cost is presented. These amplifiers were used successfully at the Persistent Cold-Air Pool Study (PCAPS) field project at Salt Lake City, Utah in Winter 2010-2011. The 449 MHz radar wind measurements are compared with wind measurements from a 915 MHz radar located at the same site. The goals of the work in this chapter include:

- System design of the 449 MHz modular wind profiler radar;
- Receiver sensitivity analysis and noise figure measurement;
- Spaced antenna horizontal wind computation;
- Transmitter architecture design;
- Radar spectral emissions measurements;
- Comparison of 915 and 449 MHz radar performance; and
- Observation of a persistent cold-air pool event at Salt Lake City, Utah.

Chapter 3 presents wind profiler radar observations during three different field projects using the 915 MHz MAPR and DBS wind profiler radars. The first project presented is the Cloud and Precipitation Study (CPS) south of Miami, Florida in late summer 2008 using the 915 MHz spaced antenna MAPR system. Profiling of Winter Storms (PLOWS) is the next project that took place in Winter 2009-2010 in the Midwest United States using a mobile 915 MHz DBS wind profiler (MISS). The most recent field project is the Dynamics of the Madden-Julian Oscillation Project (DYNAMO) located south of Sri Lanka in the Indian Ocean using a ship-based 915 MHz DBS wind profiler. The goals of this chapter in terms of the thesis are:

- Demonstrate the need for higher altitude wind measurement capability than the current 915 MHz MAPR system;

- Show observation of a rain band during tropical storm Fay with the 915 MHz MAPR system;
- Show the effects of sea clutter on ship-based 915 MHz DBS wind profiler data; and
- Motivate the need for clutter mitigation with the mobile 915 MHz DBS wind profiler (MISS) and on the ship-based 915 MHz DBS system.

Because of the effects of clutter on wind profiler data quality, antenna sidelobe reduction strategies are presented in Chapter 4. A full-wave electromagnetic field simulation is presented for the existing 915 MHz antenna with a clutter fence and edge treatments. The clutter fence concept is applied to the new 449 MHz hexagonal array and simulations are performed to evaluate its performance. Sidelobe levels are simulated while the height of the array is varied above a simulated earth (soil) ground. Transmit sidelobe levels and receiver signal cross-correlation are also evaluated while changing edge to edge spacing of the three hexagonal arrays.

Also presented is the spaced antenna array architecture, including design, analysis, and initial measurements of the first 449 MHz circular patch antenna arrays built for this system. Simulations using Matlab and Ansoft HFSS are presented along with measurements taken on the prototype antenna arrays. The goals of the work in this chapter are as follows:

- Evaluate clutter fence and height above ground techniques for antenna sidelobe reduction;
- Verification of individual circular patch antenna performance;
- Initial simulation of antenna array sidelobe levels using element pattern and array factor computation;
- Measurement of near-horizon sidelobe levels for an 18-element hexagonal array;
- Simulate effect of hexagonal array spacing on receiver signal cross-correlation and transmit antenna sidelobe levels; and
- Determine optimum hexagonal array spacing.

Chapter 5 presents a new 63% efficient, 2.5 kW UHF power amplifier for use as a transmitter for wind profiler radar. The output matching circuit of the amplifier was tuned to achieve a high drain efficiency and high gain. Large signal pulsed S-parameters were measured for each 1.2 kW module. A thermal imager was used to monitor output matching capacitor temperature. The pulse envelope was measured on the output of the 2.5 kW amplifier. These

amplifiers will be combined together to produce higher power 10-15 kW transmitters in the future. Goals of this chapter are:

- Design and build a low-cost, high efficiency, high power amplifier for wind profiler radar; and
- Combine multiple amplifiers together to produce higher power transmitter in order to enable wind observations at higher altitudes.

Chapter 6 describes some directions for future work and summarizes the contributions of the thesis.

Finally, Appendix A describes the authors first research at the University of Colorado, Boulder on a chip-scale atomic magnetometer (CSAM) project with NIST [91,93-97]. Previous magnetometers such as the Hall Effect device do not have the same sensitivity as an atomic magnetometer. A SQUID magnetometer is more sensitive, but it requires a low temperature cryogenic system, that is not low-cost or portable. Previous atomic magnetometers were table top optical bench systems, but the CSAM has made this into a device with dimensions of a few millimeters. The CSAM can use either an Mx or Bell-Bloom technique for sensing the magnetic field. The goals of this work were to create a small, portable, low-cost, high sensitivity magnetometer and demonstrate its use as a heart magnetic field monitor [92]. Since this first research experience was invaluable for the author, although not directly related to the PhD thesis topic, it is included for completeness.

The following are the specific contributions of this thesis:

- A new 449 MHz wind profiler radar with low sidelobe level modular antenna design. This is the first wind profiler radar using the spaced antenna wind computation method in the 400 MHz frequency bands [47,81-86].
- Sidelobe level reduction techniques for the 915 MHz and 449 MHz wind profiler radars. This is the first systematic study of wind profiler clutter fence and edge treatment antenna improvements using full-wave electromagnetic simulation techniques. Sidelobe reduction by varying height above simulated earth ground (soil) is also studied [69].
- Wind measurements and system comparisons at the Persistent Cold-Air Pool Study (PCAPS) and Dynamics of the Madden-Julian Oscillation (DYNAMO) projects with the 915 MHz wind

profiler, 449 MHz wind profiler, radiosondes, and Doppler lidar [47]. Because of observed sea and land clutter in these measurements, they provided motivation for simulations of 915 and 449 MHz antenna sidelobe reduction technques [69].

- Analysis of optimal spaced antenna receiver spacing using full-wave electromagnetic simulation [69]. For the 3-hexagon system, edge-to-edge spacing is optimal because of the wider beamwidth and therefore lower cross-correlation at zero lag ($c_{12}(0)=0.45$). For the 7-hexagon system, the spacing can be optimized for low sidelobe levels because of the narrower beamwidth and higher cross-correlation at zero lag ($c_{12}(0)=0.6$).

- High power amplifier design using a Freescale 50V LDMOS device for a 54% efficient 1 kW (peak, 10% duty cycle) UHF power amplifier with a 57 cents/Watt transistor cost [47].

- High power amplifier design using an NXP 50V LDMOS device for a 63% efficient 2.5 kW amplifier with a 23 cents/Watt transistor cost. This amplifier won first prize in the 2011 NXP High Performance RF Design Challenge at the International Microwave Symposium in Baltimore, MD and is reported in [67].

Chapter 2

449 MHz Spaced Antenna Radar System Design and Measurements

The spaced antenna wind profiling method [9,15] is a way to determine the horizontal velocity of the wind without steering the antenna beam as in the Doppler Beam Steering (DBS) method [6]. Advantages of this method include a simpler RF network for the antenna feed and improved time resolution of the wind velocities. Existing wind profiler systems at the National Center for Atmospheric Research (NCAR) operate at 915 MHz. Other wind profiling systems such as the National Profiling Network [16], the MU radar [12], the OQNet [17], the Lindenberg radar [18], the Gadanki MST radar [19] and other commercially built systems [20] use 50, 449, and 482, and 915 MHz frequencies. Further review of the current systems, networks, and techniques can be found in [21] and [22]. In addition to considerations of government frequency allocation, higher frequencies, e.g. 915 MHz are more sensitive to Rayleigh scatter from precipitation while lower frequencies, e.g. 50 MHz are more sensitive to clear-air echoes from temperature and humidity fluctuations [23]. At the 50 MHz frequency however, the size of the antenna array becomes very large.

While vertical wind velocities are found from measured Doppler shift, the horizontal winds are computed using the spaced antenna method. Historically the spaced antenna technique has been used with large dipole antennas at HF wavelengths to study the ionosphere [24]. More recently the spaced antenna technique has been developed to measure atmospheric winds with a simpler antenna topology, while adding some processing and receiver complexity. It has been successfully used, e.g. at Jicamarca for wind measurements at 50 MHz using dipole arrays [25], and also at the Adelaide radar [26], and MU radar [27]. This method determines the velocity by computing the cross-correlation between three or more different receiver signals using a method called Full Correlation Analysis (FCA) [15,28]. As the wind and turbulence move over the receivers, the velocity can be computed from the time lag

measured between adjacent receivers. A disadvantage of spaced antenna (SA) is that the signal to noise ratio is typically lower than with Doppler Beam Steering, which uses the first moment (radial velocity) of the radar Doppler spectra (empirical observations suggests SA has a 10 dB lower SNR). FCA uses higher order moments.

The spaced antenna technique offers improved time resolution over Doppler Beam Steering because the beam is pointed in one direction, while DBS systems require averaging over at least 3 different beam directions. In DBS the sampling volumes are widely separated (up to 500 m apart at 1 km range), so to satisfy continuity among the sampling volumes, long time averages (> 10 minutes) are used. The continuous vertical beam used for SA can also allow measurement of boundary layer fluxes of momentum, and potentially sensible and latent heat [9]. Another technique that can be used with a spaced antenna system is baseband digital post beam steering, where the phase of the spaced antenna receiver data is altered in post processing so that the receive beam is steered [103].

(a)

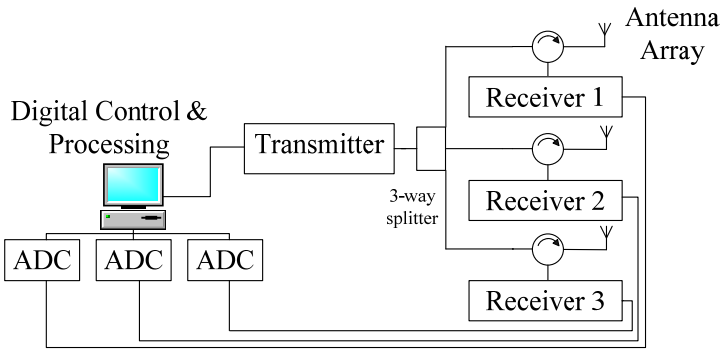

(b)

Figure 2.1. (a) Photograph of the 449 MHz radar wind profiler at Salt Lake City, Utah in November 2010. The receivers are located under the antenna panels. The transmitter and data system are located inside the trailer. (b) Block diagram of the 449 MHz radar wind profiler.

This new radar system is similar to the NCAR Multiple Antenna Profiler Radar (MAPR) which is a deployable 915 MHz spaced antenna radar [9]. Because of high antenna sidelobe levels, the MAPR antenna requires a ground clutter fence, which consists of metal panels placed around the perimeter of the antenna and is difficult to deploy because of its large size (about 3m x 3m square) and mass (about 100kg). The 449-MHz radar presented here uses an antenna design with lower sidelobe levels that eliminate the need for a clutter fence. While 50-MHz systems are most sensitive to clear-air echoes from temperature and humidity fluctuations, the size of the antenna arrays at this frequency is quite large and not as suitable for portable systems. The 449-MHz wind profiler frequency is a good compromise between antenna size and clear air wind sensitivity and there is an available government frequency allocation. This frequency is chosen for the system described in this work and shown in Figure 2.1(a).

The requirements for wind profilers are different than those for other radars, e.g. precipitation radars [29], because wind profilers receive very little of the transmitted signal. The radar is designed to measure boundary layer winds from an altitude of 100m to 5km. The desired target is Bragg scatter from turbulence [30], which occurs from irregularities in the index of refraction produced by temperature and humidity fluctuations.

Table 2.1: Radar Parameters

Parameter	**Value**
Radar Frequency	449 MHz
Transmit Power	3 1 kW modules
Inter-pulse Period	50 μs
Pulse coding	4-bit complementary
Maximum Range	5 km
Minimum Range	200 m
Range Resolution	150m
Transmit Array Gain	24.8 dBi
Receiver Array Gain	19 dBi
Receiver Noise Figure	2 dB

A general block diagram of the 449 MHz wind profiler is shown in Figure 2.1(b), while the basic radar parameters are given in Table 2.1. A pulse is generated by a D/A converter within the computer system. The system uses a pulse with a 4-bit complementary code [31] and an inter-pulse period of 50μs. This pulse is amplified by the transmitter and transmitted on all three antennas. Each of the three antennas, receives the radar return signal separately. The signal from each of the three receivers, described in detail in the next section, is processed separately to compute horizontal winds. The LDMOS power amplifier (PA) design and characterization is presented and then system measurements and wind measurements are detailed.

2.1 Receiver Design and Implementation

The receive section is shown in Figure 2.2. The receive section consists of a limiter to protect the LNA, a 5 MHz filter, and a mixer / IF amplifier stage to downconvert the 449 MHz to 60 MHz. The 5 MHz filter blocks out Radio Frequency Interference (RFI) and also keeps out-of-band noise from aliasing into band during the mixing process. The IF amplifier drives the 30m cable back to the data system and A/D converter. The gain of the receive section is designed so that the receiver noise will be amplified enough that the 2 least significant bits of the A/D converter will always be active.

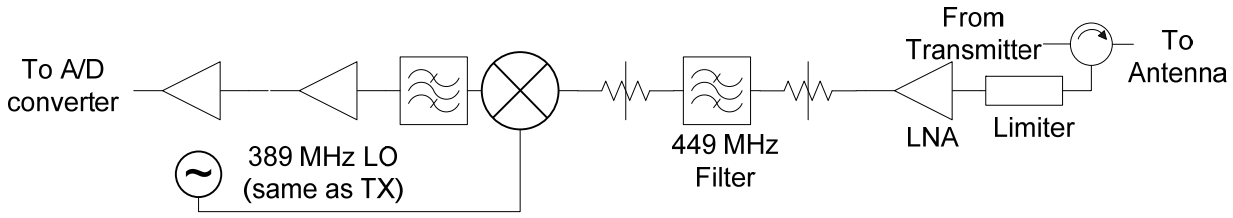

Figure 2.2. Block diagram illustrating one of the three receiver channels.

A receiver noise temperature of 250K is measured for the LNA, which includes sky noise, LNA noise figure, and cable losses. To calculate required system gain, first the receiver noise power is calculated using the front end filter bandwidth of 5 MHz and the receiver noise temperature of 250K, as follows:.

$$P_{Noise} = 10\log\frac{kTB}{.001} = \text{-}107.6 \text{ dBm}$$

Because winds and atmosphere have radar returns in the -140 to -150 dBm range we need additional processing to receive signals below the -107 dBm level. The SNR after coherent integration of the radar signal is given by:

$$SNR = N \cdot SNR_{Single\ Pulse}$$

where N≅128 is the number of coherent integrations. For this value, the coherent averaging gain is about 21 dB. The minimum detectible signal-to-noise ratio due to spectral averaging was determined empirically in [8,32] to be well described by:

$$SNR_{S.Avg.} = 10\log\frac{25\cdot\sqrt{N_{SP} - 2.3125 + \frac{170}{N_{FFT}}}}{(N_{FFT})(N_{SP})}\ [\text{dB}]$$

where N_{FFT} = 256 is the number of points in the FFT and N_{SP} = 17 is the number of spectral averages. For these values, the spectral averaging gain is about 16.5 dB. This gives a total processing gain of 37.5 dB, resulting in a minimal detectable signal of -(107 + 37.5) = -144.5 dBm.

Full scale input for the Pentek 7642 A/D converter is +10 dBm. The SNR in the LTC2255 datasheet is given as 71 dBFS at 60 MHz [33]. Thus, the required input power to be above the A/D noise is +10 dBm - 71 dB = -61 dBm. This results in a required IF gain of at least 107.6 dBm - 61 dBm = 46.6 dB.

During the prototype phase, a number of sensitivity tests were conducted. Each test involves checking each receiver for sensitivity to a -150 dBm test signal. This test is important because it verifies the performance of the system from the antenna terminal through the receiver to the signal processing software. All of the receivers had a detection threshold near -150 dBm. The receive signals are processed with spaced antenna software based on the NCAR Maprdisplay package [34], and further processed for horizontal winds using Briggs' Full Correlation Analysis (FCA) method [28].

2.2 Spaced antenna horizontal wind computation

The spaced antenna technique of radar wind profiling relies on a radar return from the Bragg scatter target described in Chapter 1. While the Doppler shift of the received signal is used to compute the vertical velocity,

spaced receivers are used to compute horizontal winds. The backscatter from the turbulence target produces a unique diffraction pattern at the surface illustrated in Figure 2.3 [35]. This pattern travels with a velocity *V*, that is related to the true velocity of the atmospheric wind at the altitude of interest.

G.I. Taylor formulated a hypothesis in 1938 that is now called the Taylor Frozen-in Turbulence Hypothesis [36-37]. This hypothesis basically states that turbulence moving past an observer can be thought of as frozen non-changing turbulence. Therefore as the diffraction pattern moves in Figure 2.3(a), its characteristics change very little.

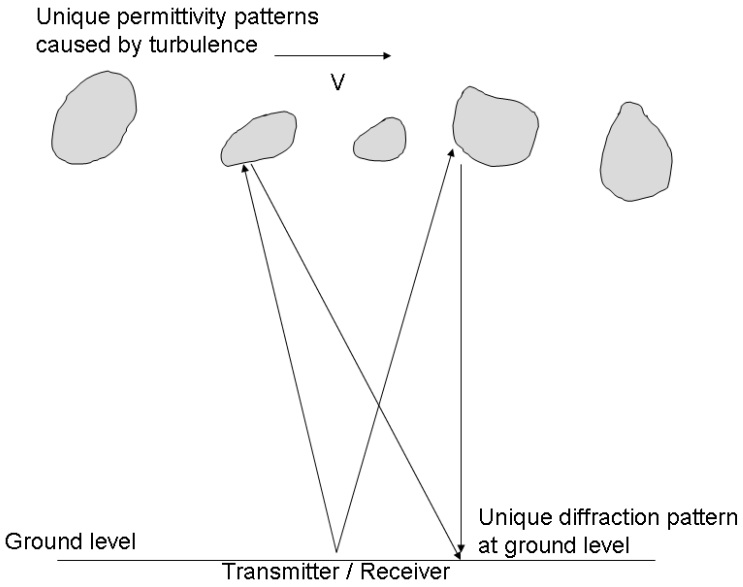

(a)

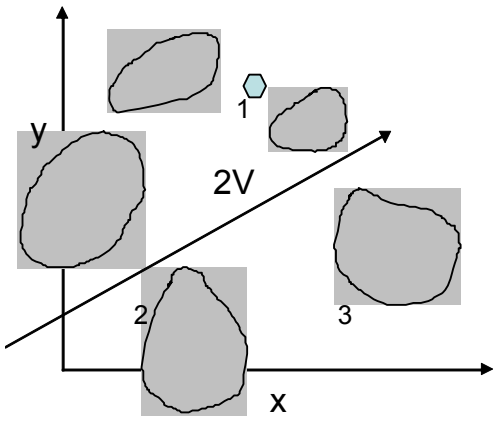

(b)

Figure 2.3.(a) Illustration of how backscatter received at ground level is a superposition of scatter from multiple targets above. (b) Top view of three spaced receivers measuring the travelling diffraction pattern at ground level.

If three or more spaced receivers measure the travelling diffraction pattern at ground level, as in Figure 2.3(b), the horizontal motion can be computed by measuring the time lag using a simple cross-correlation between receiver signals and then trigonometry to compute the wind vector. This computation has the following shortcomings:

1. The pattern observed on the ground may be systematically elongated in a direction not perpendicular to the velocity. This will result in a velocity computation that is not the true velocity of the wind.

2. The pattern evolves over time. This also can cause velocity errors.

To address these shortcomings, the Full Correlation Analysis method described by Briggs [28] is used. This method uses auto and cross-correlations instead of time delays between channels to compute the true velocity. This method is described in more detail in Appendix B. Next, a transmitter architecture will be presented that will enable the use of multiple high power amplifier stages to increase the SNR.

2.3 Transmitter Architecture

The transmit section of the system is shown in Figure 2.4. It consists of a mixer to convert the 60 MHz transmit pulse from the D/A converter to 449 MHz. A 10W driver and 80W amplifier stage drive the final amplifier. The core of the transmit section is the three 1 kW peak power amplifiers. These three amplifiers are combined using a reactive combiner, the output is transmitted through a 30m heliax cable to a 3-way splitter located underneath the outdoor antenna. The output is split to the three hexagonal antennas and then split 18 ways using phase matched cables to each circular patch antenna.

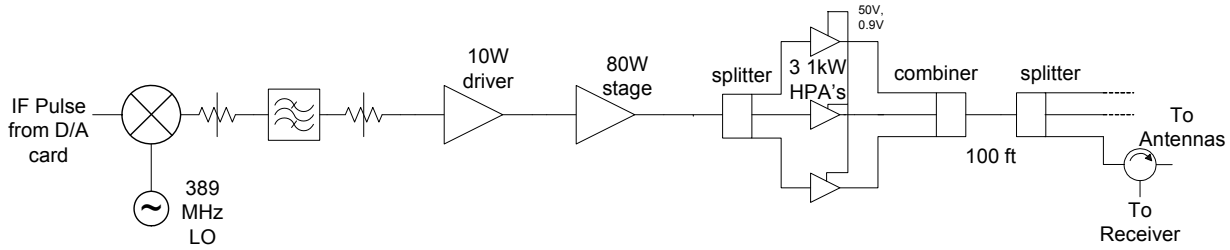

Figure 2.4. Diagram illustrating the transmit section of the radar. The 1 kW High Power Amplifiers are driven by 80W and 10W stages.

The MRF5S9070N is a low cost (~$35) LDMOS transistor capable of 80W CW. To design a high efficiency amplifier using this transistor, Class-E amplifier theory was used [40-41]. The transistor is modeled as a switch with an output capacitance. For class-E operation, a network is added to the output of the transistor that forms a low pass filter so that only a sinusoidal waveform is seen across the output load. Using the Class-E theory derived in [42], the ideal output impedance to achieve a sinusoidal waveform is given by:

$$Z = \frac{0.0446}{C_S f} e^{j49.05^\circ} [\Omega]$$

C_s can be estimated from the given S-parameters for a transistor. In this case the manufacturer provided a value for C_s in the datasheet, 34 pF. Using this capacitance value, the calculated value of the output impedance is Z = 2.8 + 3.3j Ω. Because of the high output capacitance of this device, a low output circuit impedance is required.

The substrate used for the 80W amplifier is Rogers 4350B. The output network was designed for the target impedance and then a shunt capacitor was used on the output to tune the amplifier for best power added efficiency (PAE) and output power, Figure 2.6. A PAE of 68% was measured with a CW output power of about 49 dBm, Figure 2.7. Additional tests were conducted to confirm the phase stability of multiple amplifiers over temperature. The measured phase variation was a maximum of 8 degrees of phase over the -15C to 40C temperature range. Because of the low cost, this transistor was initially considered for use in an active array design with an amplifier located behind each antenna. As higher power final stages were considered, this amplifier became a low cost driver amplifier.

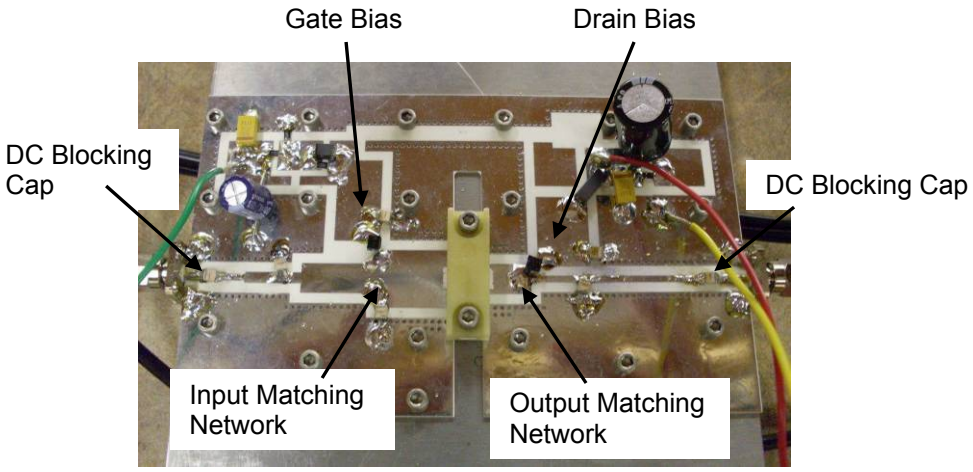

Figure 2.6. Photograph of 80W amplifier based on a Freescale MRF5S9070N transistor. The transistor is mounted underneath a clamp in the center of the circuit.

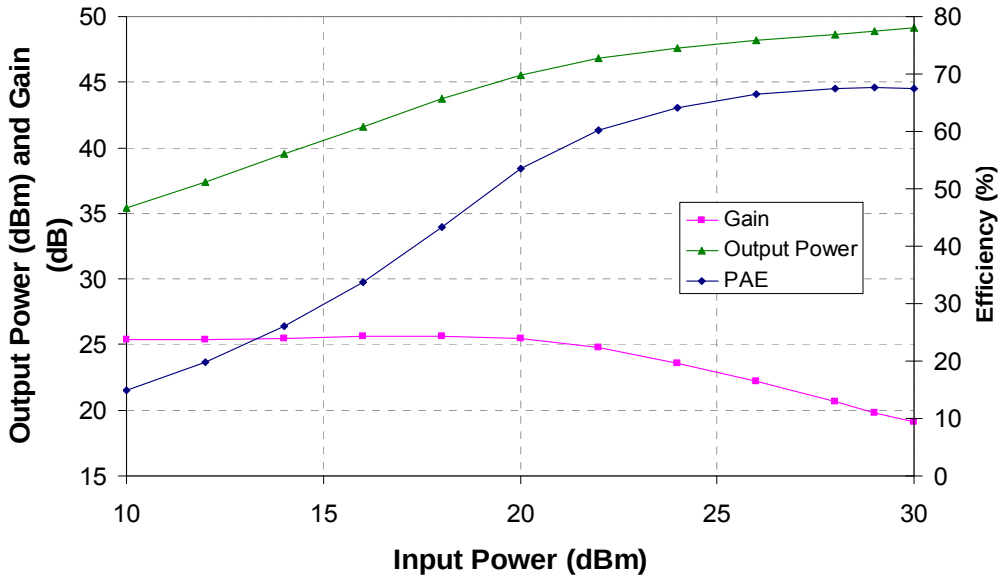

Figure 2.7. Measured 80W LDMOS Pout, gain, and PAE vs. input power. The operating point is Pin = 30 dBm, Pout = 49.1 dBm CW, PAE = 68%, gain = 19 dB.

Improvements in LDMOS device technology have enabled kW-level amplifiers. The Freescale MRF6VP41KHR6 [43] was evaluated for use as a 1 kW peak power pulsed 449 MHz high power amplifier. It is packaged in a push-pull configuration, so that two devices are easily combined. A manufacturer test circuit was modified for best gain, efficiency, and output power at 449 MHz. The goal for this application is to have a 1 kW, 10% duty cycle, 449 MHz pulse amplifier.

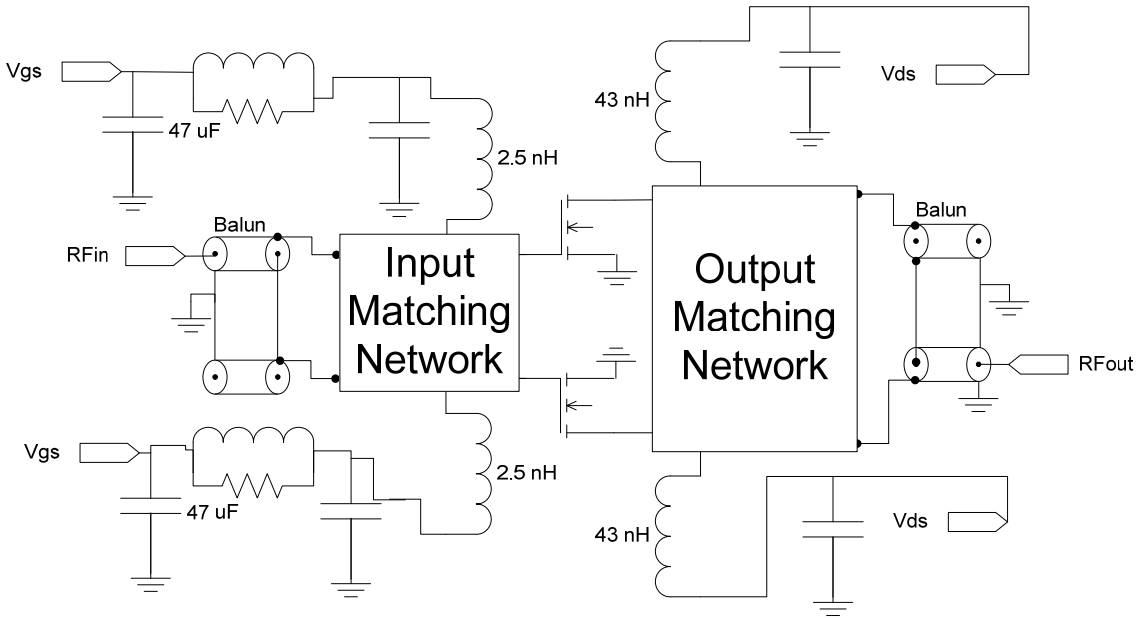

(a)

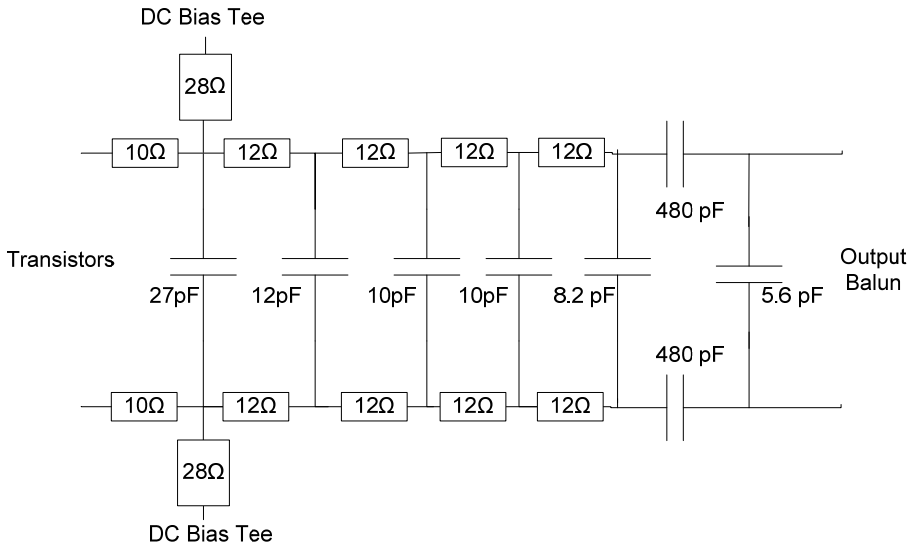

(b)

Figure 2.8.(a) Schematic of the 1 kW (peak) LDMOS pulse amplifier. Coaxial baluns drive the push-pull transistor pair and combine the output. (b) Output matching network of the 1 kW LDMOS amplifier using low impedance microstrip transmission lines.

The 1-kW peak pulse amplifier uses lumped element components. The overall schematic including bias tees is shown in Figure 2.8(a). The amplifier layout was fabricated on Rogers 4350 substrate. Some of the benefits of a

push-pull amplifier are a doubling of the input and output impedances and reduced even harmonics. Coaxial baluns made of 25Ω coax are used to transform the unbalanced 50Ω input and output impedances into lower impedances that are easier to match to the transistor. The input return loss of the balun at 449 MHz is -12 dB (VSWR 1.7:1). The insertion loss of both balun networks measured back-to-back is 0.1 dB. The amplifier is tuned for best gain, PAE, and output power at 449 MHz by changing the value and position of the capacitors in the input and output matching networks, however the efficiency at 1 kW output is limited by the 110V maximum rating for Vds. The output matching network is shown in Figure 2.8(b). The input matching network has a similar topology.

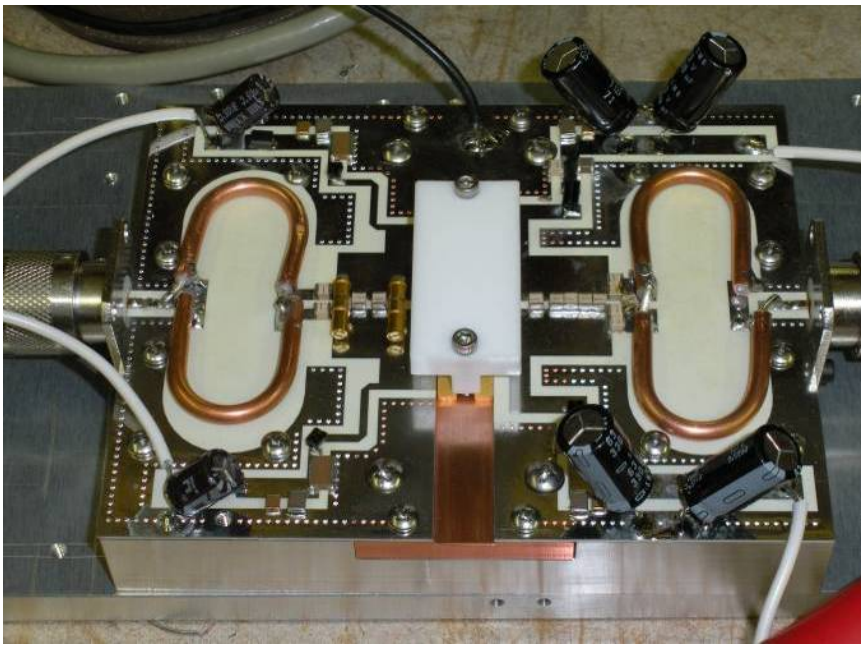

Figure 2.9. Photograph of the 1-kW (peak) pulse amplifier module based on the Freescale MRF6VP41KHR6 LDMOS transistor in push-pull configuration.

A photograph of the amplifier with a light-weight aluminum heat sink is shown in Figure 2.9. A copper insert was installed below the transistor to allow more heat transfer between the transistor and the aluminum heatsink. A transistor clamp made of Teflon allows for easy test and replacement of the transistor if needed.

Output power, efficiency, and gain of the amplifier as a function of input power are shown in Figure 2.10. The best amplifier operating point is Pin (peak) = 41.5 dBm, Pout (peak) = 60.1 dBm, PAE = 53.8%, gain = 18.5 dB. Since the final PA stage has 18.5 dB gain, the overall efficiency of the amplifier chain is dominated by that stage. The PAE at 1 kW output is limited by the 110V maximum rating for Vds. Figure 2.11 shows the amplifier

performance vs. frequency. The amplifier performance is frequency dependent because of the narrowband nature of the input and output matching networks. Because the only modulation of the radar pulse are phase shifts, the bandwidth needed for the amplifier is less than 5 MHz.

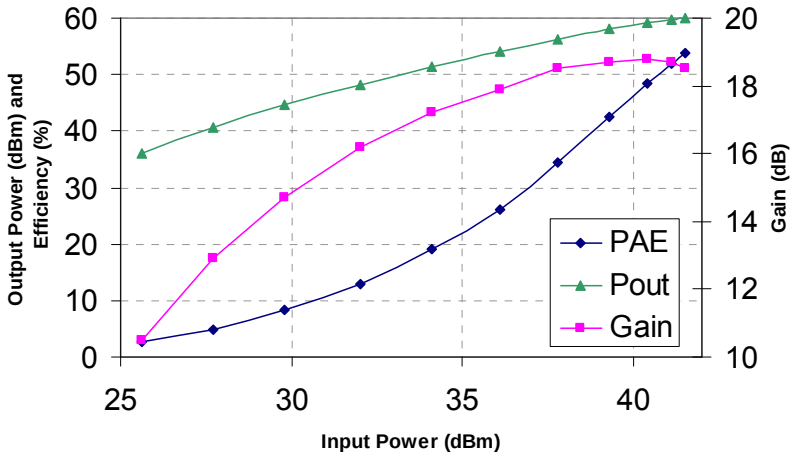

Figure 2.10. 1 kW LDMOS Amplifier performance vs Input Power. Pulsed operation, 10% duty cycle. Best amplifier operating point is Pin (peak) = 41.5 dBm, Pout (peak) = 60.1 dBm, PAE = 53.8%, gain = 18.5 dB.

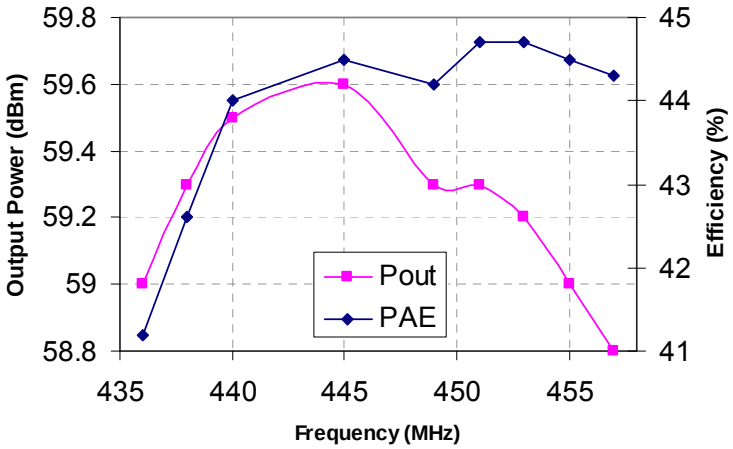

Figure 2.11. Measured 1 kW LDMOS Amplifier performance vs. frequency. Pulsed operation, 10% duty cycle. Amplifier has output power above 59 dBm and efficiency above 44% from 440 to 455 MHz. Input power was reduced to 40.38 dBm for this sweep.

Another amplifier requirement is to produce low noise between pulses. To accomplish this simply, the transistor is biased below cutoff with Vgs=0.9V. This bias voltage turns the transistor off between pulses and allows for sufficient gain during the pulses.

2.4 System Measurements

Final tests involved the whole system including both the transmitter and receiver. The radar was tested for compliance with ITU requirements [44] and the United States Radar Spectrum Engineering Criteria (RSEC) requirements [45]. Pulse shaping is used to limit the bandwidth of the transmit pulse to the requirement of a -20 dB bandwidth of 2 MHz. Measurements without pulse shaping were taken to determine whether pulse shaping was needed. The measurements were made to check against the requirements shown in Table 2.2 with a 1 microsecond pulse and both the commercial transmitter and the amplifier described in this thesis. Two 449 MHz Lark Engineering Inc. filters were added in the transmit chain, one right after the mixer (with attenuators) and the other right before the final amp (with attenuators).

Table 2.2: Spectral Emissions Requirements and Measurements

Requirement	Measurement
-20 dB, 2 MHz bandwidth	5 MHz
-40 dB, 24 MHz bandwidth	31 MHz
-60 dB, second harmonic	-50 dB

The spectrum analyzer was in "line spectrum" mode, so that RBW < 0.3 * PRF. The PRF was 20 kHz (50 microsecond IPP). The first measurement was taken by disconnecting the feed cable for one patch, and then running into about 30 dB of attenuation before going into the spectrum analyzer.

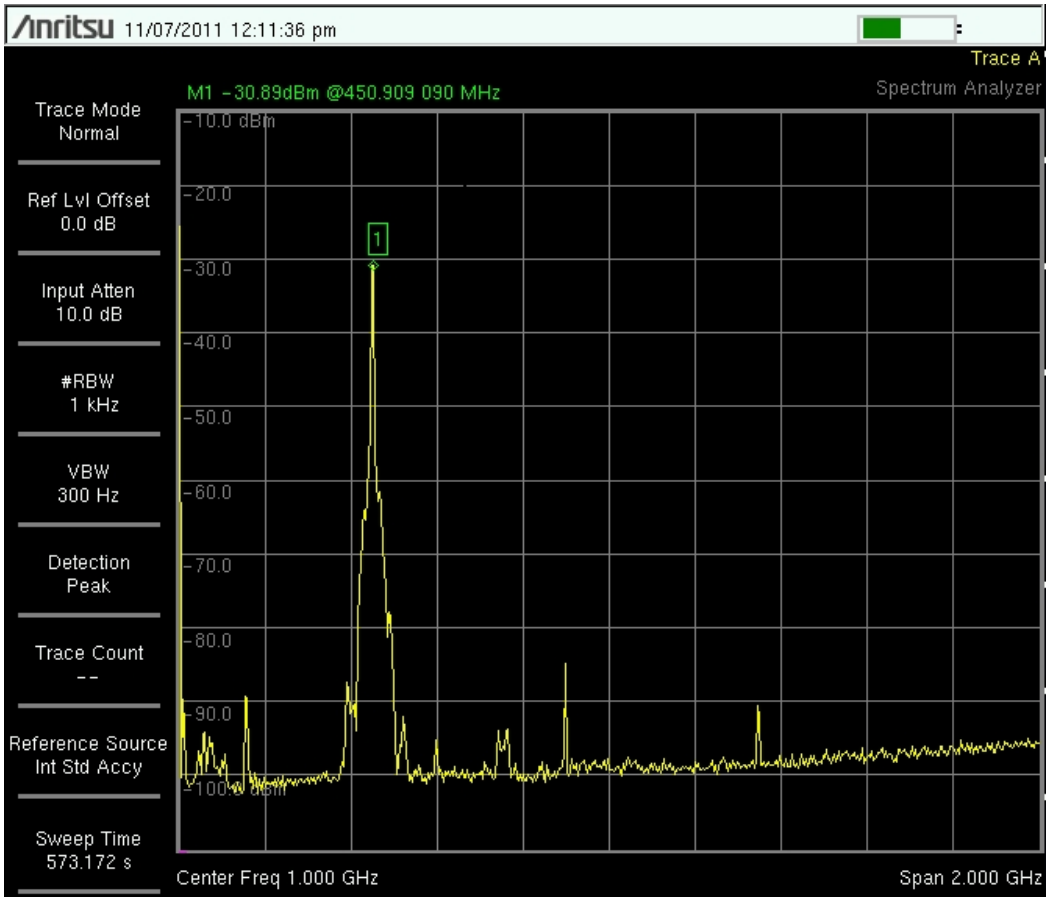

Figure 2.12. Measured radar output emissions vs. frequency. Commercial 2 kW transmitter is used for this measurement.

Figure 2.12 shows the measured data. The RSEC requirement is harmonics 60 dB down. There are three peaks to observe: between 152 and 156 MHz there is an unidentified signal, second harmonic is above the 60 dB limit, third harmonic is right at the limit. The transmitted spectrum also shows the third harmonic, but more than 60 dB below. Second harmonic is only 45 dB below. The addition of a second 449 MHz filter lowered the 152-156 MHz peak to more than 60 dB below. The next test is to observe the bandwidth close to the 449 MHz signal. Using a 1 μs pulse (no coding) and a 0.1 μs rise time, it was calculated that the allowed -40 dB transmit bandwidth is 24 MHz. The current system configuration did not satisfy the -40 dB requirement.

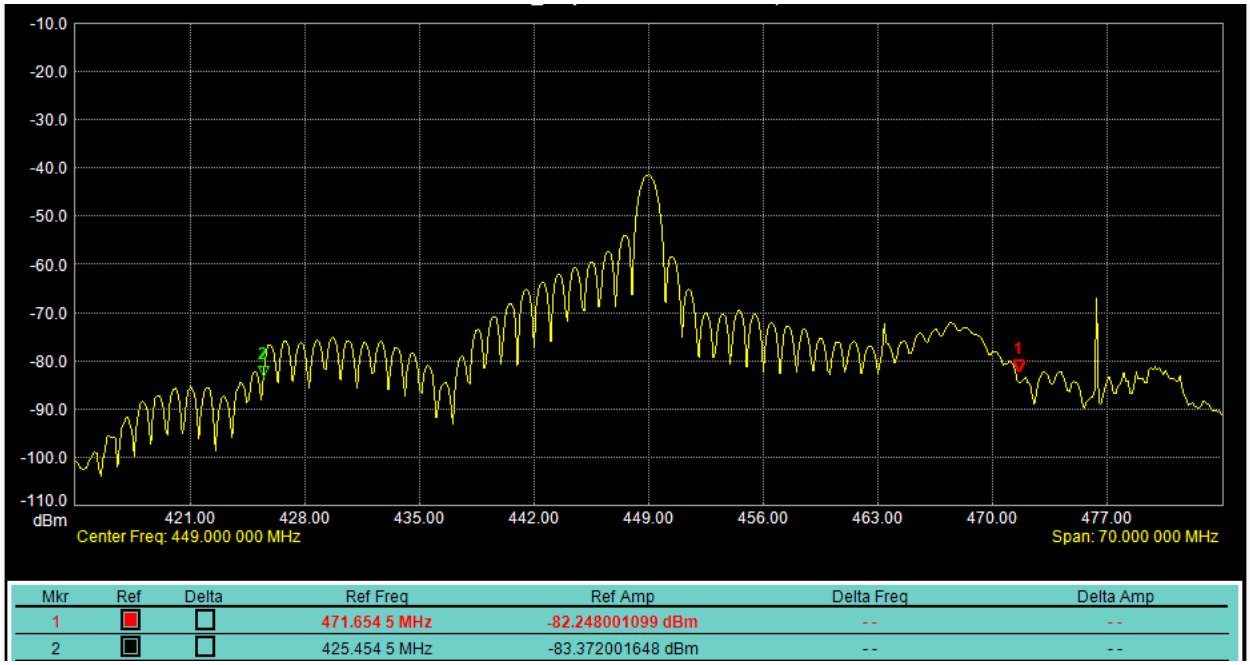

Figure 2.13. Measured radar output emissions vs. frequency. Commercial 2 kW transmitter is used for this measurement. Markers are placed at -40 dB points.

Figure 2.13 is a plot of the transmitted spectrum with markers near the -40 dB points. This is with the spectrum analyzer connected to a wideband discone antenna (25 MHz to 6 GHz). It is clear it is an antenna measurement because an out of band peak around 477 MHz is seen from another source. The markers are near the -40 dB points: about 46 MHz between the points. Adding another 449 MHz filter with attenuators around it right before the final amp brings the -40 dB bandwidth down to 31 MHz.

The -20 dB bandwidth is given by RSEC to be 2 MHz. The markers in the measurement for Figure 2.14 show the -20 dB bandwidth is about 5 MHz, more than the 2 MHz by RSEC. This is also measured on the discone antenna.

It is clear from these measurements that to achieve RSEC-E compliance, pulse shaping will be required. Pulse shaping is currently being implemented while the system is operated in accordance with RSEC-A for transportable systems (exemption from the above requirements). Along with pulse shaping, there are a number of frequency-dependent components that aid in filtering the 449 MHz pulse bandwidth to the -20 and -40 dB levels and its harmonics down to the -60 dB levels (e.g. the circulators and splitters). These measurements were repeated with the 1 kW LDMOS amplifier module and it was found the the 1 kW module had similar or lower output emissions. Therefore the dominant factor in radar output emissions for this system is pulse shape. All other requirements such as side-lobe suppression, frequency tolerance, and peak EIRP are also satisfied.

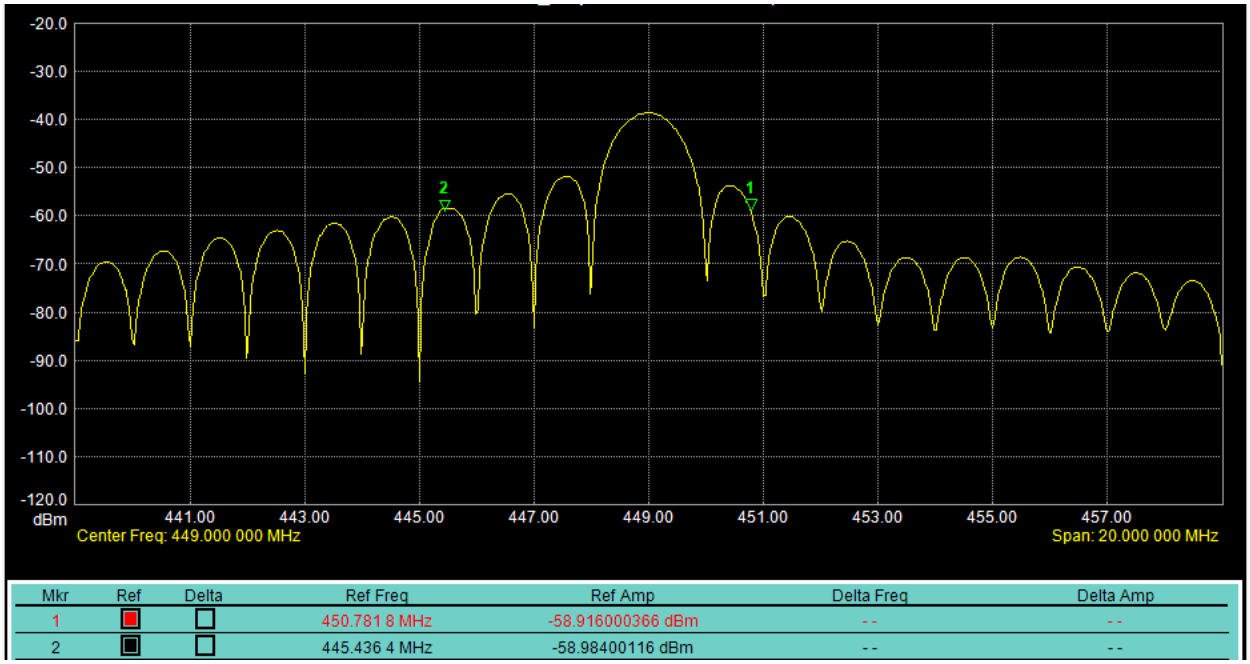

Figure 2.14. Measured radar output emissions vs. frequency. Commercial 2 kW transmitter is used for this measurement. Markers are placed at -20 dB points.

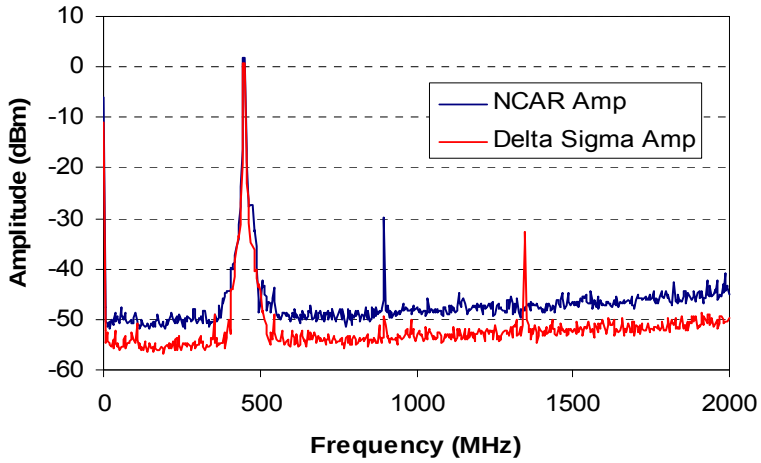

Figure 2.15. Measured radar output emissions vs. frequency using a coupler at the output. Spectral output of 3 combined 1 kW modules (NCAR Amp) is compared with a commercial 2 kW transmitter (Delta Sigma Amp).

Comparisons were made of three of the 1 kW modules combined together vs. a commercial 2 kW amplifier from Delta-Sigma, Inc. Figure 2.15 shows the result of this comparison. This spectrum was measured using a broadband coupler at the output of the amplifiers. Note that the amplitude is that measured at the spectrum analyzer and does not indicate the peak transmit power. The noise level is different between the two measurements because the resolution bandwidth was changed. The NCAR amplifier (three 1 kW modules combined) produces more second harmonic at 898 MHz than the Delta-Sigma amplifier, but the Delta-Sigma amplifier produces more third harmonic at 1347 MHz. These harmonics will be filtered out by the narrow band splitters, circulators, and antennas. Figure 2.16 shows that the second harmonic generated by the NCAR amp is greatly attenuated by the circulators, splitters, and antennas (third harmonic was not measured for this case because it was not observed at the coupler). For the Delta-Sigma amp, there is no observed second or third harmonic received by the patch antenna.

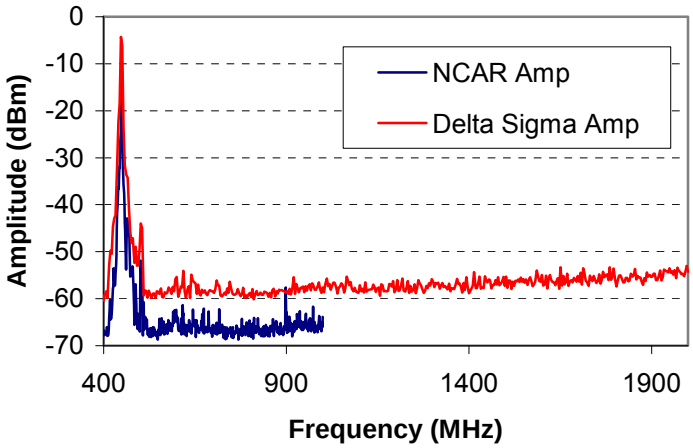

Figure 2.16. Measured radar output emissions vs. frequency using a patch antenna connected to a spectrum analyzer. Spectral output of 3 combined 1 kW modules is compared with a commercial 2 kW transmitter.

Noise figure of the receiver was measured using an HP 8970B noise figure meter with an HP 346B noise source. The measurements are shown in Table 2.3. The factory specification for the Miteq LNA noise figure is 0.8 dB. Measuring the noise figure for the cascade of the circulator, limiter, LNA and 449 MHz filter gives a combined noise figure of 1.38 to 1.57 dB. This corresponds to a noise temperature of 110-120K, which is better than the 250K noise temperature that is measured for other 449 MHz systems [46], but does not include the additional cable losses for the 1 meter cables to connect to the antenna.

Table 2.3: Receiver Noise Figure Measurements

Channel	Noise Figure of LNA	Noise Figure of Antenna Input to Mixer Input
0	0.91 dB	1.38 dB
1	0.97 dB	1.57 dB
2	1.12 dB	1.57 dB

Another significant test is a blanker delay test. In a pulsed radar, the blanker switches off the receive signal to the A/D converter during the transmit pulse. Connecting the A/D converter to the receiver during the radar pulse will saturate the A/D converter. This saturation takes a longer time to recover from than the time it takes to switch the blanker. For this test, the system is run normally as a radar during a period with good atmospheric SNR in the range below 1 km and little or no RFI. Every 2 minutes, the blanker turn-off time is adjusted using the profiler control software and a 0 dB SNR level is collected for each blanker turn-off time. Figure 2.17 shows the data from this test. Note that 0 dB SNR was a level chosen for this test. The system is able to compute winds below 0 dB SNR using additional averaging. The goal of this test is to find the optimum blanker turn-off time. As shown in Figure 2.17, the SNR at the lower range gates can be significantly improved with the optimum blanker turn-off time.

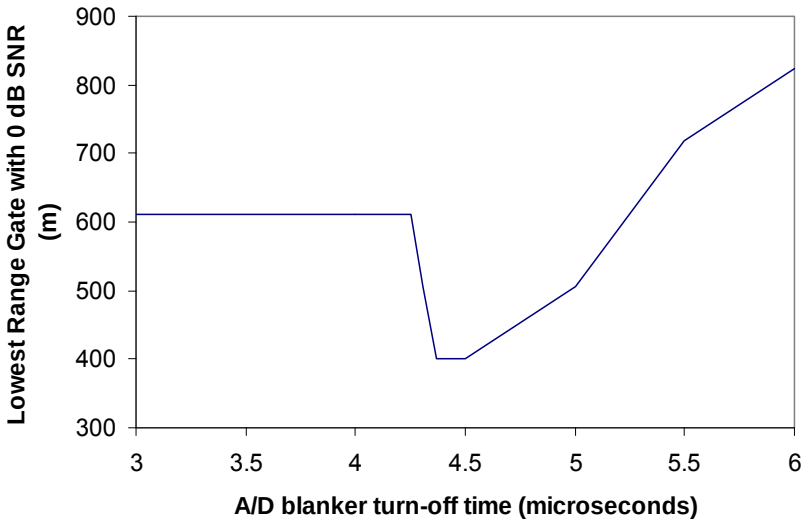

Figure 2.17. Measurement of the lowest range gate SNR while varying the A/D converter blanker turn-off time. The SNR of the lowest range gates is affected by the time that the blanker deactivates.

2.4.1. Wind Data from Boulder, Colorado

As a confirmation of the performance of the new radar, the new wind profiler radar was first operated during prototype tests at the NCAR Foothills Laboratory in Boulder, CO. Figure 2.18 shows data from October 23rd, 2010. Precipitation can be seen in the data at 9UT and between 15 and 18UT as indicated by the downward vertical velocities.

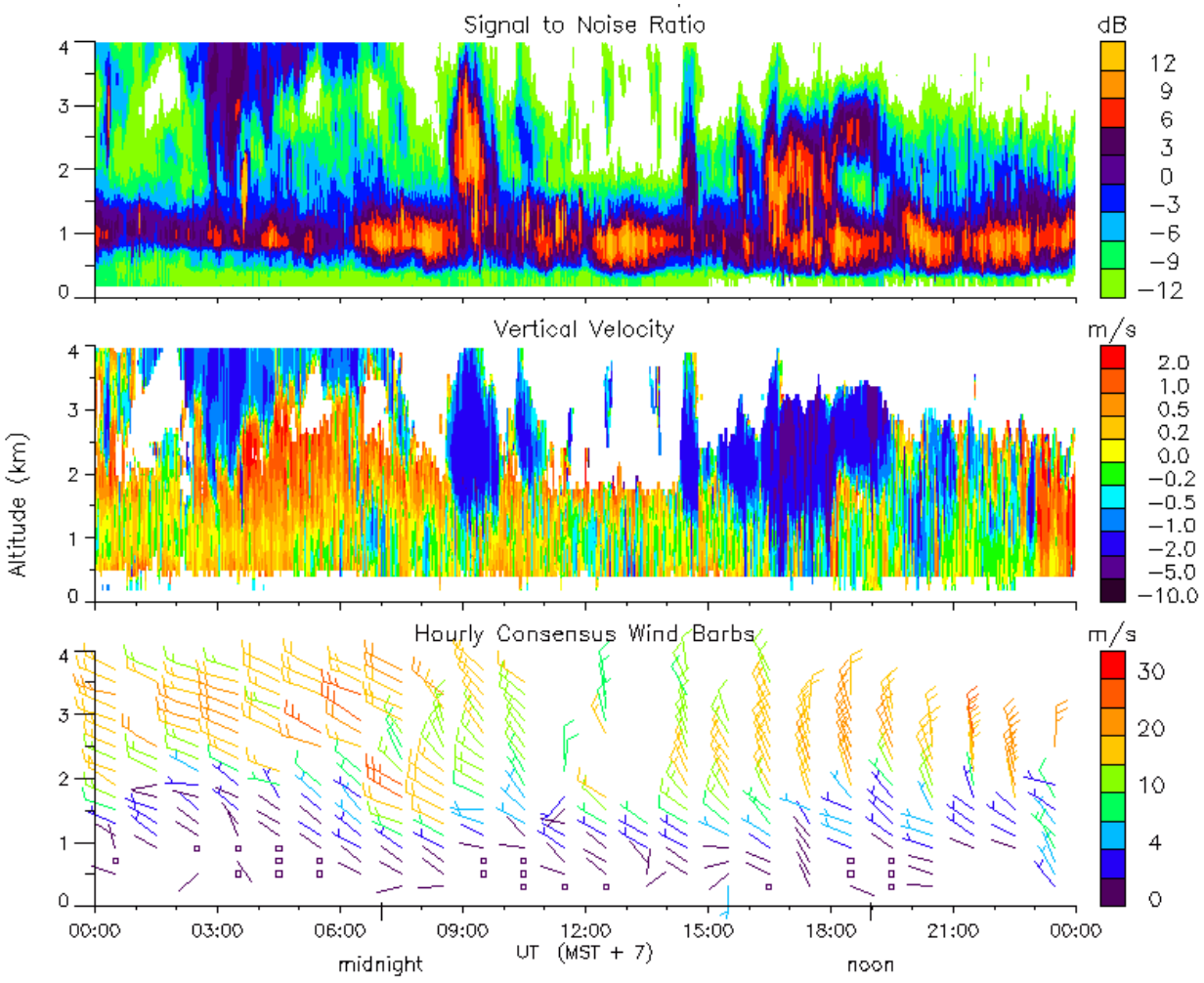

Figure 2.18. Boulder, Colorado wind profiler data on 23 October 2010 from 449 MHz system using 3 combined 1kW amplifiers. The plots show altitude vs. time with the color code indicating SNR for the top plot and velocity in m/s for the bottom two plots. Precipitation is indicated by strong SNR and negative (downward) vertical velocities.

The top plot in Figure 2.18 shows Signal to Noise ratio. Note that SNR is decreased below 1 km because of ground clutter and antenna ringing. SNR is higher during the precipitation events at 9UT and 15-18UT. The middle plot shows the vertical velocity. The vertical velocity is computed directly from the Doppler shift of the return

signal. The bottom plot shows horizontal wind barb data. These horizontal winds are computed by cross-correlations between the receiver signals using the spaced antenna method. The wind direction is indicated by position of the barb (e.g. a barb pointed downwards with the tail straight up is a wind from the North). The wind velocity is indicated by the number of lines at the tail of the barb and also by the color code.

2.4.2. Wind Data from West Jordan, Utah

After initial prototype tests in Boulder, the radar was transported and deployed as part of the Persistent Cold Air Pool Study (PCAPS) in West Jordan, Utah, south of Salt Lake City. A commercially available 915 MHz wind profiler was also located at this site to allow comparison of the data between the two profilers. A nearby site contained a SODAR and radiosonde launch site for additional comparisons. Data for all systems at PCAPS was collected from 15 November 2010 until 15 February 2011.

A cold-air pool is a weather phenomenon that can trap air pollution near the ground level. A picture of the pollution effects of a cold-air pool in Salt Lake City is shown in Figure 2.19. Two of the goals of PCAPS are to study what causes formation of the persistent cold-air pool and what causes dissipation of the pool. A cold-air pool is a temperature inversion in which a cold layer of air is trapped near the ground under a warm layer of layer of air. This will be shown in the data from this project.

Figure 2.19. Picture of a persistent cold-air pool event at Salt Lake City, Utah showing pollution trapped near the ground level.

Figures 2.20-2.22 show a comparison of data from both Wind Profilers. The SNR and wind data are quite similar. One issue that can be seen in the raw signal data is the presence of RFI. Because wind profiler radars typically have low SNR, RFI is a common problem [19]. RFI is seen in the data as a constant signal return from all range gates. Because of the position of the antennas, each antenna sees a different level of RFI. As an example, RFI is seen in Figure 2.20, Signal Channel 2 from 12-21UT. The FCA processing algorithm is normally able to detect winds in the presence of RFI. Because snow is the only expected precipitation during this project, a modified Butterworth filter rejects all vertical Doppler velocities greater than 5 m/s. This filter can be modified for other precipitation. RFI can still affect the SNR as seen at 06UT. The RFI sources are usually communication and pager sources at frequencies such as 450 and 451 MHz.

A precipitation event on 9 January 2011 is seen in the data in Figures 2.20 and 2.21 between 05 and 10UT. The precipitation is indicated by the high SNR signals. A comparison of the 449 MHz and 915 MHz profiler data shows that the 449 MHz radar is able to sense winds at a higher altitude than the 915 MHz profiler. Higher height coverage can be attributed to the higher transmit power (500W peak for the 915 MHz system vs. 3000W peak for the 449 MHz system). Increased sensitivity can also be explained by the wavelength dependence of the effective aperture, which is directly related to SNR. The effective aperture of the 449 MHz system was calculated using an antenna gain simulation to be 10.5 m^2, and for the 915 MHz system it is 3.4 m^2. The difference in aperture provides about 5 dB of difference in SNR. These calculations assume no losses from the antenna feed networks and 100% antenna efficiency. The clear air backscatter cross section is only weakly dependent on wavelength ($\lambda^{-1/3}$), so this provides about 1 dB of SNR difference between 449 and 915 MHz. total SNR improvement is 13 dB. Given that the spaced antenna method has about a 10 dB decrease in SNR, then there is a 3 dB net improvement, this is consistent with the data. The data also shows that the 449 MHz system is able to sense winds down to the 500m level, while the 915 MHz system can sense down to the 200-300m level. The reason for this difference is that short transmit pulses were not yet implemented in the profiler control software, this is planned in future work.

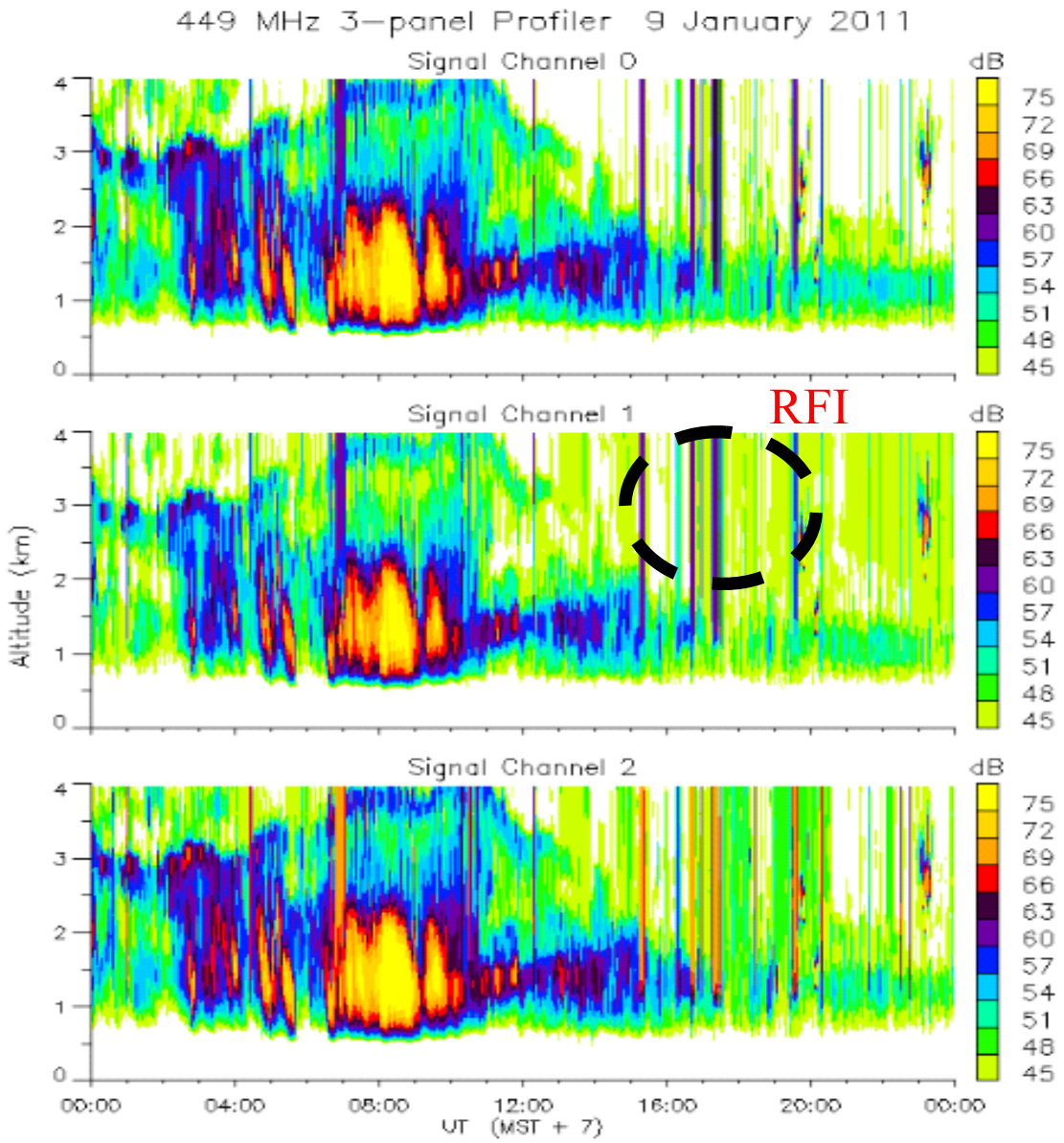

Figure 2.20. 449 MHz spaced antenna wind profiler data at West Jordan, Utah on 9 January 2011. Three channel raw signal level vs. altitude and time in dB.

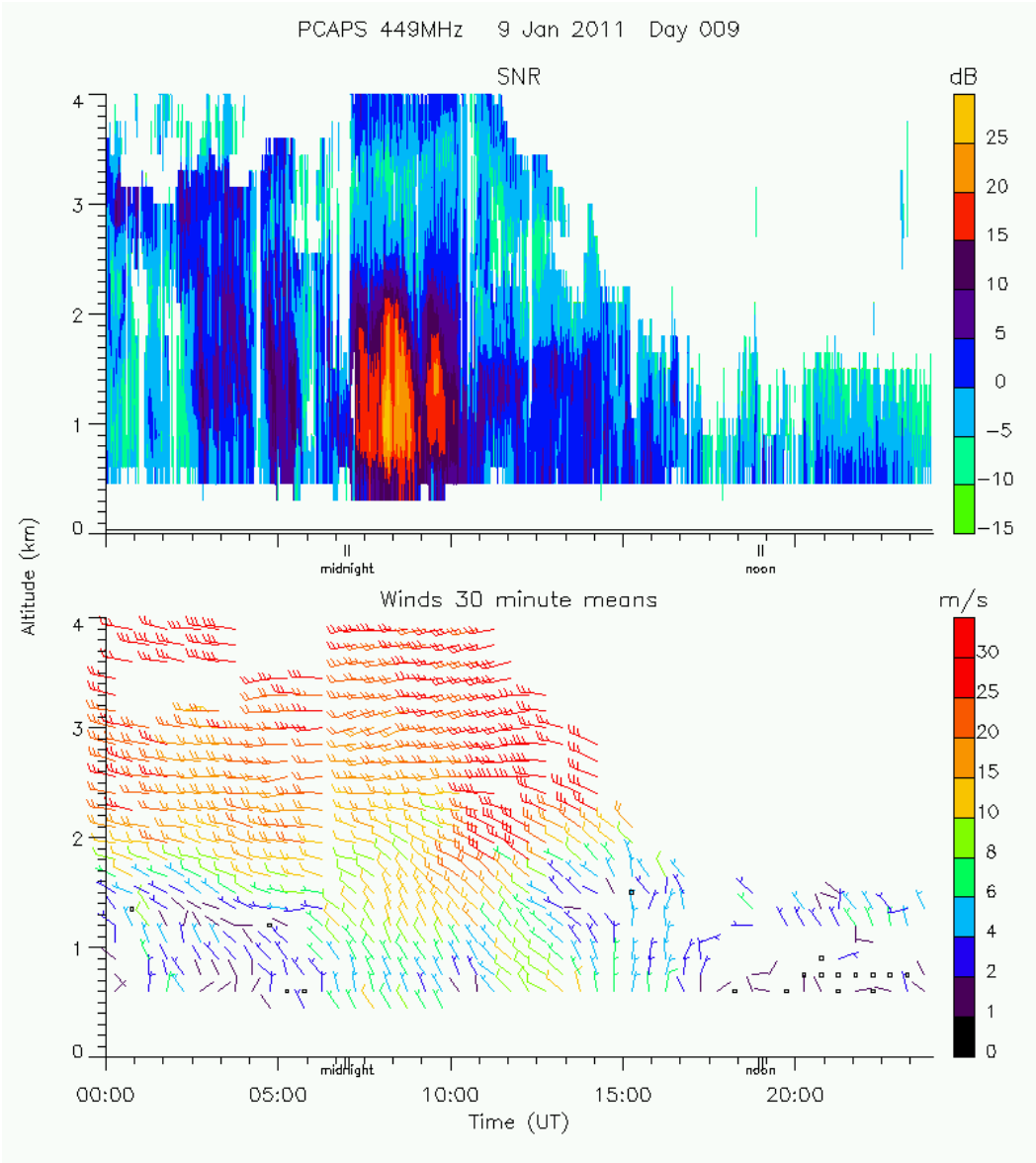

Figure 2.21. 449 MHz spaced antenna wind profiler data at West Jordan, Utah on 9 January 2011. SNR (dB) and horizontal winds (m/s).

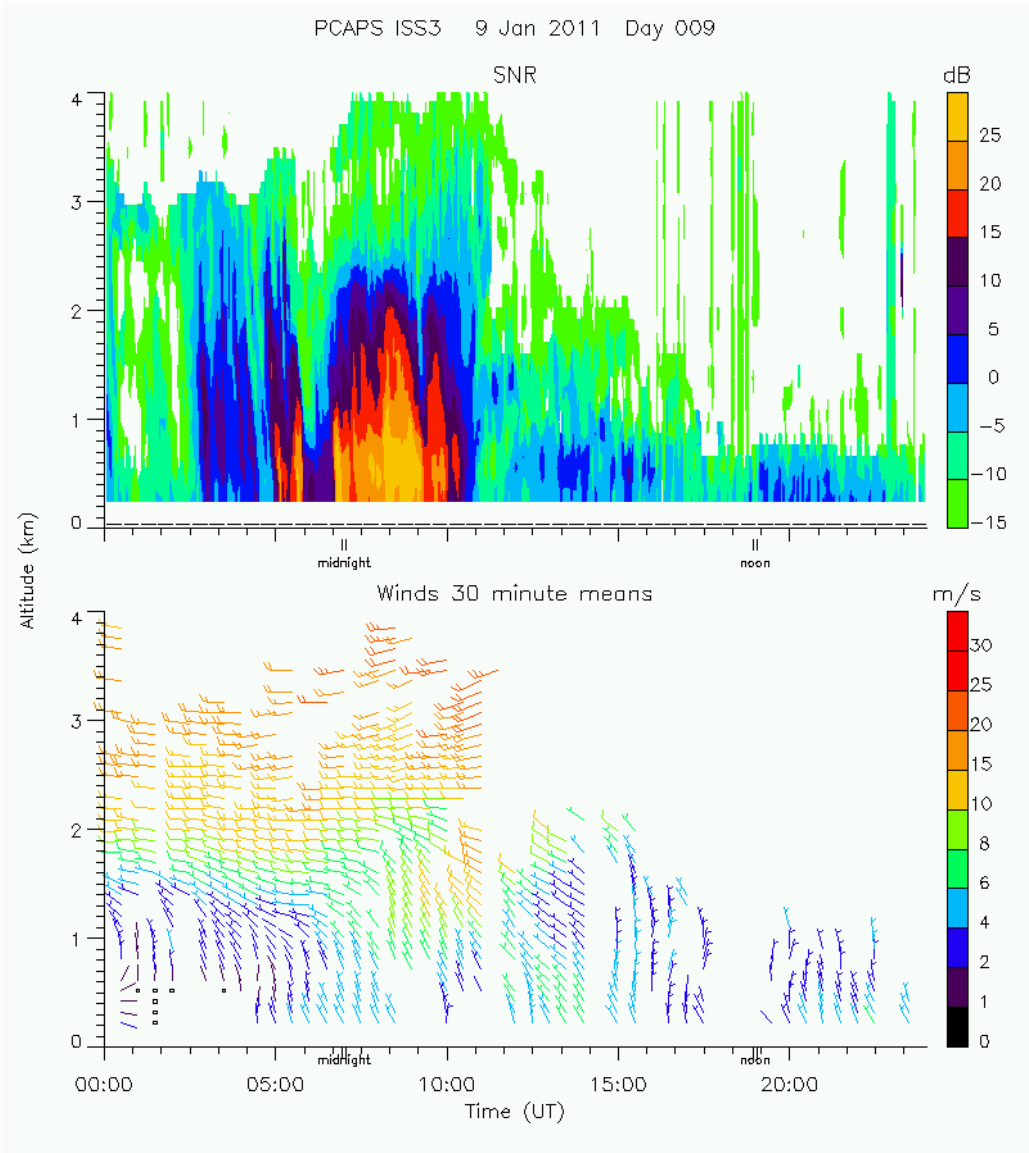

Figure 2.22. Data from commercial 915 MHz Doppler beam steering wind profiler located at the same site. SNR (top) and winds (bottom) during the same time period.

Figure 2.23 shows the wind computation rate for the 449 MHz wind profiler vs. the 915 MHz wind profiler over a two month period from December 10, 2010 to February 7, 2011. The x-axis shows the percentage of time that winds were computed for a given altitude. The 915 MHz profiler is able to compute some winds up to 4.5km while the 449 MHz wind profiler can compute winds up to 5.5km. The 449 MHz profiler has a problem computing winds below 500m, this is due to only using a high mode (long pulse) throughout the project. An alternating low and high mode (short pulse/long pulse) will be implemented for future projects. In later testing, isolation circulators added to the output of the transmitter improved low range gate performance by attenuating pulses reflected from the antenna.

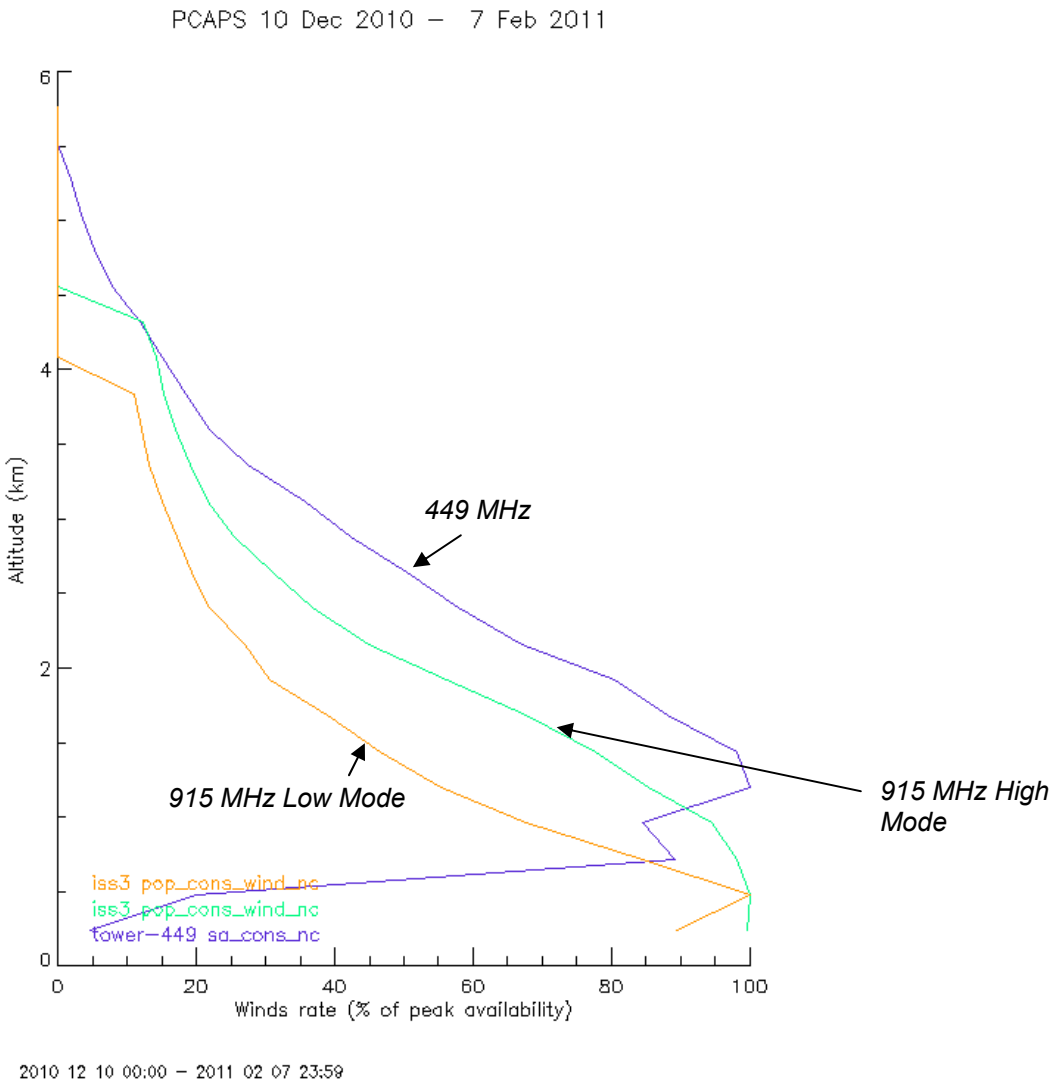

Figure 2.23. Comparison of 449 and 915 MHz wind rate vs. altitude over a two month time period at PCAPS.

The cold-air pool science that was studied at the PCAPS project was successfully observed by the new 449 MHz wind profiler and can be seen in the data. First it must be confirmed that there is an inversion observed. In Figure 2.24, radiosonde data from 3 January 2011 shows an inversion between 1.5-2.5 km. The inversion is confirmed in the detail shown in Figure 2.24(b) showing warmer air above colder air.

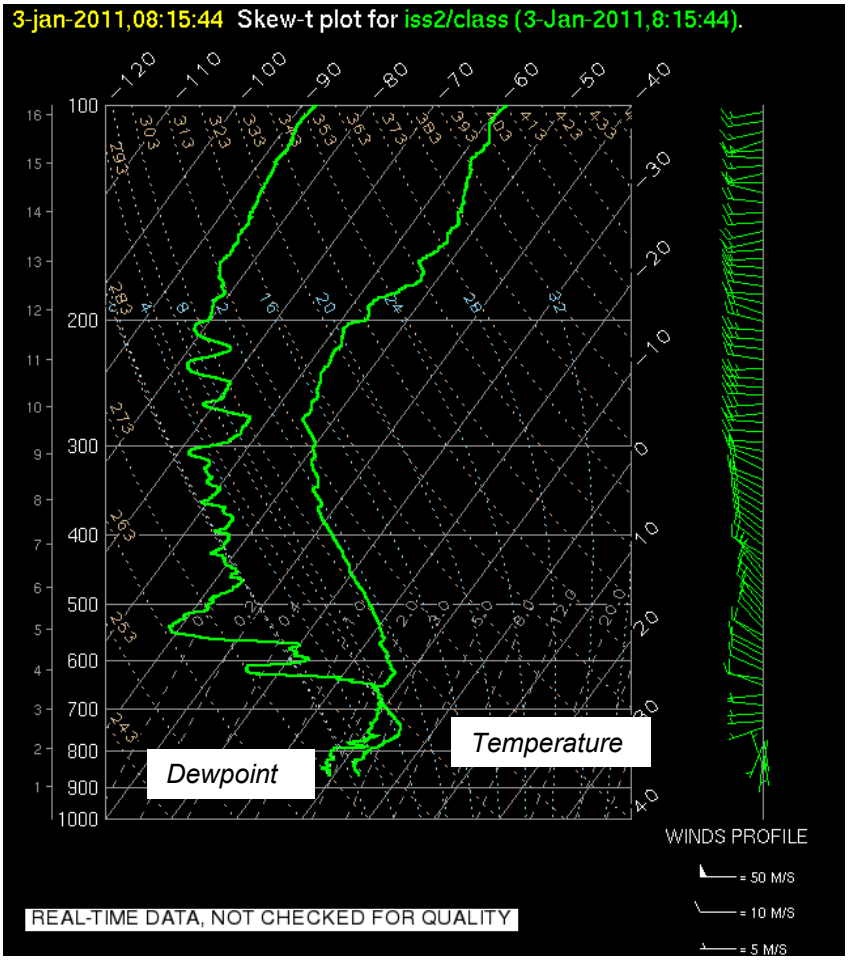

(a)

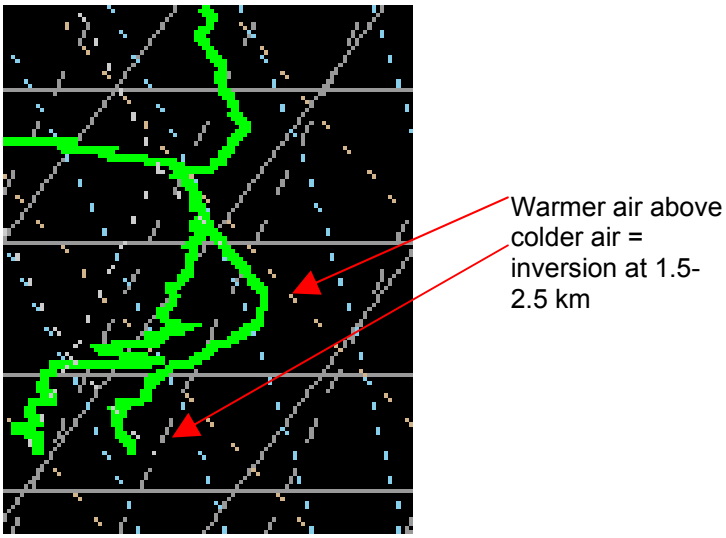

(b)

Figure 2.24.(a) Radiosonde data from Salt Lake City, Utah on 3 January 2011. The curve on the left is dewpoint and the curve on the right is temperature. (b) Detail of 1-4 km altitude showing inversion between 1.5-2.5 km.

This is also seen in the wind profiler SNR data shown in Figure 2.25 which shows a warm low-SNR layer above the high-SNR cold-air pool at 08 UT, about the same time the radiosonde is launched. The cold-air pool is also seen in the wind data. Looking at the bottom of Figure 2.25, the westerly winds above 1.5 km are influenced by the synoptic scale, while the winds below 1.5 km are southerly winds within the cold-air pool originating from the south end of the Salt Lake Valley.

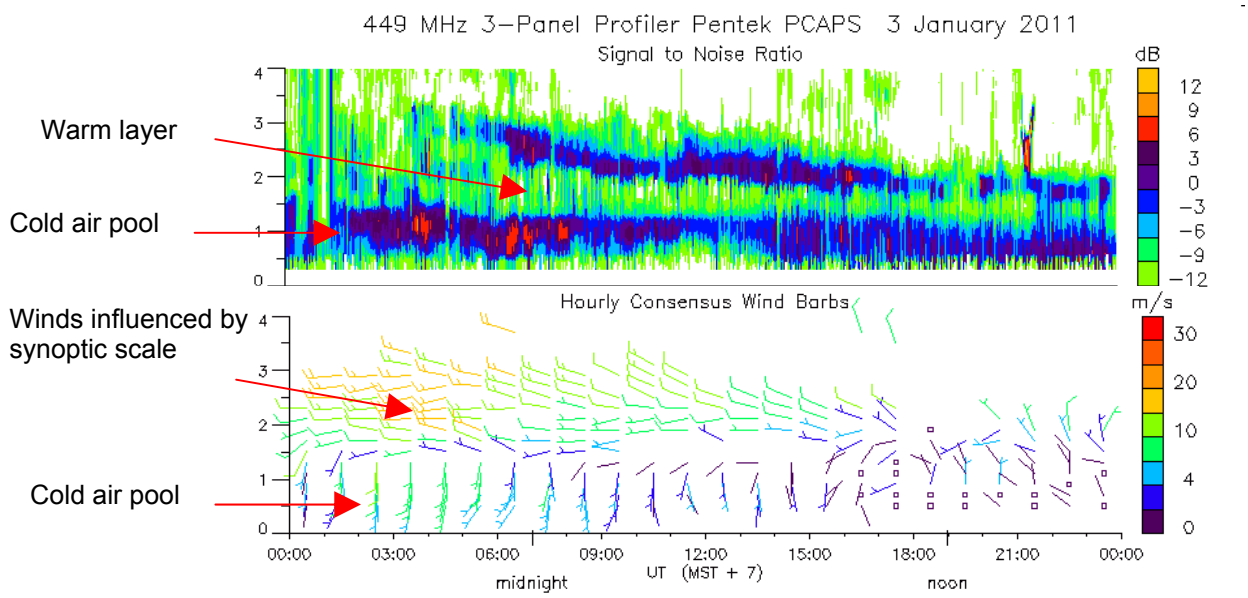

Figure 2.25. 449 MHz wind profiler data from Salt Lake City, Utah on 3 January 2011 showing persistent cold-air pool layers (top) and winds within the cold-air pool and winds influenced by the synoptic scale (bottom).

2.5 Conclusions

A new 449 MHz radar wind profiler has been demonstrated. This system will continue to be deployed in support of NCAR scientific field projects. A transmit section and three receivers were designed and tested. With low noise figure and adequate gain these receivers were tested to detect return signals with power levels down to -150 dBm.

An 80W LDMOS amplifier with PAE of 65% and gain of 13 dB was demonstrated at 449 MHz and used as a driver amplifier. Three 1 kW amplifiers based on LDMOS transistor technology were successfully combined to operate as a high power transmitter for this application. The 1 kW amplifiers have a PAE of 53.8% and a gain of 18.5 dB for operation up to 10% duty cycle. The new amplifiers were successfully integrated with the rest of the

radar system and deployed to the PCAPS field project at Salt Lake City, Utah. The winter cold-air pool phenomenon was observed with this system and wind measurements were compared with a 915 MHz DBS system operating at the same location. Results of this chapter have been published in [47].

Chapter 3

915 MHz Wind Profiler Radar Measurements

3.1 Introduction

In this chapter, wind measurements performed with the 915 MHz Multiple Antenna Profiler Radar (MAPR) and DBS wind profiler radars between 2008 and 2012 are presented. The first project presented is the Cloud and Precipitation Study (CPS) south of Miami, Florida in late summer 2008 using the 915 MHz spaced antenna MAPR system developed at NCAR in the late 1990s. Profiling of Winter Storms (PLOWS) is the next project that took place in Winter 2009-2010 in the Midwest United States using a mobile 915 MHz DBS wind profiler (MISS). The most recent field project is the Dynamics of the Madden-Julian Oscillation Project (DYNAMO) located south of Sri Lanka in the Indian Ocean using a ship-based 915 MHz DBS wind profiler. In addition to presenting observations from these projects, the goals of this chapter are:

- Demonstrate the need for higher altitude wind measurement capability than the current 915 MHz MAPR system;
- Motivate the need for clutter mitigation with the mobile 915 MHz DBS wind profiler (MISS) and on the ship-based 915 MHz DBS system.

3.2 The Cloud and Precipitation Study, Miami, FL

The Cloud and Precipitation Study (CPS) was a project led by Dr. Bruce Albrecht of the University of Miami in August and September of 2008 that studied convective storms in the Miami area and outer rain bands of tropical storms [53]. The 915 MHz Multiple Antenna Profiler Radar (MAPR) was deployed to this project. MAPR is an existing spaced antenna wind profiler radar that is capable of making rapid measurements to study the rapidly evolving structure of convective storms. Figure 3.1 shows a picture of the MAPR system at Miami, FL with a clutter fence and edge treatments described in Chapter 4. Note that this system does not beam steer or switch polarization. The array is divided up into four sections, each with its own receiver.

Figure 3.1. The MAPR 915 MHz spaced antenna wind profiler radar at the Center for Southeastern Tropical Advanced Remote Sensing (CSTARS) in Miami, FL.

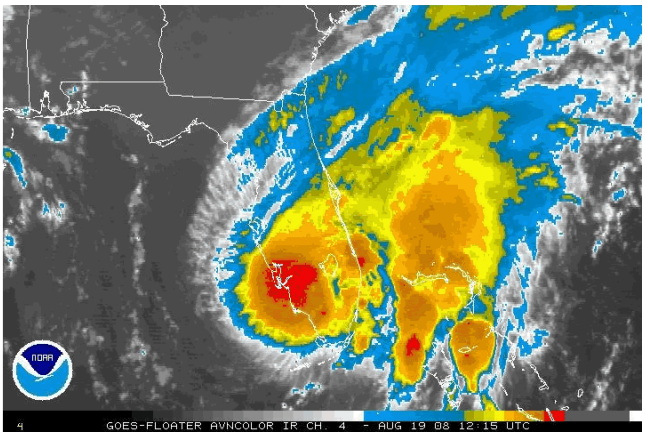

Figure 3.2. GOES satellite data showing the extent of Tropical Storm Fay on August 19th, 2008.

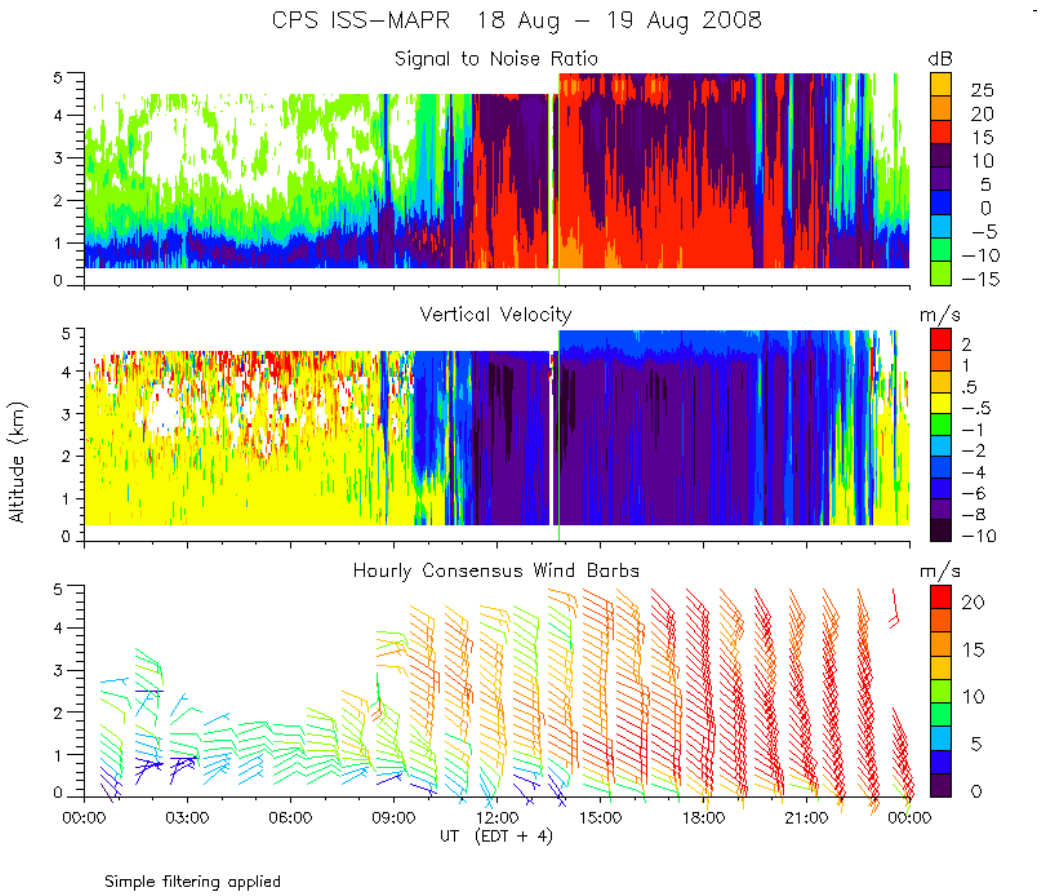

Figure 3.3. MAPR 915 MHz wind profiler data showing the passage of a rain band between 11-21 UT. Rain is indicated by the high SNR and negative vertical velocity. The winds intensify from 10 m/s to 20 m/s as Tropical Storm Fay passes over the area.

During this project, Tropical Storm Fay passed over Miami, FL on August 19, 2008, resulting in the closure of many offices and businesses. GOES satellite data shows the general extent of Tropical Storm Fay on August 19th in Figure 3.2. MAPR continued observations over this time and recorded data from one of the rain bands of the storm is shown in Figure 3.3. In the MAPR data, the passage of a rain band from Tropical Storm Fay is seen between 11-21 UT. The rain band is indicated by the high SNR and negative vertical velocity due to rain. Also, the winds increase from 15 m/s southeasterlies (wind from the southeast) to 20 m/s south-southeasterlies during the passage of the rain band. Around 14 UT the profiler mode was changed from clear-air mode to rain mode in order to observe higher altitudes. Because of the high humidity content of the air in this tropical region the refractive index variations are large compared with dry climates. This means the wind profiler radar SNR in general is higher in Miami, FL than Boulder, CO. An area for improvement can be seen in the data from 03-07 UT, where winds are calculated only

for altitudes from ground level up to about 2 km. The limited height range does not allow observation of the veering winds aloft. A 449 MHz system would most likely observe higher altitude winds because the scale of the turbulence it observes is larger and therefore contains more energy and produces a stronger refractive index gradient.

3.3 Profiling of Winter Storms, Midwest USA

The Profiling of Winter Storms (PLOWS) project was a project that studied winter storms with a goal to improve the 0-48 hour precipitation forecast [54]. Winter storms were studied during February-March 2009 and December-February 2010 in the Midwest US (Illinois, Indiana, Iowa, Minnesota, Missouri, Nebraska, and Wisconsin). The NCAR Mobile Integrated Sounding System (MISS) was deployed to this field project and included a 915 MHz wind profiler radar mounted on a trailer pulled behind a truck, Figure 3.4. This system is powered by a generator so that it can be operated at any location without a easily accessible power outlet.

Figure 3.4. The MISS 915 MHz wind profiler radar.

To keep this system portable and quick to set up, there is no clutter fence or edge treatment on the antenna array as described in the next chapter. This can result in higher sidelobe levels than the traditional 915 MHz wind profiler with clutter fence and edge treatments. Data from the MISS 915 MHz wind profiler radar is shown in Figure 3.5. Inconsistency in the winds is noticed from ground level up to about 700m between 06-15 UT and highlighted by the red box in the figure. This same inconsistency is not seen in the radiosonde data from 08:37 UT (Figure 3.6).

A closer look at the SNR data (Figure 3.7 top) reveals the consistent clutter at a range of 500m (highlighted by a red box) produced by a wind turbine as noted in the logbook. Fortunately the NCAR Improved Moments Algorithm (NIMA) [55] is able to filter some of the clutter out, however there is still gaps in the data such as the gap at 10 UT where low altitude winds are lost below 500m (Figure 3.7 bottom).

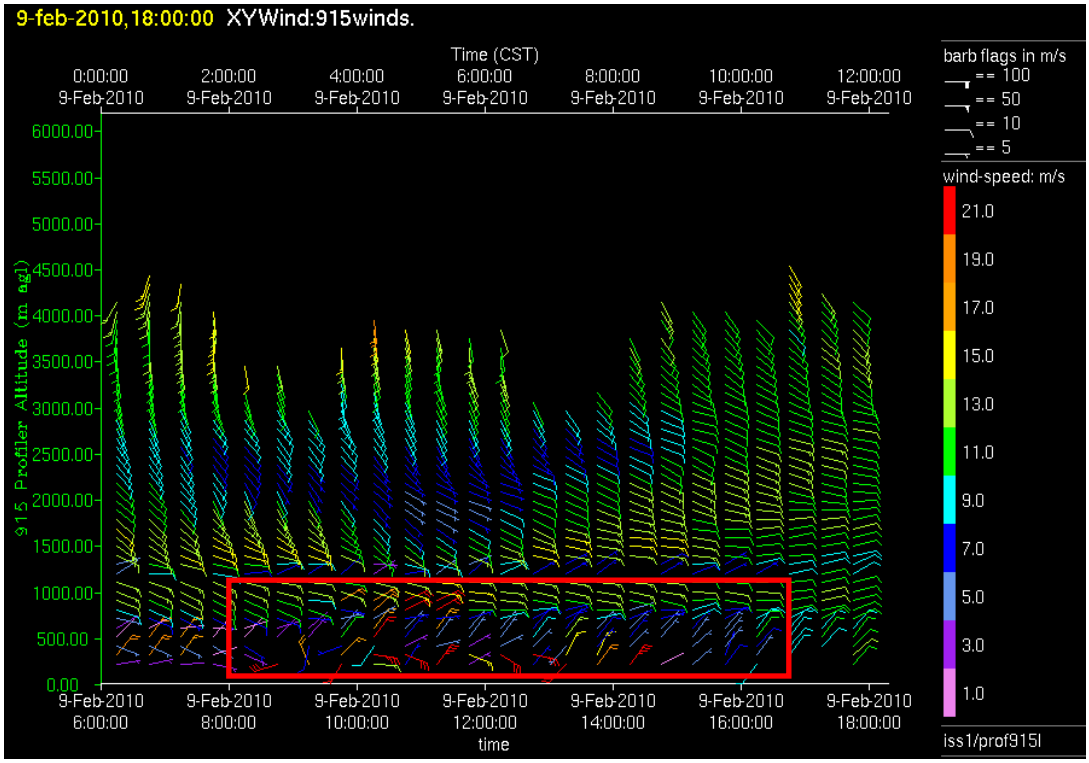

Figure 3.5. Unfiltered wind measurements from the MISS 915 MHz wind profiler radar at Fort Atkinson, WI.

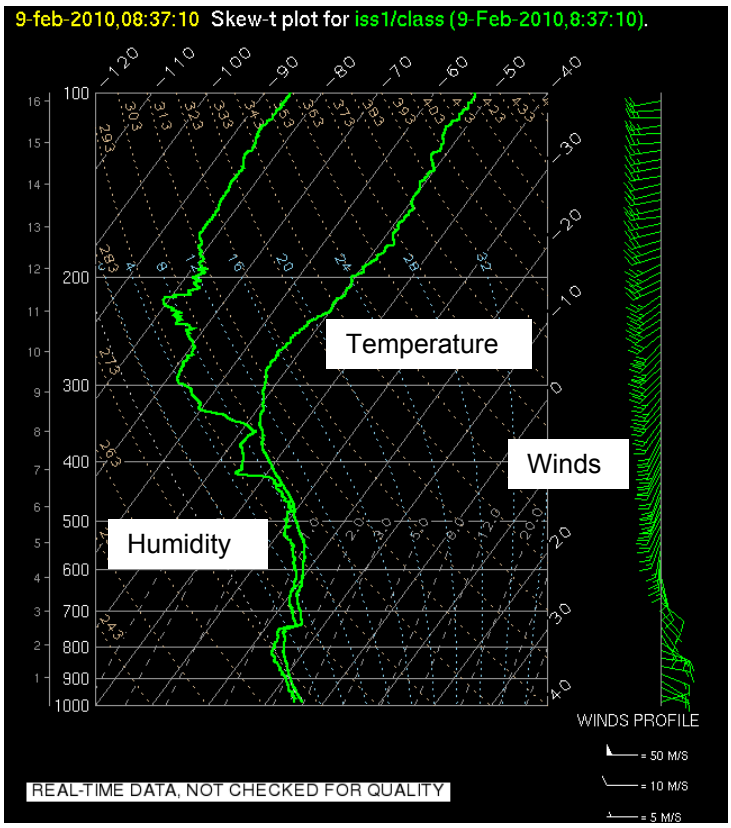

Figure 3.6. Radiosonde data at 08:37 UT at Fort Atkinson, WI. Altitude profile up to 16 km. Less inconsistency in winds at 500m altitude than wind profiler data.

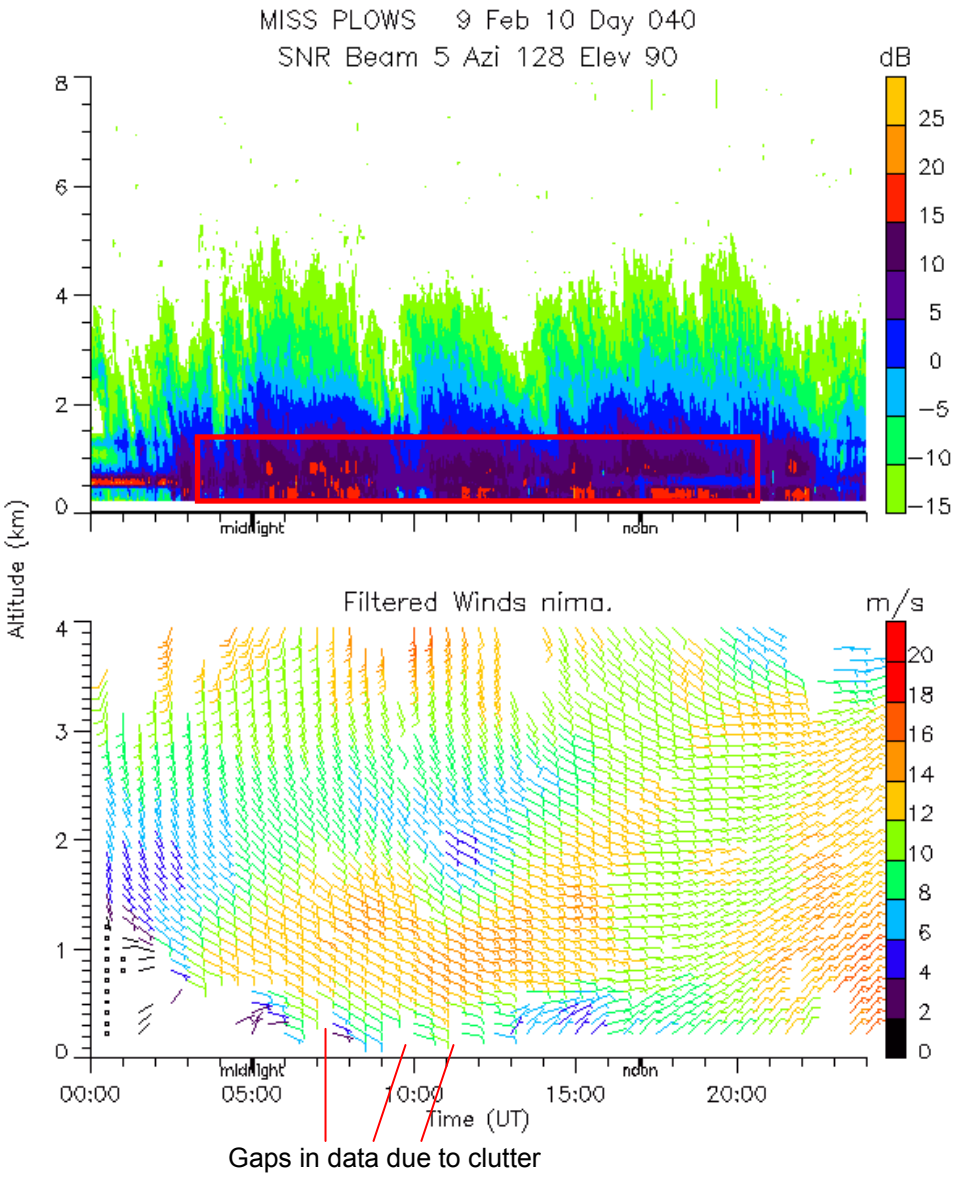

Figure 3.7. 915 MHz Wind Profiler Radar data at Fort Atkinson, WI showing wind turbine clutter in the SNR plot (top) at a range of 500m. This results in the loss of some wind data in the 0-500m range around 10UT.

3.4 Dynamics of the Madden-Julian Oscillation, Indian Ocean

From August 2011 until February 2012 the DYNAmics of the Madden-Julian Oscillation project (DYNAMO) studied the Madden-Julian oscillation in the Indian Ocean. Much like the El Niño / La Niña weather pattern in North / South America, the Madden-Julian oscillation (MJO) is large scale climate pattern centered over the Indian Ocean. The MJO affects weather phenomena that originate in the Indian and Pacific Ocean areas. In the coastal areas of the

Western US, the MJO is known to influence a local weather phenomena known as the Pineapple Express. The Pineapple Express is precipitation that approaches that West Coast of the US from the direction of Hawaii (named Pineapple Express because many pineapples are grown in Hawaii). As shown in Figure 3.8, the Pineapple Express is influenced by the MJO about 7-10 days before the event and brings precipitation to the West Coast of the United States from the direction of Hawaii in the Pacific Ocean [56]. The weather anomaly approaches the area of Hawaii and becomes a "Pineapple Express" about 3-5 days before it approaches the West Coast of the US.

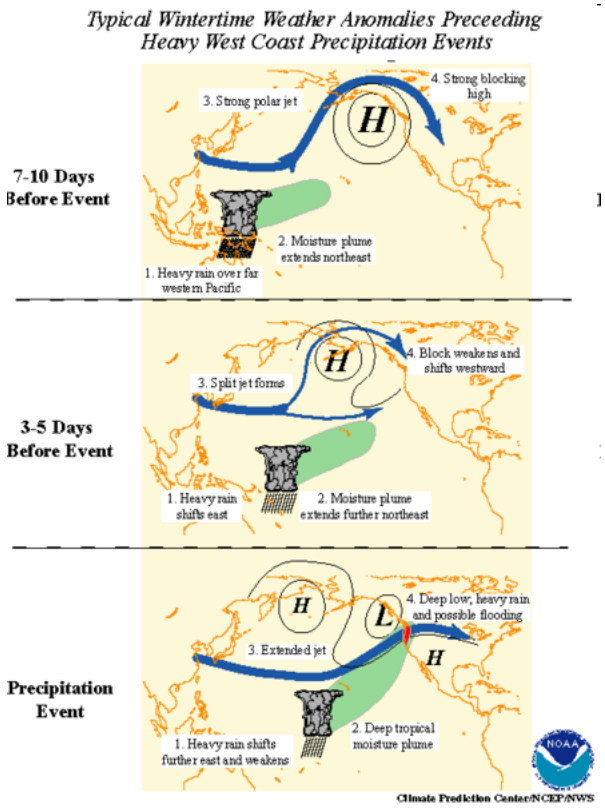

Figure 3.8. Influence of the Madden-Julian Oscillation on weather phenomena in the Western United States, such as the Pineapple Express (from[56]).

To study the MJO, a network of radars and radiosonde (weather balloon) stations were deployed at different sites in the Indian Ocean as shown in Figure 3.9 [57]. NCAR wind profilers were deployed to a ground-based station at the island of Diego Garcia and a ship-based station at 80E in the Indian Ocean (SE Ship).

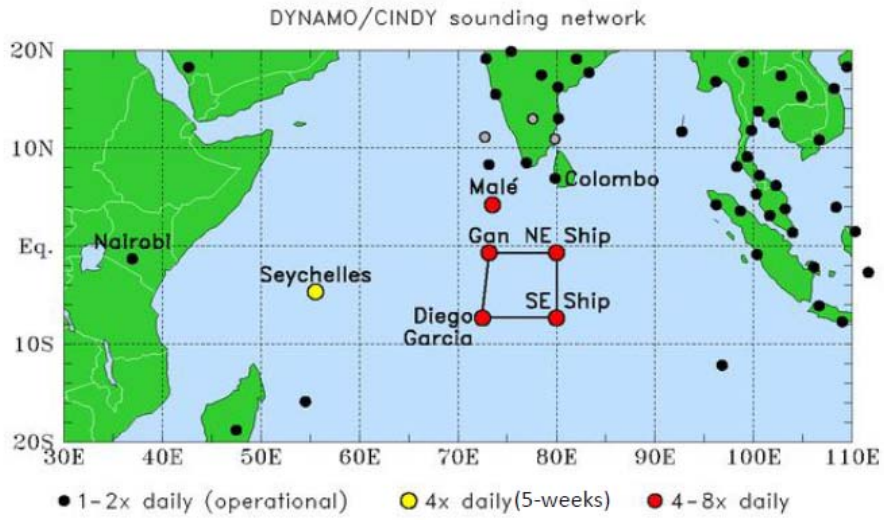

Figure 3.9. Locations of ship and ground-based radars and radiosonde stations for the Dynamo project (from [57]).

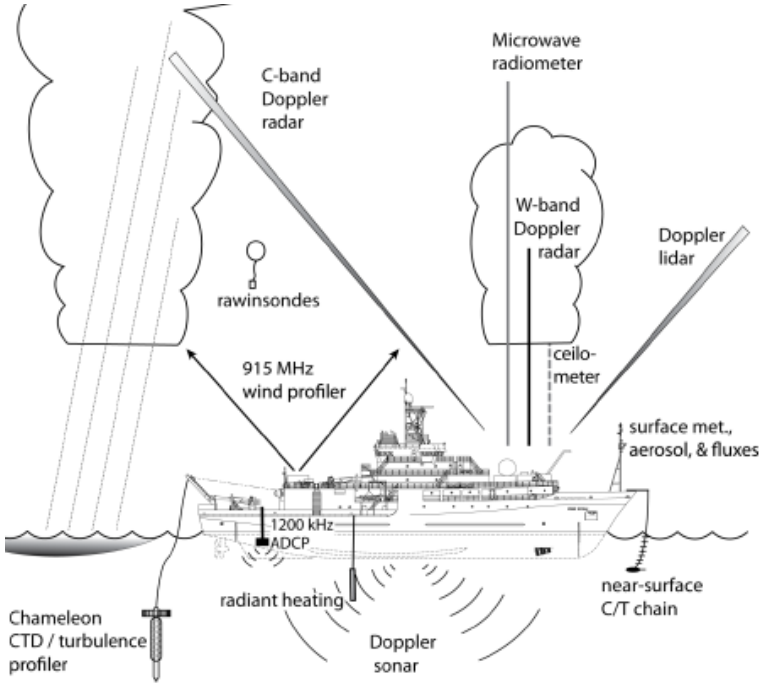

Figure 3.10. Placement of the NCAR wind profiler radar on the aft deck of the Roger Revelle (from [58]).

An NCAR 915 MHz wind profiler was placed on the Research Vessel Roger Revelle. The Roger Revelle is operated by the Scripps Institution of Oceanography at UC-San Diego. The 915 MHz wind profiler was installed at

Darwin, Australia on the aft deck of the ship (see Figure 3.10) during a setup period from August 19-28, 2011. Wind data was taken by the system starting on August 29, 2011 en route to Cocos Island, Australia. After the September 5, 2011 stop at Cocos Island wind data were taken in the Indian Ocean area primarily south of Sri Lanka at 8S, 80E. Four port calls were made at Phuket, Thailand with the last call on January 8, 2012. The last leg of operations was en route to Durban, South Africa where the Wind Profiler was taken off of the ship on February 12, 2012.

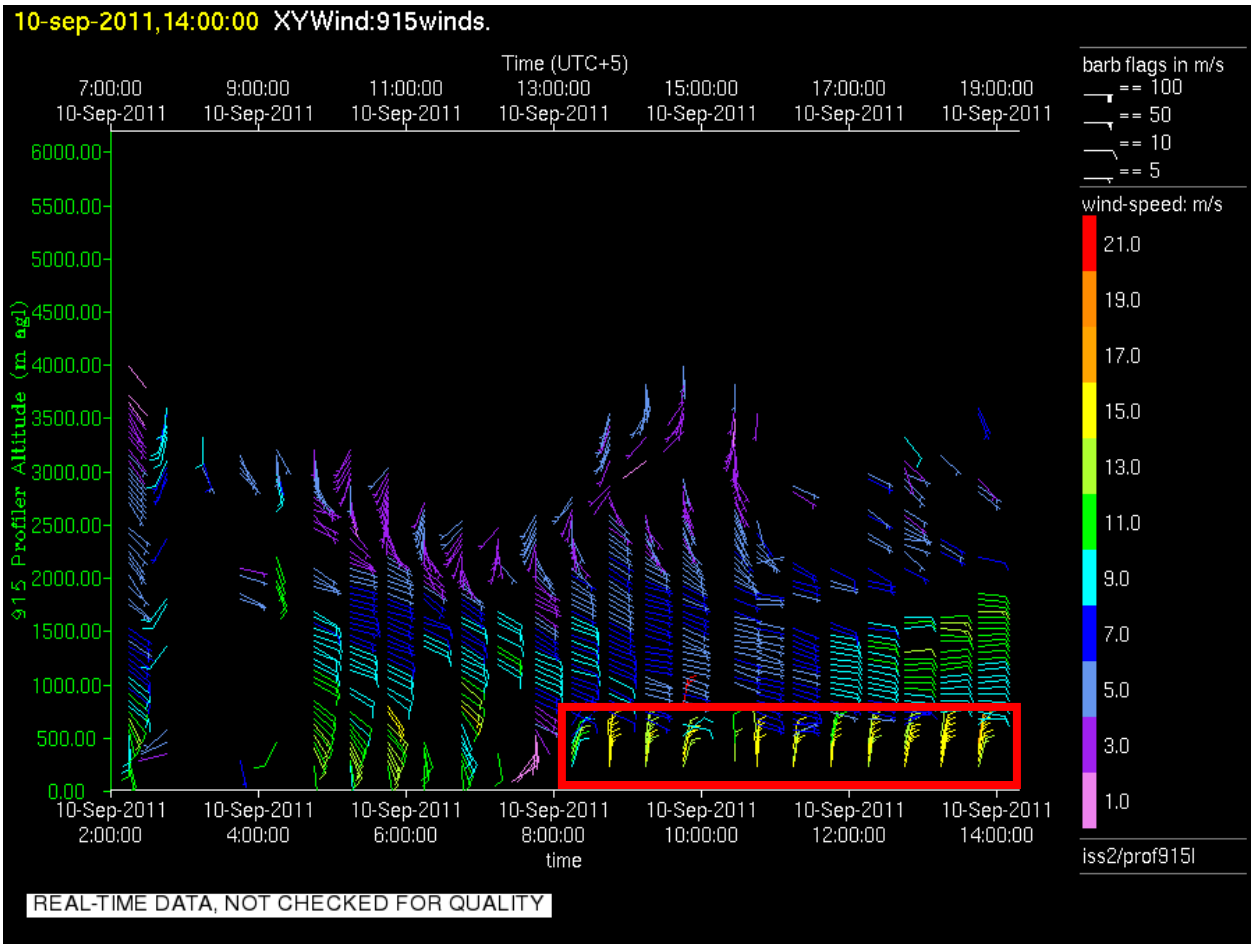

Figure 3.11. 915 MHz wind profiler data from the R/V Revelle in the Indian Ocean. Incorrect winds influenced by sea clutter are highlighted with a red box.

A sample of wind profiler data taken during the author's time on the ship is shown in Figure 3.11. This data shows mostly easterly winds from 1-2 km and southerly winds around 3 km during the time 02-14 UT on September 10, 2011. SNR levels allowed computation of winds from an altitude of about 200m up to about 4 km. Figure 3.12

shows radiosonde data at 11:18 UT on the same day with east-southeasterly winds up to 2 km and southerly winds from 3-5 km.

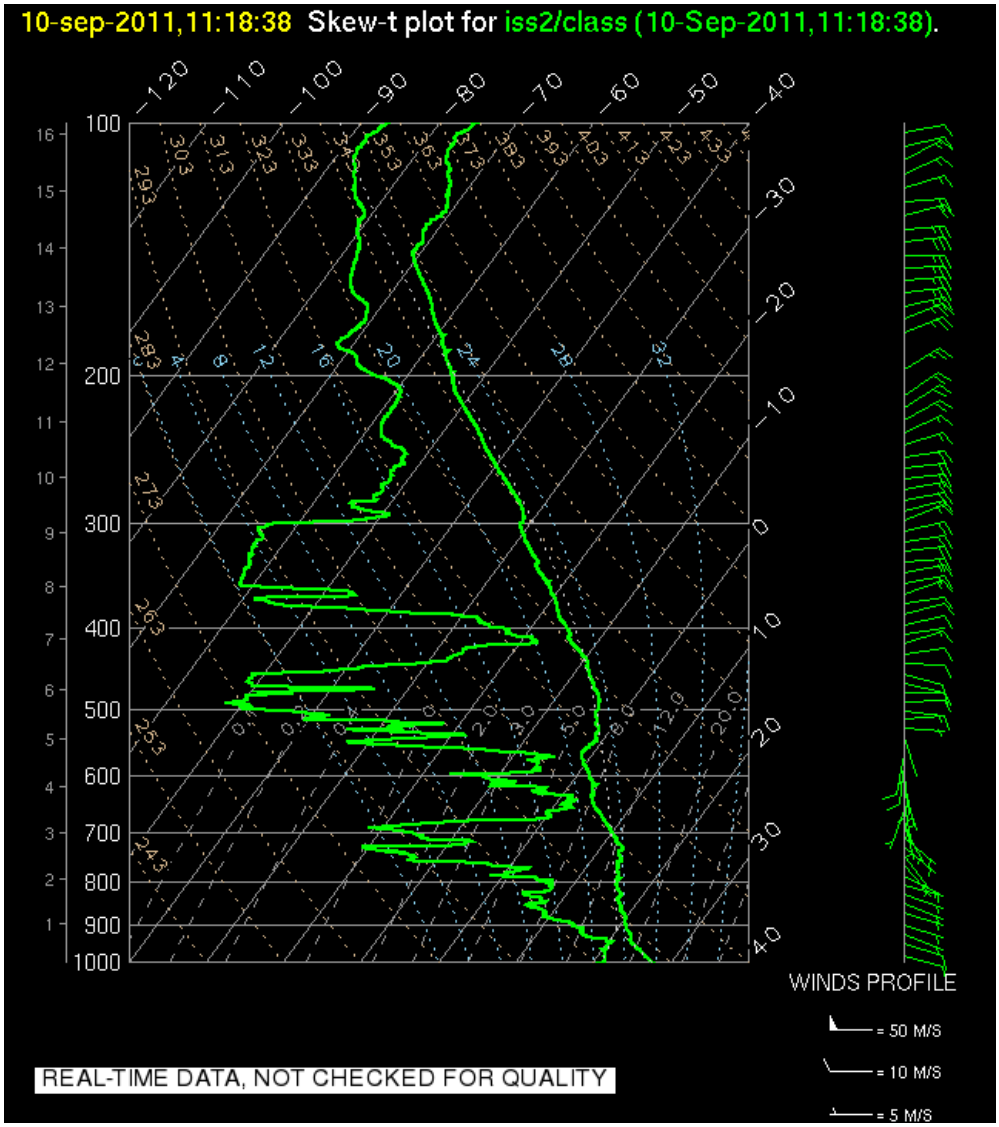

Figure 3.12. Radiosonde wind profile data, including skew-t temperature (right curve) and humidity (left curve) profile from the R/V Revelle in the Indian Ocean.

During the leg from Cocos to Phuket starting on September 5, comparisons were made between the wind profiler, launched radiosondes, and the NOAA High Resolution Doppler Lidar (HRDL), Figure 3.13. The NOAA

HRDL is a beam steered lidar that can determine horizontal winds like a wind profiler radar [59]. Because the lidar requires aerosols for backscatter, the altitude coverage is lower than a wind profiler radar.

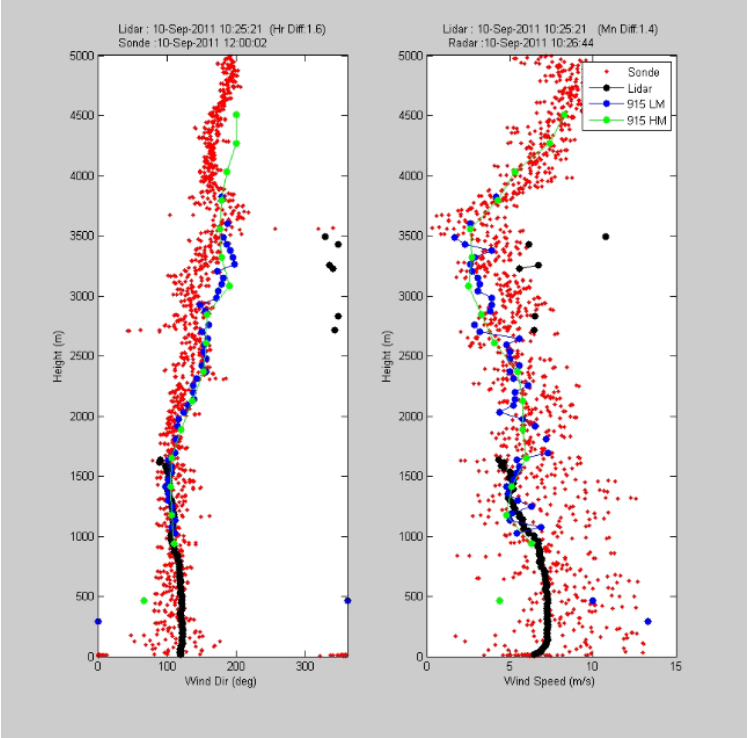

Figure 3.13. Comparison of radiosonde, NCAR 915 MHz wind profiler low mode (LM), high mode (HM), and NOAA HRDL Doppler lidar winds. Sea clutter prevents computation of wind profiler radar winds below 1 km (from Alan Brewer, NOAA).

As seen in the data, the radiosonde has very fine vertical resolution, but there is a wide variance. Because of the motion of the radiosonde while it travels through the air, the indicated GPS wind speed varies as much as 5 m/s. Also, because the radiosonde was only launched twice per day during this time period, the amount of time between the radiosonde measurement and an interesting radar or lidar measurement can be significant. Looking at both sides of Figure 3.13 (wind direction and wind speed), the 915 MHz wind profiler is not able to compute accurate winds below 1 km, but it is able to compute winds up to 4.5 km, while the lidar is only able to compute winds up to about 1.7 km. The reason that the wind profiler can not compute winds below 1 km is because of moving sea clutter. Comparing Figure 3.11 and Figure 3.13, the northerly winds (highlighted with a red box) in Figure 3.11 from 08-14 UT up to 1 km can now be interpreted as erroneous because of sea clutter. The NCAR Improved Moments

Algorithm will be applied to this data in the future, and will reduce the effect of sea clutter, but gaps in the data will be frequent because of the strong sea clutter signal. Especially when the ship is moving, ocean waves are moving away from the ship at velocities similar to winds. Because ocean waves are a hard target, they reflect much more of the radar pulse than atmospheric turbulence. Figure 3.14 shows the NCAR 915 MHz wind profiler surrounded by the R/V Revelle ship structure and the Indian Ocean with many ocean waves.

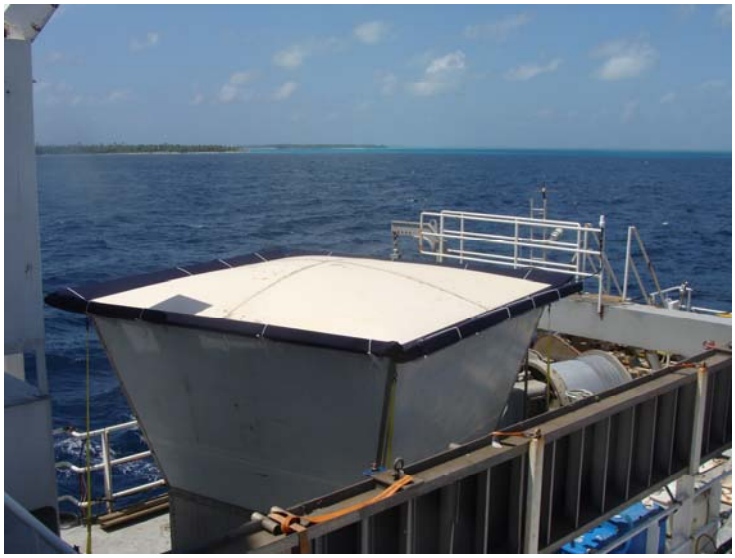

Figure 3.14. NCAR 915 MHz wind profiler radar installed on Research Vessel Roger Revelle. Ocean waves produce reflections from the sidelobes of the radar which result in sea clutter.

While Figure 3.13 presented a case of no wind profiler radar winds below 1 km, sometimes the radar is able to compute winds at lower altitudes such as in cases when the ship is not moving or there is calm seas. Figure 3.15 presents such a case. Here the wind profiler radar is able to see winds down to 250m and up to 5 km. The HRDL is able to see winds up to 2.1 km. The HRDL is dependent backscatter from aerosols, so the height coverage is limited to lower altitudes where aerosols are abundant. The difficulty measuring winds below 1 km because of sea clutter is a motivation to analyze the 915 MHz wind profiler antenna sidelobe levels. This will allow exploration of designs that may allow reduction of the sidelobe levels and sea clutter.

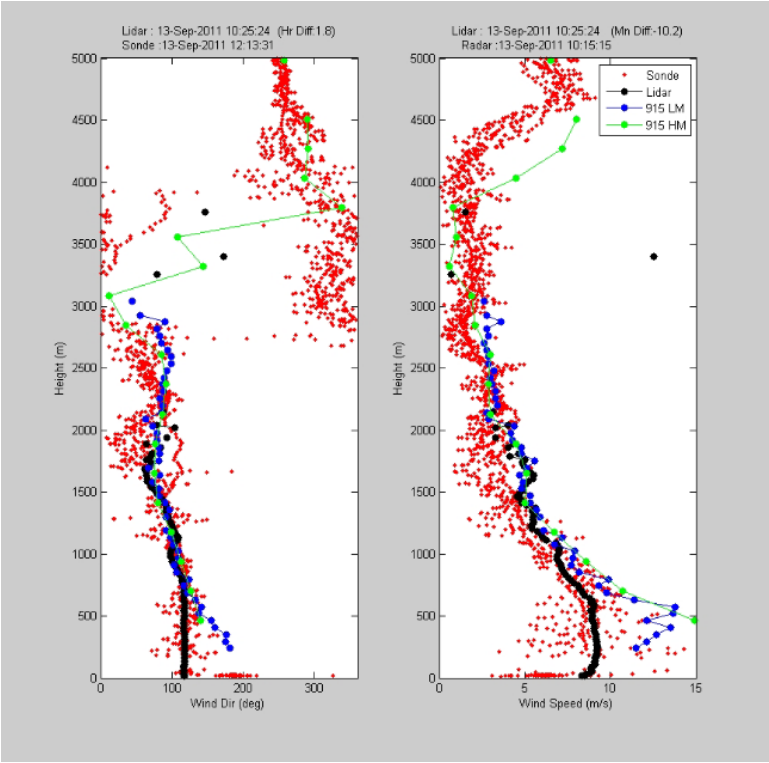

Figure 3.15. Comparison of radiosonde, NCAR 915 MHz wind profiler low mode (LM), high mode (HM), and NOAA HRDL Doppler lidar winds. In this case, the wind profiler radar is able to detect winds down to about 250m (from Alan Brewer, NOAA).

3.5 Conclusions

This chapter has shown wind measurements using the 915 MHz wind profiler radars from projects studying weather phenomena such as convective storms, tropical storms (CPS), winter storms (PLOWS), and large scale climate phenomena such as the Madden-Julian Oscillation (DYNAMO). These measurements show the limitations of the existing 915 MHz wind profiler radars in high clutter environments such as near wind turbines or on a ship with sea clutter. Reduction of antenna sidelobe levels is proposed for clutter mitigation and will be explored in the next chapter. Recent results presented in this chapter are planned for a publication in the Journal of Atmospheric and Oceanic Technology.

Chapter 4

Wind Profiler Radar Antenna Sidelobe Reduction

Wind profiler pulsed radars measure small (on the order of 80 ppm) changes in electric permittivity of clear air resulting from turbulence caused by wind at heights ranging typically from 150m to 18km. For example, 915-MHz DBS wind profiler radar was first described by Ecklund et al. [6] with improvements by Russell and Jordan [60]. Another method is interferometric, referred to as a "spaced antenna" method [15], in which the horizontal winds are computed from the time lag of correlated signals between receivers. For example, the National Center for Atmospheric Research (NCAR) 449-MHz spaced antenna wind profiler is described in [47]. The spaced antenna method was also used by the existing Multiple Antenna Profiler Radar (MAPR) [9].

Both types of wind radars have main antenna pattern lobes pointing in the zenith direction, and sidelobes of the radiation pattern result in clutter from ground or sea. The 200-dB attenuation of the transmitted radar signal requires high transmitted power levels on the order of 1-kW peak power with a 10% pulse duty cycle and 1μs long pulses. Thus, for a 1-kW transmitter, sidelobes at -40 dB can contribute clutter returns on the order of -100 dBm, while the desired averaged Bragg scattered signal is at a -150dBm level. Therefore, reduction of sidelobe levels is important for reducing radar returns from ground clutter and is commonly done with a modified 3-D metallic ground plane referred to as a clutter fence. Clutter fences have been used by radars since the 1960's [61]. These shields can be relatively large, e.g. in [62] the size of the main radiator is 18m while the total size of the antenna with the far-field clutter fence is 150m. For a portable and easily deployable radar, it is of interest to have a compact clutter fence, with the fence located as close to the antenna as possible. In [63], diffraction off edges of a ground plane are discussed theoretically, and [64] demonstrated a slot-based modification of the fence edges for further sidelobe attenuation. More recently, a US patent proposes using an array of $\lambda/4$ corrugations as an edge treatment [65], as

implemented in the 915MHz radar shown in Figure 4.1. Electromagnetic simulations of clutter fences have been presented by Rao et al [104] using Uniform Theory of Diffraction and Physical Optics techniques. However, to the best of our knowledge a systematic study of clutter fences and edge treatments using full wave simulation has not been presented.

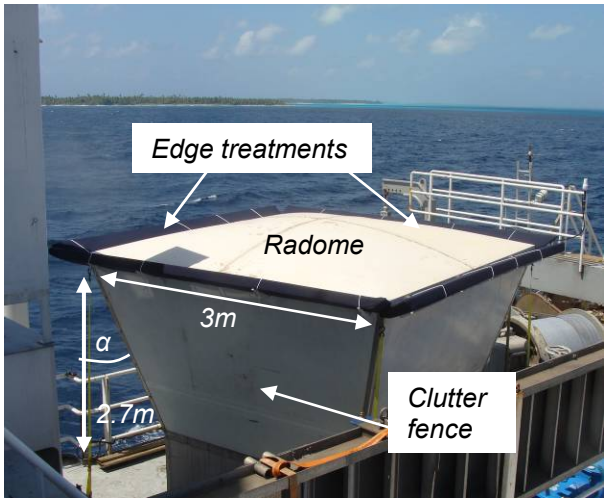

(a)

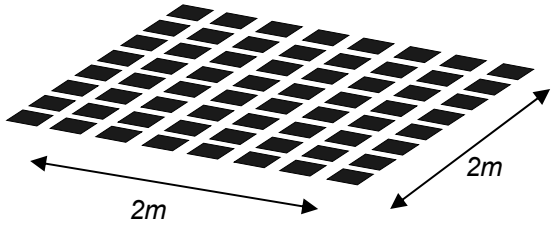

(b)

Figure 4.1.(a) Photograph of 915 MHz wind profiler radar antenna covered by a radome and surrounded by a clutter fence with four edge treatments. (b) Diagram illustrating zenith-looking 915 MHz 64-element square patch antenna array under radome.

A number of full-wave electromagnetic simulation techniques were evaluated to determine wind profiler radar antenna patterns. Element patterns were initially determined by using the Method of Moments [107] code with AWR EMSight and then later using the 3D Finite-element Method with Ansoft HFSS. Another Method of Moments implementation called NEC-2 (the Numerical Electromagnetics Code) was evaluated for initial simulations of the wind profiler radar clutter fence. NEC-2 requires converting all structures to wire grids and is more resource

intensive than FEKO. FEKO is a 3D Method of Moments code that was successfully used to simulate the whole antenna structure including the clutter fence. FEKO also has an implementation of the Multilevel Fast Multipole Method (MLFMM) which allows faster computation of Method of Moments problems with the use of less memory.

The goal of this chapter is to evaluate sidelobe reduction methods for existing 915-MHz and 449-MHz wind profiler radar systems which can be easily implemented in hardware and with a potential to mitigate effects of clutter for land-based, land-mobile, and ship-based operations.

4.1 915-MHz Beam-Steered Antenna with Clutter Fence

Over 100 existing wind profiler radars use a 915-MHz 8x8 square patch antenna array, each with two cross-polarized feeds, which is located under the fiberglass radome in Figure 4.1. The sides of the clutter fence consist of metal coated panels typically at α=15° relative to zenith, depending on the system. Referring to Figure 4.2, the top edges of the clutter fence have an edge treatment mounted at β=22° above horizontal. The edge treatment consists of parallel quarter-wave deep corrugations spaced at less than a tenth of a free space wavelength [65]. The specific antenna shown in Figure 4.1 has 13 corrugations, as shown in the Figure 4.2 simulated geometry.

The existing beam steering system uses both horizontal and vertical linear polarization. In order to better understand effects of edge modifications on array patterns, the existing array was simulated with a full-wave electromagnetic field simulator (Feko from EMSS, Inc. [66]). First, the 22° edge treatment angle was confirmed to result in the most sidelobe suppression for a fixed clutter fence panel angle of 15°, as summarized in Figure 4.3. Figure 4.3 shows the sidelobe levels near the horizon for the E-plane. Edge treatments with β = 22° provide about 3 dB lower sidelobe levels in the E-plane. The angle of the edge treatment is critical to within a few degrees; a vertical edge treatment has a 5 dB higher sidelobe level than no treatment. A horizontal treatment has a sidelobe level similar to no edge treatments. The trace for "β=22.5° and separated" shows that connecting the corrugations with the fence electrically does not result in any significant reduction in sidelobe levels.

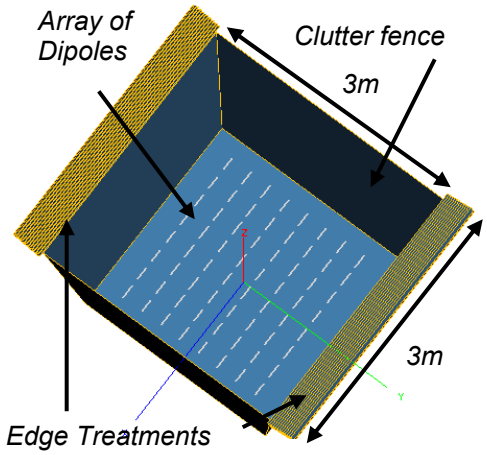

(a)

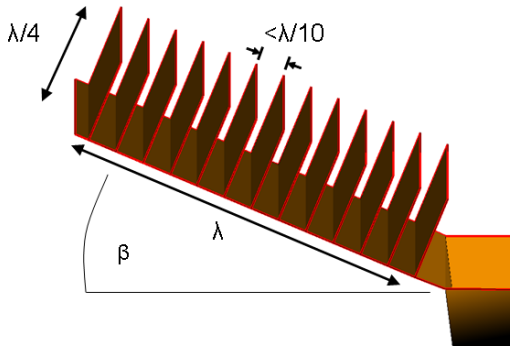

(b)

Figure 4.2. (a) CAD Model of 915-MHz clutter fence with two edge treatments. (b) Detail CAD drawing of a single edge treatment with dimensions.

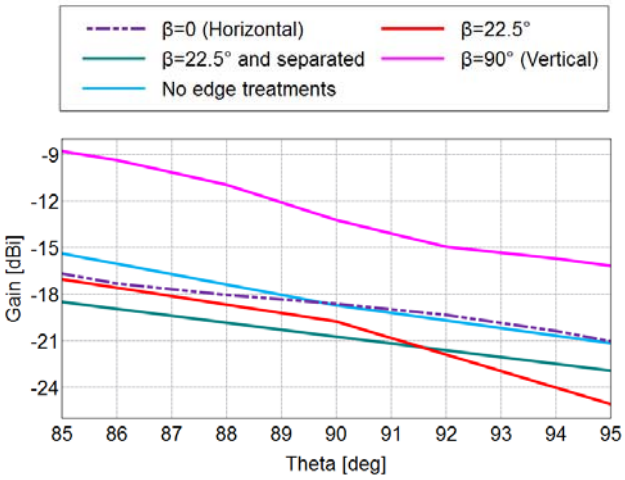

Figure 4.3. Simulation of E-plane sidelobe levels near the horizon between θ=85-95° using different configurations of clutter fence edge treatment. Note that θ is the angle of the computed antenna pattern while β is the angle of the edge treatment.

The simulations are performed for arrays without a clutter fence and compared to various cases of clutter fence geometries in order to understand the effects of edge treatments that could lead to the most effective design. E and H-planes of an 8x8 array of linearly-polarized half-wave dipoles are considered instead of the square patch antennas to simplify the simulation due to memory constraints encountered in this electrically-large three-dimensional problem. The general conclusions should not depend on the exact antenna element, as the radiation pattern of a patch is similar to that of a dipole above a ground plane. For this simulation, the angle of the edge treatments is kept at β = 22° (Figure 4.4). The standard radome is also not considered in the simulation for simplicity, since it should not affect the radiation pattern. The edge treatments in the simulations consist of metal corrugations about λ/4 deep, λ wide, with a spacing less than λ/10 [65], as shown in Figure 4.2(b).

The entire structure in Figure 4.2(a) was simulated with Feko for the following cases: (1) no clutter fence; (2) clutter fence with no edge treatment; (3) edge treatment as shown in Figure 4.2(a) on the two sides perpendicular to the H-plane; and (4) edge treatment on all four sides of the fence. The following conclusions can be made from the results plotted in Figure 4.4:

- the sidelobe level is unacceptably high in the H-plane without a fence; thus a clutter fence should be used;
- the E-plane sidelobes degrade with a clutter fence, so the natural conclusion would be to only have a clutter fence with two sides for the H-plane. However, since the existing radar uses dual polarization, this is not possible;

- for the same reason, the edge treatments on all 4 sides of the fence should be used, and they reduce the horizontal sidelobe level by about 5 dB at the horizon.

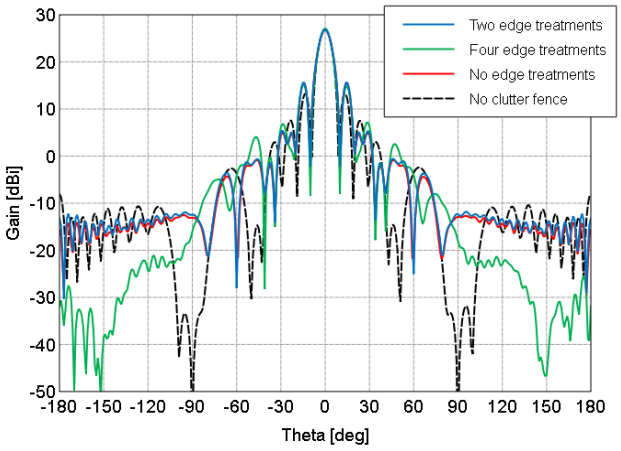

(a)

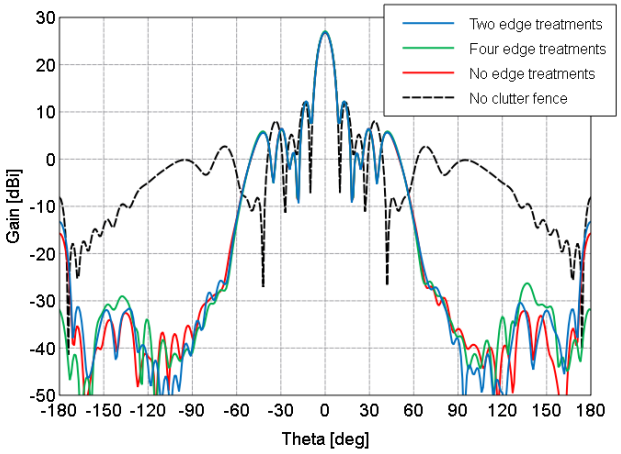

(b)

Figure 4.4. (a) Simulation of E-plane and (b) H-plane pattern for the four cases described in the text, and for β=22°and α=15°.

After determining that the edge treatment is beneficial on all sides of the clutter fence for dual-polarized arrays, variation of the number and spacing of the corrugations was explored. It was found that the $\lambda/10$ spacing of $\lambda/4$ corrugations was optimal, and that the performance does not vary as long as the total length of the corrugations is larger than a free-space wavelength λ.

4.2 Sidelobe Reduction in the New 449 MHz Spaced Antenna Array Architecture

The antenna used in the 449 MHz spaced antenna wind profiler radar is a modular design using three 18-element linearly-polarized circular patch antenna hexagonal arrays (54 elements total). Circular patch antennas in hexagonal arrays have been considered by simulations earlier by Law [48]. This type of antenna array is chosen for the wind-profiler due to its low sidelobe levels which minimize ground clutter and allow operation without a clutter fence. The basic unit array is the 18-element hexagonal array, shown in Figure 4.5(a). This array can be used as a sub-array and lends itself easily to modular and scalable arrays. Figure 4.5(b) shows a simulated antenna pattern for the 18-element hexagonal array, using Ansys HFSS [49] for the single element and a standard array pattern calculation (following Law [48]) for the array. The simulation in 4.5(b) neglects effects of mutual coupling.

The circular patch antennas are probe-fed for linear polarization [50] and implemented using single sided copper FR4 circuit board material separated from the ground plane by a 13-mm thick Nida-Core H8PP honeycomb material which has a relative permittivity of ε_r=1.12. The ground plane is a 3-mm thick aluminum sheet chosen for light weight and mechanical stability. Figure 4.6 shows HFSS electric field simulation of a single 449 MHz pin-fed circular patch antenna with these dimensions and plot of the electric field vector illustrating the polarization of the patch antenna.

These antennas were custom built for this application and Figure 4.7(a) shows the construction by Warner Ecklund of one of the 6-element parallelograms that make up the hexagonal array. The patch feed points are 5.8 cm offset from the center for a good match to 50-Ω SMA connectors. After adding a 25-mm thick polystyrene flat radome above the patches, the return loss of the antenna was measured using a vector network analyzer calibrated to the SMA connector. The match is better than -15dB at the 449-MHz design frequency, as shown in Figure 4.7(b).

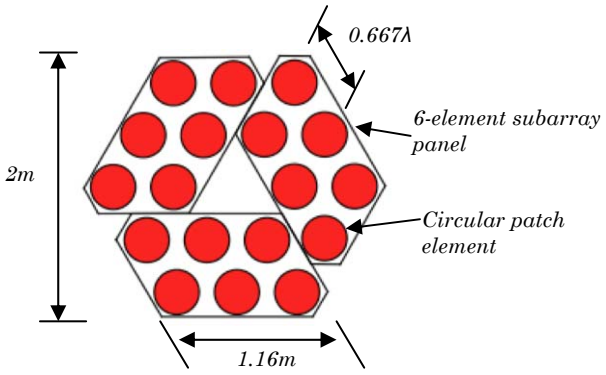

(a)

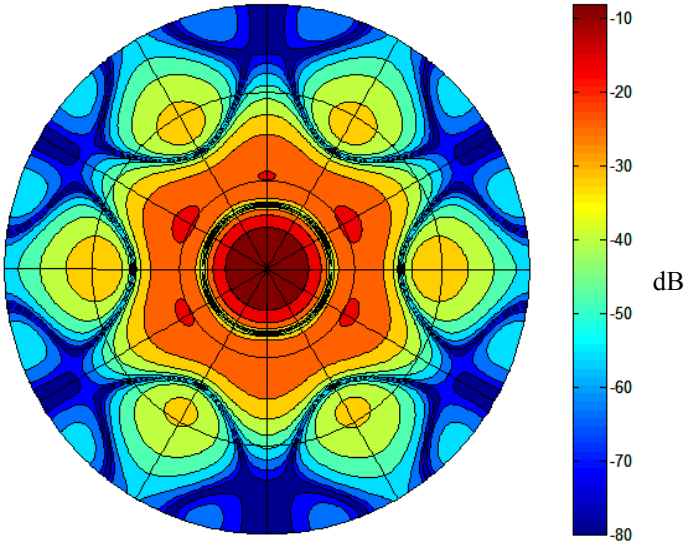

(b)

Figure 4.5. (a) 18-Element hexagonal circular patch antenna array for 449 MHz. (b) Antenna pattern simulation following Law [48]. Scale is in dB with reference to main beam. Edge of circle is horizon, center is zenith. Sidelobes at horizon are more than 35 dB less than main beam.

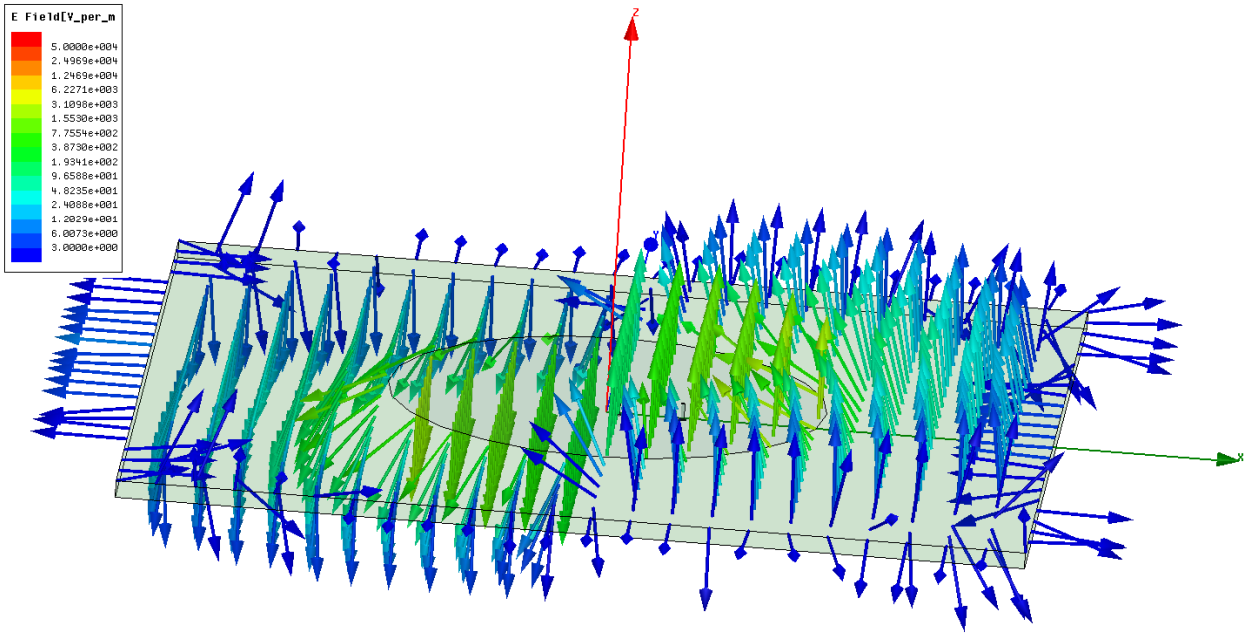

Figure 4.6. Electric Field simulation of a single 449 MHz pin-fed circular patch antenna on a 13-mm thick substrate with ε_r=1.12. Plot of electric field vector illustrating the polarization of the patch antenna.

Due to the size of the array and the large wavelength, it was not possible to measure the antenna pattern in an anechoic chamber. To confirm the important low sidelobe levels, measurements were made at an outdoor antenna range as illustrated in Figure 4.8(a). The 18-element array was driven by a calibrated 18-way splitter network. The sidelobe levels were measured at horizon (0°), 12.6° and 20°, limited by the height of the telephone pole used for the probe antenna in the far field of the array. The measurement data is shown in Figure 4.8(b), confirming the low sidelobe levels at the horizon. The measured -30 dB level is sufficient to eliminate the need for a ground clutter fence.

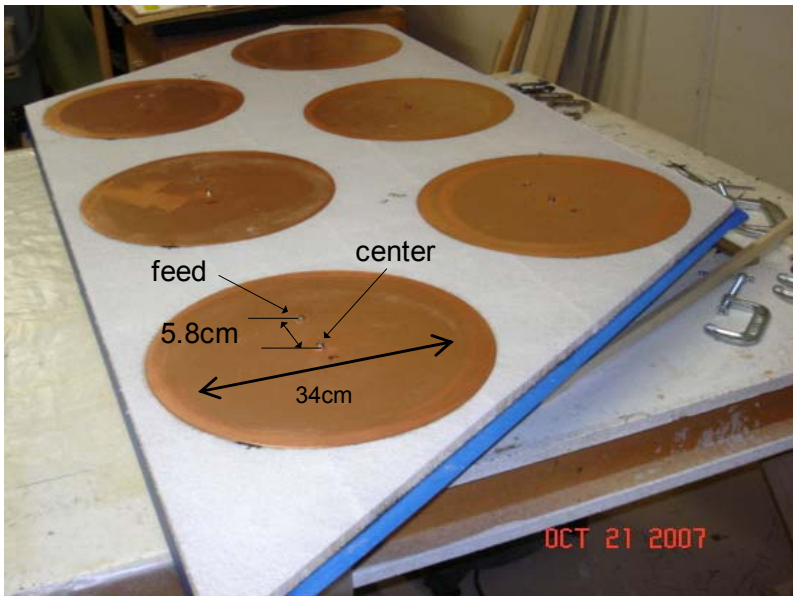

(a)

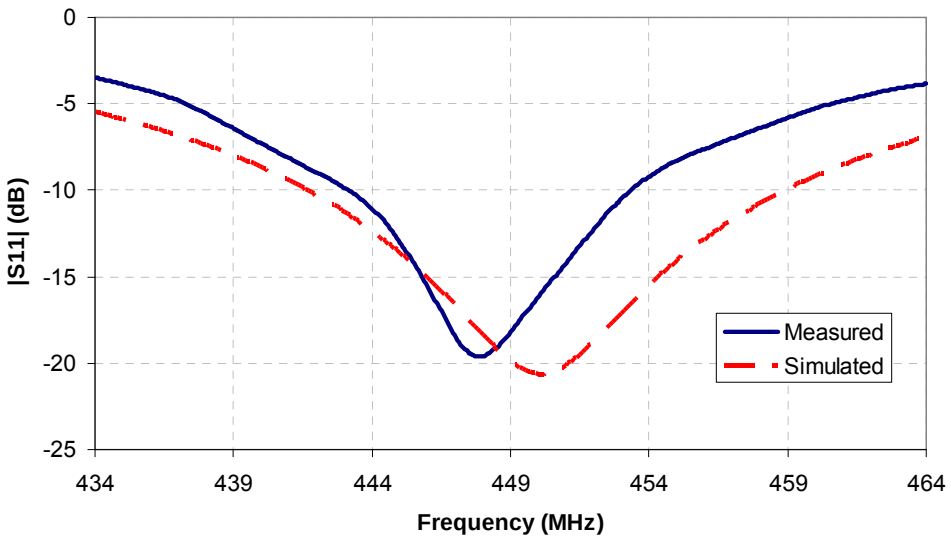

(b)

Figure 4.7. (a) Photograph of a 6-element subarray from Figure 4.5(a), showing the patch probe feed position. A 25-mm thick polystyrene layer is epoxied on top of the panel to protect against moisture. (b) Measured and simulated $|S_{11}|$ of one of the circular patch antennas.

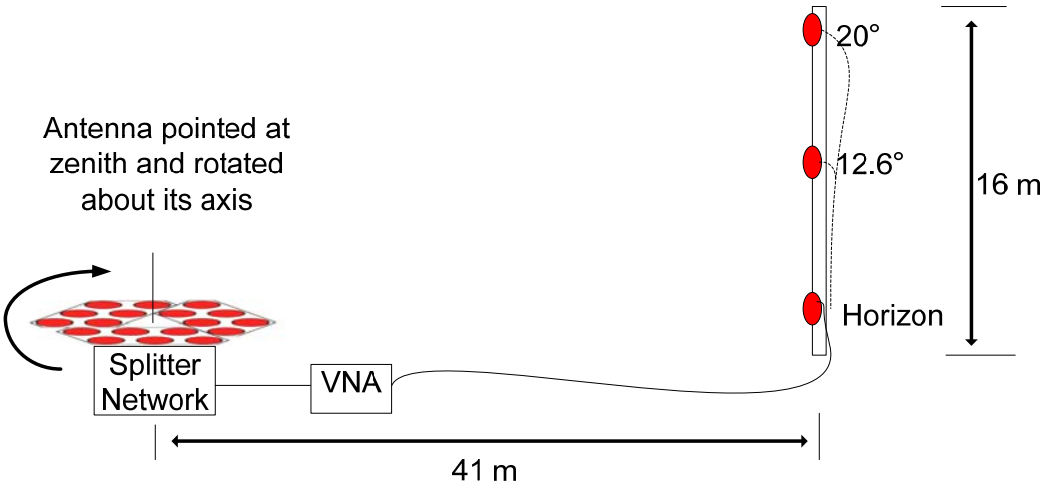

(a)

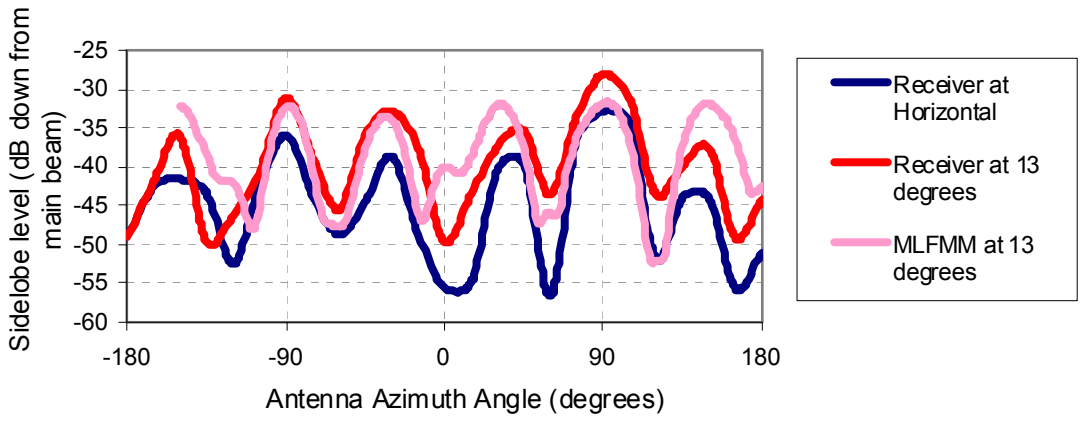

(b)

Figure 4.8.(a) Procedure for measuring 18-element antenna array sidelobes. Antenna is rotated about its axis for each elevation angle. (b) Single hexagon, 18-element array measured antenna sidelobe levels (receiver polarization oriented horizontally). Main beam is pointing at zenith.

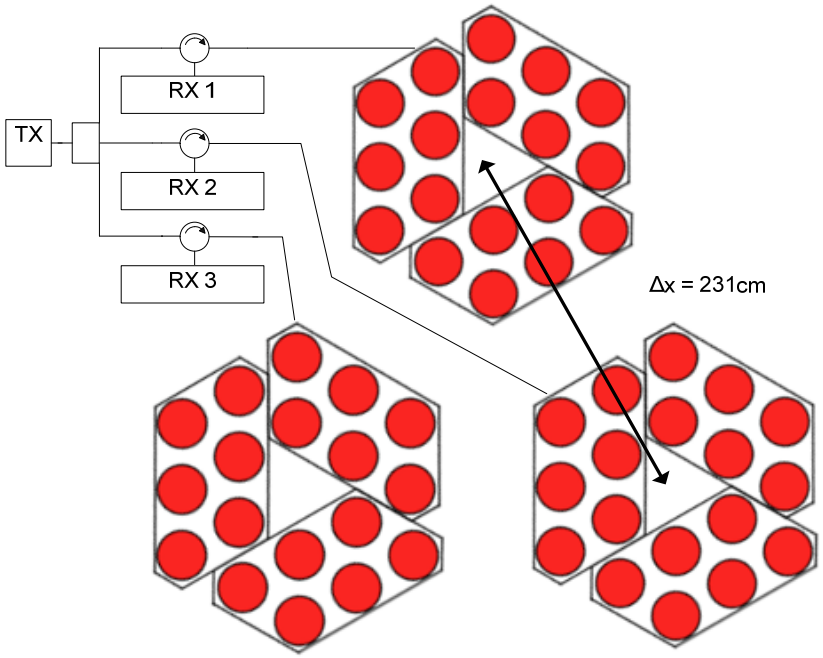

(a)

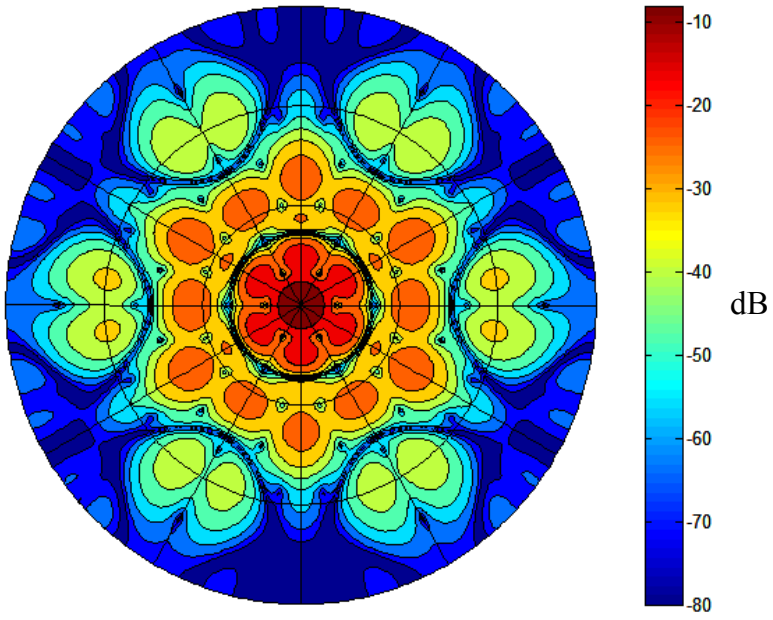

(b)

Figure 4.9. (a) 54-Element hexagonal circular patch antenna array for 449 MHz with connections to the transmitter and receivers as shown. The center to center spacing is Δx = 231cm. (b) Antenna pattern simulation. Scale is in dB with reference to main beam. Edge of circle is horizon, center is zenith. Sidelobes at horizon are more than 35 dB less than main beam.

After measurements confirming low sidelobe levels in the 18-element array, two additional 18-element arrays were built to complete the 3-receiver system with a total of 54 elements. The configuration and simulated antenna patterns for the 54 element array factor is shown in Figure 4.9(a) and (b). The size of the arrays were chosen to allow easy transport between field projects. After construction of the three arrays and their splitter networks and feed cables, phase and amplitude were measured at each element to confirm proper phasing of the antenna. This test was accomplished by using a VNA and a near field test patch positioned above each element in a repeatable manner. Amplitude data from one of the hexagons is shown in Figure 4.10.

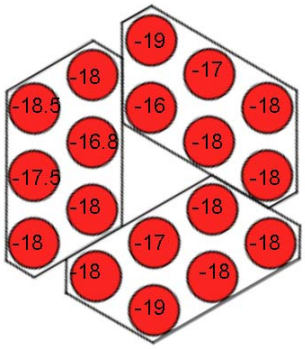

Figure 4.10. Amplitude check of each element of an 18-Element array using a VNA. A theoretical 54-way split is -17 dB.

This section has described the architecture of a 54-element circular patch array with 18-element hexagonal subarrays. The hexagonal array was chosen because it is modular and can be reconfigured into large 3, 7, or 19-hexagon arrays (each hexagon with 18 elements). The size of the hexagonal array allows easy transport between field projects. These arrays were designed to have low antenna sidelobe levels. Simulations of the design and measurements confirm the low sidelobe level performance. The results of this section are presented in [51] and [52].

4.3 Clutter Fence Effects for a 18-Element 449-MHz Hexagonal Patch Array

A new 449 MHz spaced-antenna array radar has been developed for wind profiling and is described in [47]. The lower frequency is chosen for higher SNR because the scale of the turbulence increases the Bragg scatter from clear air for longer wavelengths. In addition to 2-kW high-power and high-efficiency (60%) LDMOS power amplifiers in the transmitters [67], this wind profiler is designed to be modular and consists of several hexagonal antenna sub-arrays. Although the circular patch antenna elements and the hexagonal lattice considerably reduce the sidelobes [47], clutter is still limiting the radar performance. In contrast to the beam-steering antennas, in a spaced-antenna array the main beam always points in the zenith direction and the sidelobes do not vary during operation. Therefore, it is expected that a clutter fence will be even more beneficial than in the case of the 915-MHz antenna array.

Ideally, to minimize sidelobes, one would extend the clutter fence / extended ground plane as far as possible, but to maintain the portability of the system, the height is constrained to 1m. Simulations of a single hexagonal sub-array consisting of an 18-element array of circular patches were performed for a 1-m tall clutter fence, as shown in Figure 4.11. A vertical clutter fence was simulated for all cases except for the final 15° tilt simulation.

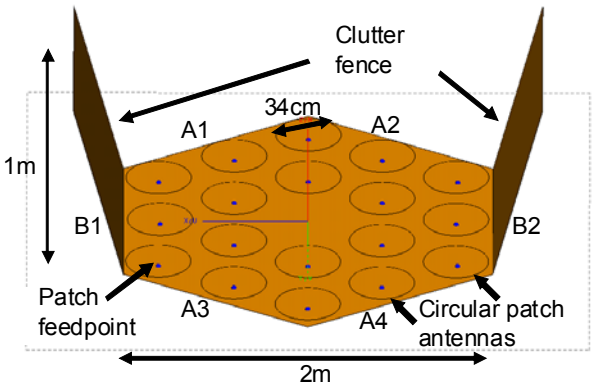

Figure 4.11. Layout of a 449-MHz 18-element circular patch hexagonal array with clutter fence at 15° tilt on sides B1 and B2, intersecting the H-plane. E-plane is parallel to red axis, H-plane is parallel to blue axis.

Figure 4.12 shows the sidelobe performance of the 449 MHz 18-element array in the E-plane and H-plane. Five different configurations were simulated: (1) no clutter fence; (2) vertical clutter fence on sides A1 through A4

(intersecting E-plane); (3) vertical clutter fence on sides B1 and B2 (intersecting H-plane); (4) vertical clutter fence on all sides; and (5) clutter fence on sides B1 and B2 with a 15° tilt.

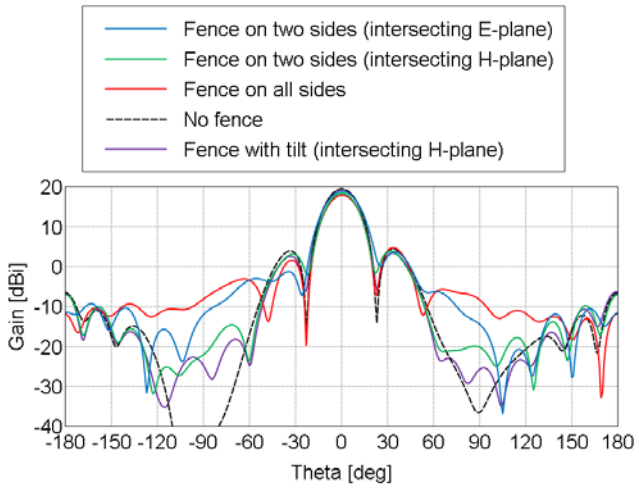

(a)

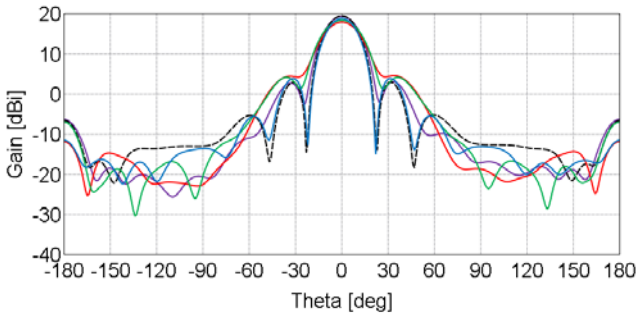

(b)

Figure 4.12. (a) Simulation of sidelobe levels in the E-plane and (b) H-plane. A vertical clutter fence was simulated for all cases except for the final 15° tilt simulation.

The results show that:

- the E-plane has better performance without any clutter fence (sidelobe levels at $\theta = \pm 90°$ are more than 40dB down from main lobe);
- the H-plane has the opposite response; sidelobe levels without the clutter fence are highest. H-plane sidelobe levels are lowest with a clutter fence on all sides;
- since a clutter fence on all sides causes the worst performance in the E-plane, a compromise is made by only adding clutter fence panels on the two sides that are intersecting the H-plane.

- a vertical clutter fence intersecting the H-plane still causes increased sidelobe levels in the E-plane. When the clutter fence is tilted outward 15° from vertical, the E-plane sidelobe levels near the horizon are decreased by about 5 dB.
- the edge treatments discussed earlier provided the most benefit to clutter fences intersecting the E-plane. Since the 449 MHz system has a fixed polarization and the beam is not steered, a clutter fence intersecting the E-plane is not recommended and the use of edge treatments is of limited benefit.

4.4 Antenna Height Effects for a 18-Element 449-MHz Hexagonal Patch Array

The other possible parameter that would affect sidelobe level is the height of the array above earth ground. Assuming sandy loam soil type (ε_r=2.55, tanδ=0.017), a simulation was performed for the 18-element circular patch array for 80cm and 20cm above ground, without clutter fence, and the co-polarized (horizontal) gain in the 5° elevation plane is shown in Figure 4.13(a). Validation measurements of the normalized pattern were performed in one accessible quadrant in the far field, Figure 4.13(b). This shows that, for a single array, the sidelobes can be reduced by 10dB by decreasing the height of the antenna above ground. However, this is less practical than having a fixed fence since ground properties and surroundings can vary in the field. Depending on soil type and moisture content, soil properties can vary between ε_r=2.5 to ε_r=20, and tanδ=0.0065 to tanδ=0.52 at 300 MHz [68].

Figure 4.14 shows a simulated configuration of three 449-MHz hexagonal arrays with two-sided clutter fences at 15° tilt intersecting the H-plane. Simulations show that two of the clutter fence panels facing the middle of the array can be removed without degradation of the horizontal sidelobe performance. Because each hexagon is an independent receiver, only one of the three hexagonal arrays is fed for this simulation of the receive antenna pattern. Since this antenna will almost always be constructed in a vertically pointed orientation above an earth surface, the model includes an infinite ground plane at that plane with a relative permittivity of 2.59 and dielectric loss tangent of 0.017 for soil and exact Sommerfeld integrals to model the ground. A 3-D plot in Figure 4.14(b) shows the total gain in dBi, for an array height of 1m above the ground, note that the front-to-back ratio is 18.4 dB.

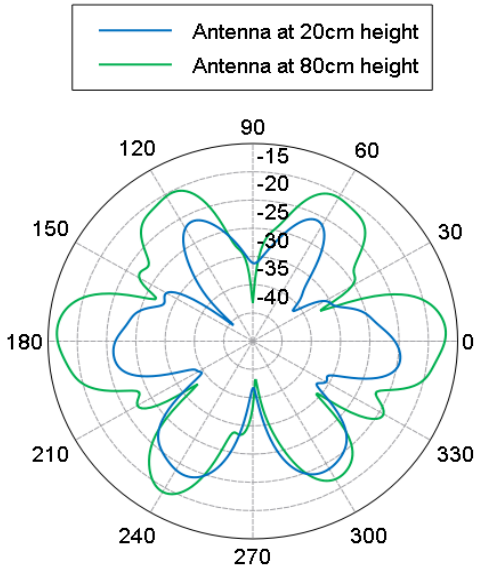

(a)

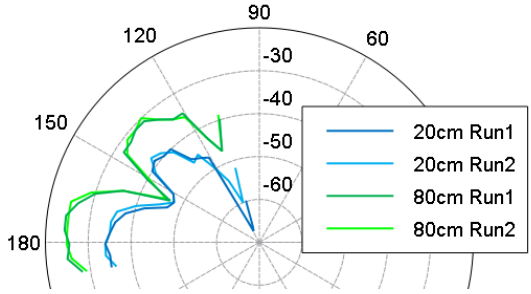

(b)

Figure 4.13. (a) Simulation of sidelobe levels (dBi) at elevation θ=85° for array at 20cm and 80cm heights. (b) Measurements of sidelobe levels (dBm) at 20cm and 80cm heights.

Figure 4.14(c) shows a plot of gain vs. azimuth at 10° elevation, for an array height of 1m above the ground. With a main lobe gain of 19.3dBi, the average and peak sidelobe levels (SLL) at 10° elevation can be calculated from the simulated data in this plot. The average sidelobe levels for the different configurations are summarized in Table 4.1. There is an average SLL difference of 2 dB between having a clutter fence and not having a clutter fence. The difference in peak SLL is 5 dB, so the fence is beneficial but less so than placing the array at an optimal distance above a known ground.

(a)

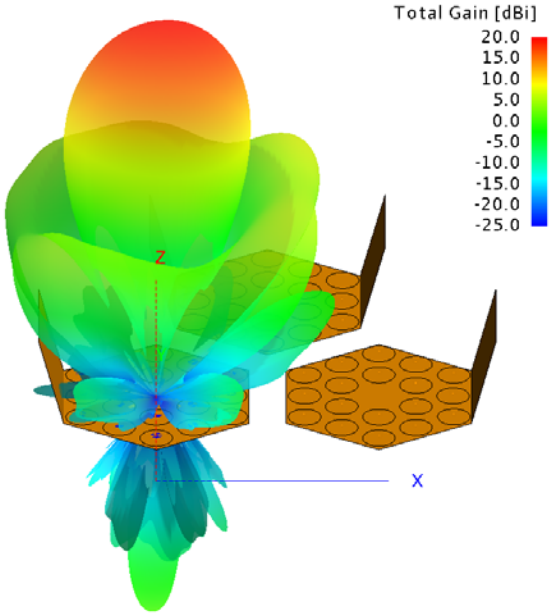

(b)

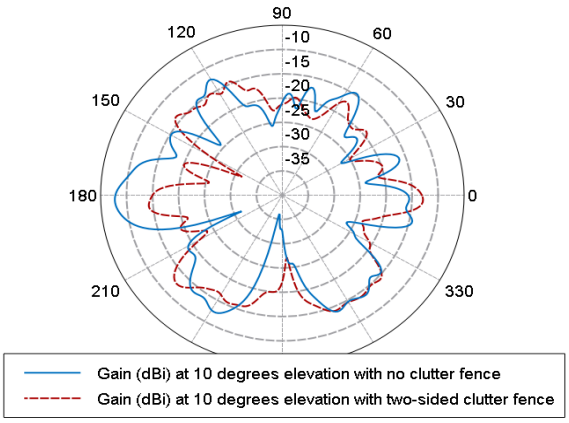

(c)

Figure 4.14. (a) Photo of 3 449-MHz hexagonal arrays with radomes and no clutter fence. (b) Layout of 3 449-MHz hexagonal arrays with clutter fence panels intersecting the H-plane. (c) Gain (dBi) at 10° elevation for an array height of 1m with and without the two sided clutter fence shown in Figure 4.11.

Table 4.1: Three Hexagonal Array Sidelobe level

Configuration	With fence	w/o fence
Average sidelobe level	-37dB	-35dB
Peak sidelobe level	-32dB	-27dB

4.5 Optimal Spacing of Three 18-Element Hexagonal Arrays

An additional important design consideration for the 449 MHz system is the chosen spacing of the hexagonal arrays for both transmit and receive performance. As briefly described in the introduction and elaborated in [9], spaced antenna radar systems depend on cross-correlation of the receiver signals in order to compute horizontal velocities. A cross-correlation at zero lag $c_{12}(0)=0.5$ between signals received on two of the arrays results in optimal Full Correlation Analysis algorithm performance [28]. The performance of the spaced antenna radar is dependent on the transmit and receive beamwidths and the receiver spacing. An antenna constant, a_h, which relates the transmit and receive beamwidths to the wavelength is defined as (from Cohn et al.[9]):

$$a_h = \frac{2\pi\alpha(\theta_T,\theta_R)\theta_T}{\lambda}$$

Where θ_T and θ_R are the first null beamwidths (principal lobe) of the transmit and receive antennas and α is an angular weighting function. The antenna constant a_h is directly related to the cross-correlation at zero lag, $c_{12}(0)$ between two spaced receiver signals by:

$$a_h = \frac{2}{\Delta x}\sqrt{-\ln[c_{12}(0)]}$$

where Δx is the spacing between receivers. Because a higher value of the cross-correlation function c_{12} results in a more accurate velocity determination, it is useful to rearrange this equation for the purpose of antenna array design:

$$c_{12}(0) = \exp\left[-\left[\frac{\Delta x\, a_h}{2}\right]^2\right]$$

This equation shows that a higher cross-correlation function will result from smaller transmit and receive beamwidths and smaller spacing between receiver arrays. Assuming edge-to-edge spacing of the subarrays, a larger antenna will produce a smaller beamwidth, but also result in a higher cross-correlation. Table 4.2 shows the values of these parameters for the existing MAPR system, and the new 3-hexagon and 7-hexagon Spaced Antenna Interferometry (SAI) systems with edge-to-edge spacing. Like MAPR, the 7-hexagon system has the additional benefit of two different length baselines.

Table 4.2: Antenna Parameters

Antenna	**TX BW**	**RX BW**	**a_h**	**Δx**	**$C_{12}(0)$**
3-hexagon (449 MHz)	10°	18°	0.91	2	0.45
7-hexagon (449 MHz)	7°	10-18°	0.64	2	0.68
				3.3	0.31
MAPR (915 MHz)	9°	18°	1.58	0.9	0.59
				1.3	0.35

For proper operation of the system it is desired to place the sub-arrays at a spacing d that results in optimum $c_{12}(0)$ and the lowest sidelobe level near the horizon. Another tradeoff that was explored is whether a larger spacing that decreases the transmit beamwidth will negate this improvement because of the lower cross-correlation function. This tradeoff was simulated with FEKO using both method of moments and the multilevel fast multipole method (MLFMM) [66]. A realistic ground was simulated one meter below the antenna array using a reflection coefficient approximation for a homogeneous half-space in the region $z<0$ with a relative permittivity of 2.59 and dielectric loss tangent of 0.017 for soil. The spacing of the antenna arrays was varied. The FEKO simulation provided the transmit beamwidth and receive beamwidths and $c_{12}(0)$ was calculated using Equation (3). Measurements of $c_{12}(0)$ at three different spacings were taken using the system shown in Figure 4.14(a).

Figure 4.15(a) shows a plot of simulated and measured cross-correlation at zero lag ($c_{12}(0)$) and transmit beamwidth as a function of edge-to-edge antenna spacing. Figure 4.15(b) is a plot of $c_{12}(0)$ and sidelobe level at 10° elevation, as a function of edge-to-edge antenna spacing.

The simulation shows that the optimum spacing for the desired $c_{12}(0)$=0.5 is not achievable, i.e. the arrays would need to overlap. For d=0m, i.e. aligned edges, the cross-correlation is maximized and edge-to-edge spacing is the dominant factor affecting $c_{12}(0)$. Transmit beamwidth affects $c_{12}(0)$ weakly. The effect of transmit beamwidth is seen at the edge-to-edge spacing of 0.4m, where transmit beamwidth decreases relatively, resulting in a larger $c_{12}(0)$. While the best spacing for $c_{12}(0)$ is 0m, the optimum spacing for low sidelobe levels is about 0.45m. Height of the array above the ground mostly affects the sidelobe levels and would not significantly affect $c_{12}(0)$.

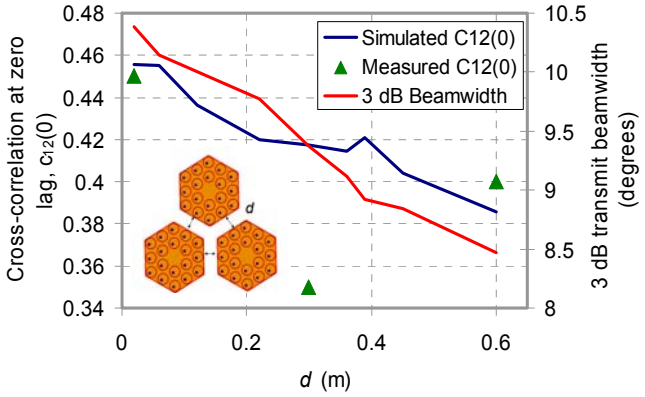

(a)

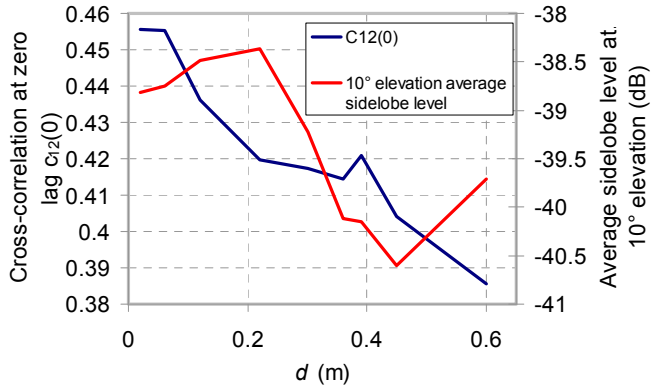

(b)

Figure 4.15.(a) Plot of cross-correlation at zero lag $c_{12}(0)$ and 3 dB transmit beamwidth as a function of edge-to-edge antenna spacing. (b) Plot of cross-correlation at zero lag $c_{12}(0)$ and sidelobe level at 10° elevation (dB down from main beam).

4.6 Discussion and Conclusions

In summary, clutter fence design simulations for the two types of wind profiler radar discussed in this thesis are shown to improve the sidelobe level in order to reduce clutter. The first type of radar is based on beam steering, and a number of existing 915-MHz radars using dual-polarized square patch antennas, such as those presented in Chapter 3, are deployed currently on land and sea. It is found that for a compact clutter fence, there is an optimal angle of the clutter fence sides, and edge treatment of the clutter fence results in lowest sidelobe level.

The second type of wind profiler described in Chapter 2 operates at 449 MHz and is based on the spaced-antenna (interferometer) method using optimized circular patch antennas. In this case, it is found that a clutter fence does not affect the sidelobe level as much, and that edge treatments do not contribute additionally to sidelobe suppression. A clutter fence intersecting the H-plane provides about 5 dB of sidelobe level reduction near the horizon. RF absorber material could be considered for use in addition to the clutter fence, but there are concerns about portability and weather resistance of the material. For good performance at the 449 MHz frequency, the absorber material would need to be at least 45cm thick. This material would not be easy to store and transport. For this modular array, transmit beamwidth, average sidelobe level, and cross-correlation values were simulated as a function of sub-array spacing for the implemented three-hexagon array. It is found that for the three hexagon system, it is not possible to achieve the optimal system cross-correlation parameter, and zero spacing gives the best performance at the expense of non-optimal sidelobe levels. However, it will be shown in Chapter 6 that as the array is scaled and more sub-arrays are added, the system parameter increases and it is possible to choose a sub-array spacing that minimizes the sidelobe level. Ideally, horizontal sidelobe levels would be over 100 dB down from the main beam. Since this is not achievable with a limited antenna size, a compromise is made between antenna size and horizontal sidelobe levels. The results of this chapter will be submitted to the IEEE Transactions on Antennas and Propagation [69].

Chapter 5

Low-Cost 63% Efficient 2.5-kW UHF Power Amplifier

A wind-profiling radar measures weak return signals from variations in atmospheric relative permittivity, and the signal-to-noise ratio (SNR) is directly proportional to transmit power [70]. In the 449-MHz allocated band with a 2-MHz -20dB bandwidth, the maximum transmit EIRP is 110dBm, while received signals are typically on the order of -150dBm. Traditionally, the final PA in the transmitter has been the highest cost of the radar. Commercially available PAs with pulse powers above 2 kW cost upwards of US$30,000 [71,72]. The goal of this work is to develop a low-cost UHF power amplifier using new LDMOS technology.

The power amplifier is the front end of a new wind profiler radar with a unique modular hexagonal antenna design, as shown in Figure 2.1 [47]. The radar pulse is transmitted from all three antennas, but the return signal is received separately on each antenna. This configuration is referred to as a spaced antenna radar, which is an interferometric technique that allows computation of the horizontal wind vector components, while the vertical component is found from the Doppler shift [73]. The hexagonal design allows the antennas to be configured into a 3 (Figure 2.1), 7, or 19 hexagon array. Because it is desired to transmit a higher power level with the larger arrays, multiple 1-kW power modules are combined together in a transmitter.

Radar power amplifiers have traditionally used BJT technology [74,75]. New low-cost LDMOS transistor technology [76,77] makes kilowatt-level pulse amplifier modules possible. A number of different medium (~50W) and high (~1 kW peak) pulse power amplifiers were evaluated for use as a wind profiler radar power amplifier. Initially the Triquint AGR09045E and the Freescale MRF5S9070 were evaluated for use in a distributed amplifier configuration where each element in the array would have a power amplifier module installed directly behind the patch antenna. As higher power (1 kW peak) LDMOS transistors became available, they were considered for use in a single transmitter. This transmitter would amplify a pulse to be split 54 ways to drive each patch antenna. The

transistors evaluated are listed in Table 5.1. The best cost/performance ratio is with the NXP BLF578 with a cost of 20 cents per Watt.

Table 5.1: LDMOS transistors evaluated for use as a wind profiler radar power amplifier

Transistor manufacturer	Part	Vd	Pout	Duty cycle	¢/W	Cost/device	Frequency range
Triquint	**AGR09045E**	**28V**	**45W**	**CW**	**102**	**$46**	**Up to 900 MHz**
Freescale	**MRF5S9070**	**26V**	**80W**	**CW**	**45**	**$35**	**Up to 1 GHz**
Freescale	**MRF6VP41**	**50V**	**1kW**	**20%**	**60**	**$600**	**10-500 MHz**
NXP	**BLF578**	**50V**	**1.2kW**	**20%**	**20**	**$230**	**10-500 MHz**

This work focuses on the use of the low-cost (~$300) NXP BLF-578 transistors [78]. When used in a push-pull configuration, a single module can produce over 1 kW peak pulse power at 10% duty cycle. In the remainder of the chapter, the implementation and characterization of two combined PAs that result in a 2.5 kW peak pulse output with a 63% drain efficiency at peak power is described.

5.1 High Power Amplifier Design

For a CW power amplifier at UHF and microwave frequencies, the best way to design the input and output matching networks is to use computer controlled load pull tuners, such as those made by Focus Microwave and Maury Microwave. At lower frequencies such as 449 MHz however, these tuners are physically large and expensive. For pulsed load pull at kW-level powers, another issue is that arcing in the tuners can occur during measurements.

Manual stub tuners provide another low-cost design method. These tuners are available from Maury Microwave and require manual adjustment of the tuner to create the impedance that results in the best efficiency, output power, and gain. An important consideration when using these tuners is that the insertion loss created by the tuner varies with adjustment position and must be calibrated out. Also, since the tuners are a short circuit stub, a DC bias block must be provided between the transistor and the tuner. An amplifier using the Triquint AGR09045E transistor was designed using this method as shown in Figure 5.1.

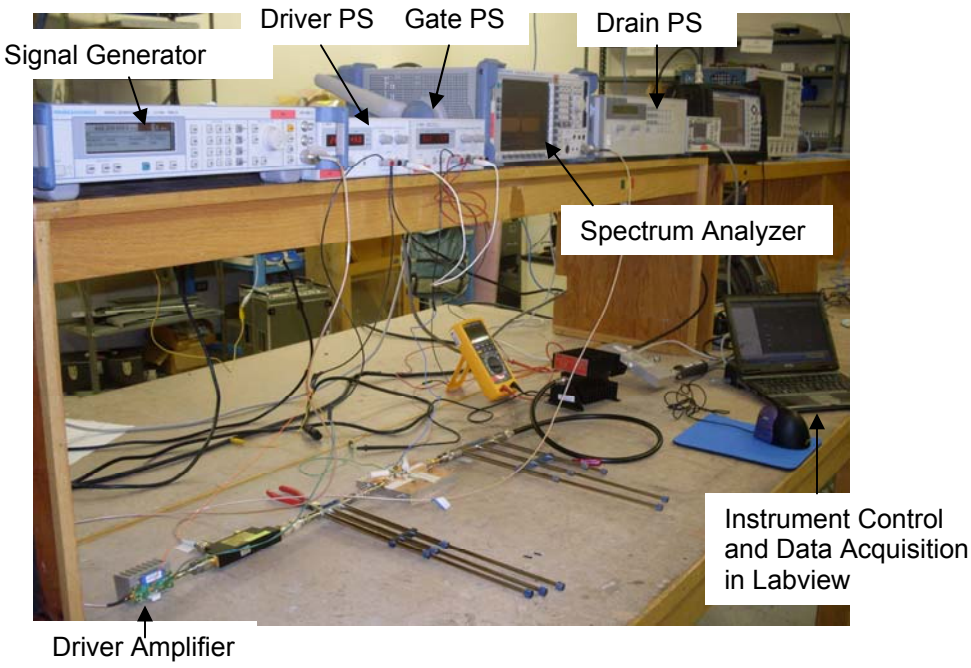

(a)

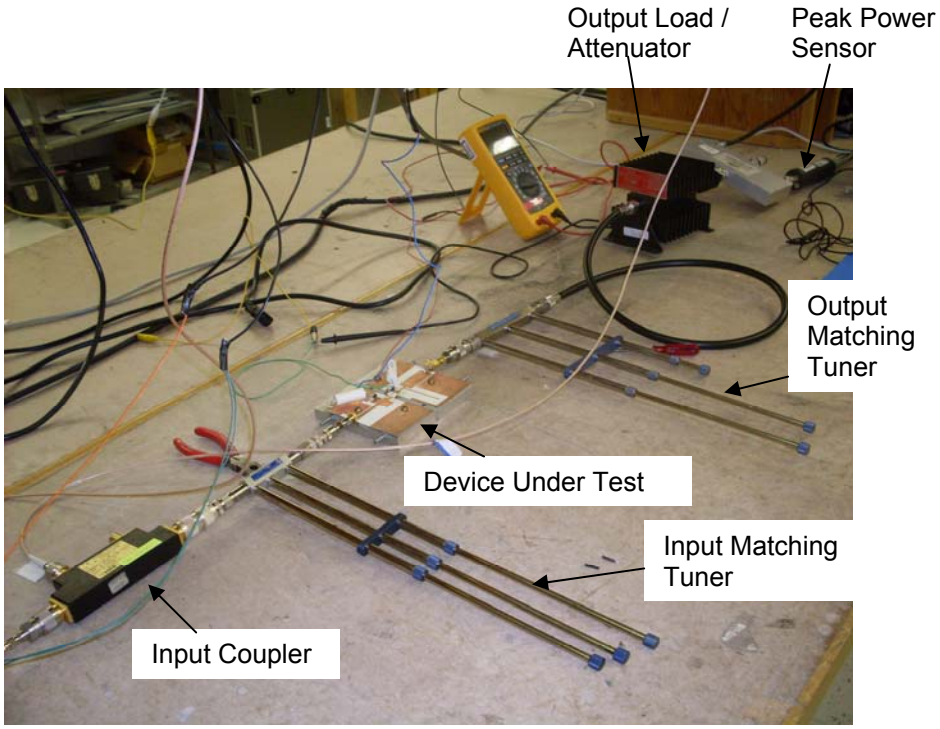

(b)

Figure 5.1.(a) Photograph of the amplifier input and output impedance tuning measurement with an Triquint AGR09045E transistor. (b) Manual stub tuners for this measurement. Length of stub is changed by sliding rod in or out.

The signal generator provides the 449 MHz signal that is amplified by a Sirenza XD010-04S-D4F driver amplifier. The input power level is measured with a directional coupler. A manual stub tuner is connected to the input of the transistor / bias fixture and another tuner connected to the output. The output is connected to a high power load / attenuator. After the attenuator, the output is measured with a spectrum analyzer for oscillations and harmonics and with a peak power meter for output power level. These measurements are recorded along with drain supply voltage and current in order to compute gain and power added efficiency. Power added efficiency (PAE) is defined by the following equation:

$$PAE = \frac{P_{out} - P_{in}}{P_{DC}}$$

When the best tuner configuration is found, the impedance of the tuner is measured with a vector network analyzer. This measured impedance can now be designed into the circuit.

Higher amplifier efficiency can be achieved with a more efficient class of operation. The most common classes of operation are Class-A, B, C, D, E, and F. Each of these classes has a different drain voltage and current waveform combination shown in Figure 5.2 from Raab et al [106]. Efficiency of these amplifier classes can be evaluated visually by observing the overlap of the voltage and current waveforms. More overlap in the waveforms means higher power dissipation in the transistor. While an amplifier may be designed for a particular class of operation, the actual class of operation can be difficult to verify. One method to determine class of operation is to measure the drain voltage waveform with an oscilloscope. At UHF frequencies and above this measurement can be difficult without disturbing normal operation of the circuit.

By sacrificing the linearity of the Class-A mode of operation, higher theoretical efficiency can be achieved. Table 5.2 compares the theoretical efficiency of the common classes of amplifier operation. Note that these values of theoretical efficiency require perfect conditions which are ordinarily not achievable. For example, 100% efficiency in Class-F requires an infinite number of harmonic terminations.

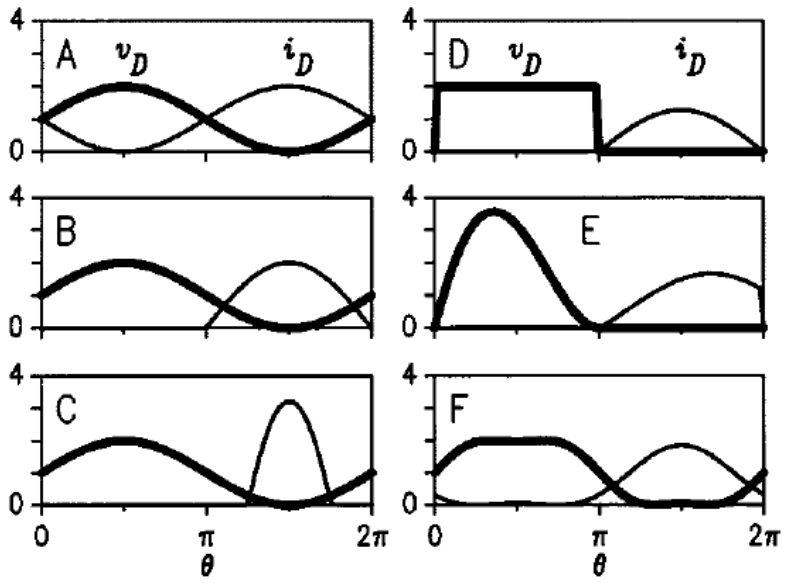

Figure 5.2. Drain voltage and current waveforms for Class-A, B, C, D, E, and F amplifier operation from Raab et al [106].

Table 5.2: Theoretical efficiency of common classes of amplifier operation.

Class of Operation	Theoretical Efficiency
A	50%
B	78%
C	85%
D	100%
E	100%
F	100%

A class-A amplifier has a quiescent current that is half of the maximum current, thus the amplifier has high power dissipation even with no RF drive. Class-B amplifiers are biased at the threshold of conduction, while class-C amplifiers are biased below the threshold of conduction. Class-AB amplifiers have a bias between that of class-A and class-B. Class-D amplifiers use two (or more) transistors to generate square drain voltage or current waveforms. Class-E uses a single transistor with careful design of the drain shunt susceptance and drain series reactance. Class-F uses harmonic resonators in the output matching network to shape the drain waveforms.

The measurements in this chapter assume a class-AB mode of operation with a quiescent current of 40mA. This mode of operation provides some of the efficiency of class-B while retaining some of the gain and linearity of class-A. While operating as a transmitter in a wind profiler radar, the amplifier can also be biased to class-B or class-C to reduce the amount of noise generated by the transmitter between the pulses. The gate voltage can also be actively controlled in order to reduce noise between the pulses but maintain gain and linearity during the pulse.

The NXP BLF 578 considered in this chapter is a package consisting of two transistors, combined in a push-pull configuration, as shown in Figure 5.3(a). Benefits of the push-pull amplifier design include doubling of input and output impedances and reduced even harmonics. The 25-Ω coaxial baluns transform the unbalanced 50-Ω input and output into impedances that are easier to match to the transistor. The baluns at the input and output of the PA have a length that makes them appear as a shunt inductive reactance to the matching network. This prevents unbalanced mode currents from flowing in the outer conductor of the coaxial line and into the balanced circuit. Figure 5.3(b) shows the output matching network of the amplifier.

While manual stub tuners were used for the 45W AGR09045E design described earlier, a simpler way to determine the output matching network is to measure the performance of the amplifier with a power sweep while tuning capacitors in the output matching network. The data from these measurements is shown in Figure 5.4. The capacitance values were varied from 9-20 pF (5% tolerance) while changing the output matching network topology. The best drain efficiency measured in this data is 63% at the 1 dB compression point. The final design for the output matching network determined from these measurements is shown in Figure 5.3(b).

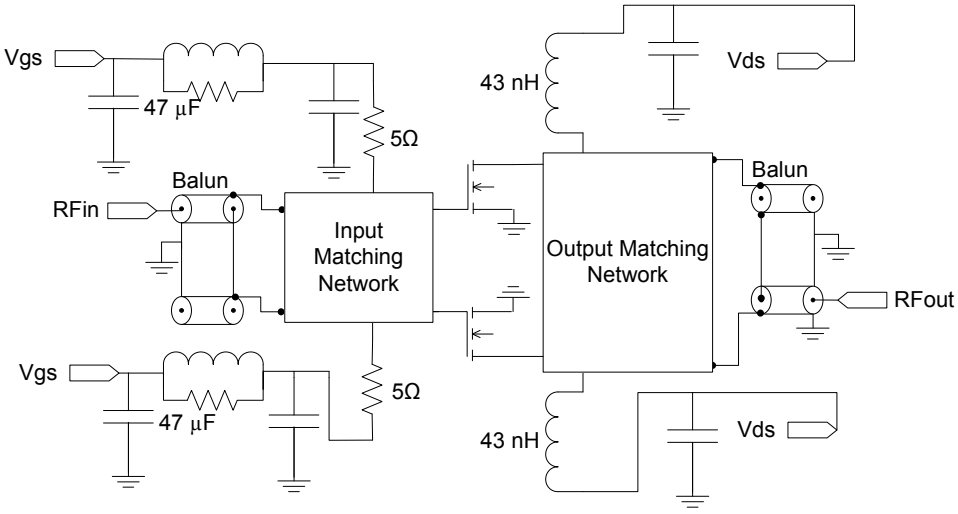

(a)

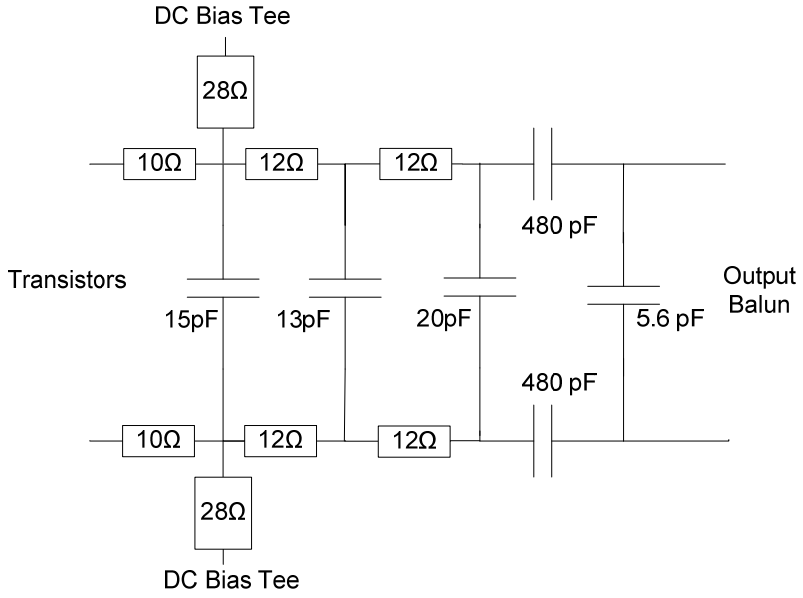

(b)

Figure 5.3.(a) Schematic of the 1-kW transmit PA with push-pull amplifier architecture. Coaxial baluns transform 50Ω input and output into impedances that are easier to match to the transistor. (b) Schematic of output matching network.

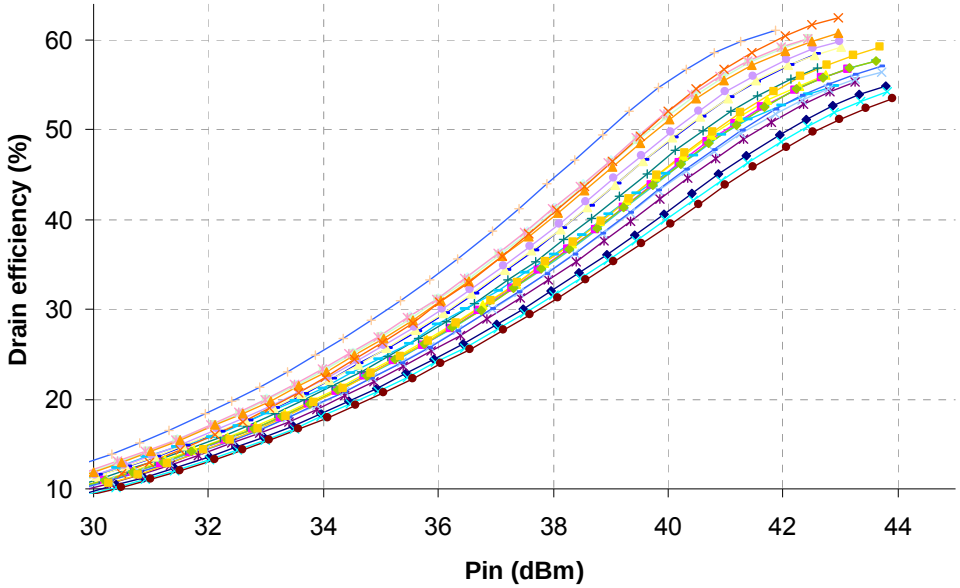

Figure 5.4. Plot of drain efficiency vs. input power for 20 different configurations of the amplifier output matching network. The capacitance values were varied from 9-20 pF (5% tolerance) while changing the output matching network topology.

5.2 1-kW Module Fabrication and Measurements

The amplifier was fabricated on a 30-mil Rogers 4350B substrate (ε_r= 3.5) which is mounted on an aluminum block with a copper insert to transfer heat directly from the transistor package. The NXP BLF-578 device is held in place using a plastic clamp. The fabricated module is shown in Figure 5.5(a). Figure 5.5(b) shows a thermal image of the 1 kW module while in operation. Note that the thermal imager (Fluke Ti10 [79]) assumes a constant emissivity of 0.95. The thermal image shows that there is a potential thermal issue with the output matching capacitors at a temperature of 96°C (the emissivity of the porcelain capacitors is 0.92). While the output matching capacitors have an operating temperature range up to 175°C [80], the use of different output matching capacitors may be necessary for duty cycles above 10-20%.

Two 1-kW modules were tuned by changing values of the output matching capacitors for best and equal gain, output power, and drain efficiency. Measurements were performed by taking a power sweep. A spectrum analyzer is used to monitor harmonics and check for oscillation, while the input can be switched between a signal generator and a Rhode and Schwarz ZVA network analyzer for pulsed large-signal S-parameter measurements. A calibrated high-power driver amplifier and appropriate attenuators are used in the setup.

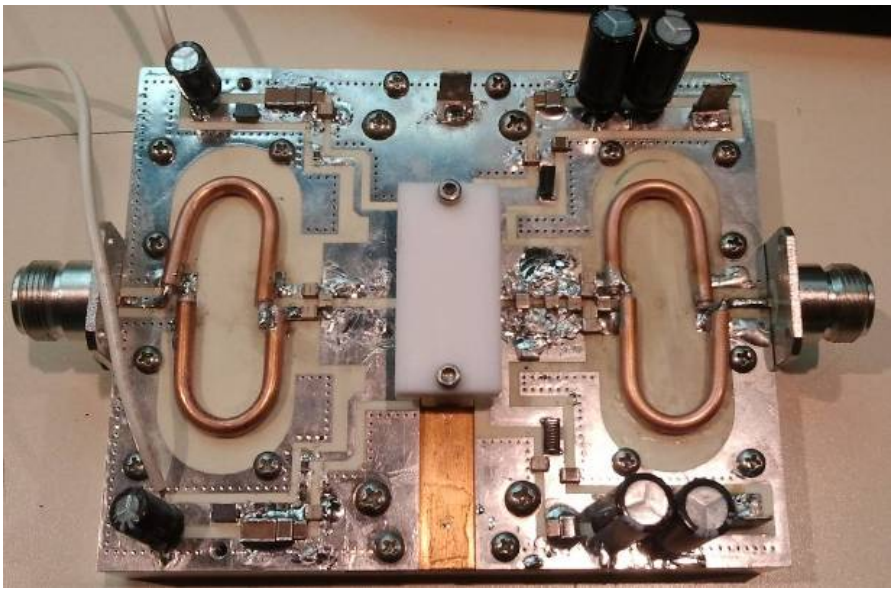

(a)

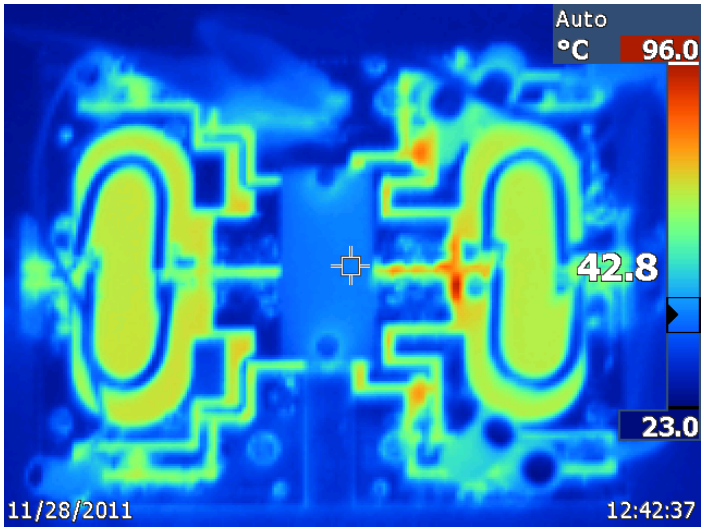

(b)

Figure 5.5.(a) Photograph of fabricated 1 kW module. (b) Thermal image of 1 kW pulse amplifier module using a thermal imager. Output matching capacitors are heating up to 96°C.

Figure 5.6 shows a measurement of the large signal pulsed S-parameters $|S_{21}|$ and $|S_{11}|$ vs. frequency for two 1-kW modules. The S-parameter data shows 18dB gain and $|S_{11}|< -12$ dB. In addition, the S_{21} phase difference at 449 MHz of both amplifiers was measured to be only 9°. Less phase difference between modules will result in higher

combining efficiency. A power sweep up to the 1 dB compression point of the 1-kW modules is shown in Figure 5.7. The best operating point is with P_{1dB} = 61 dBm (1200W), gain = 17.5 dB, drain efficiency = 63%. Note that this module may be referred to as the 1 or 1.2 kW module.

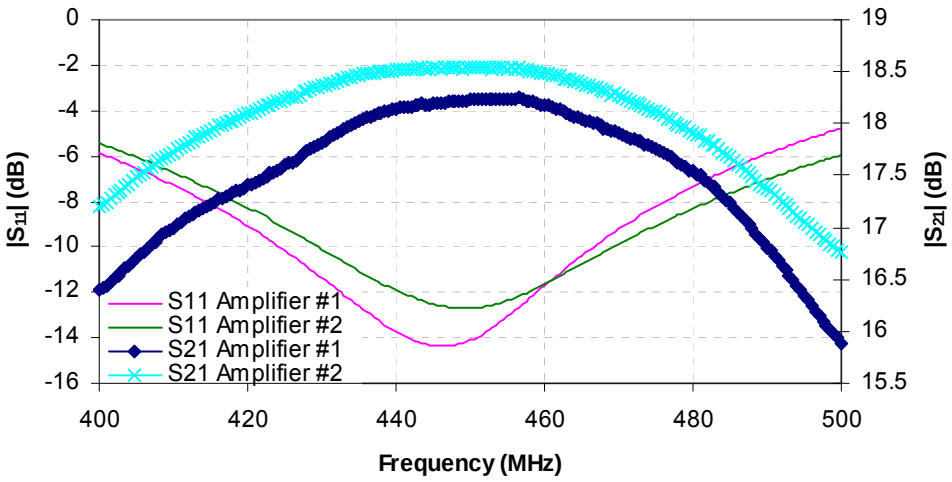

Figure 5.6. S-parameters: $|S_{21}|$ and $|S_{11}|$ vs. frequency for both 1-kW modules biased at Vdd=50V, Idq=40mA, 40A peak drain current and 4A average current.

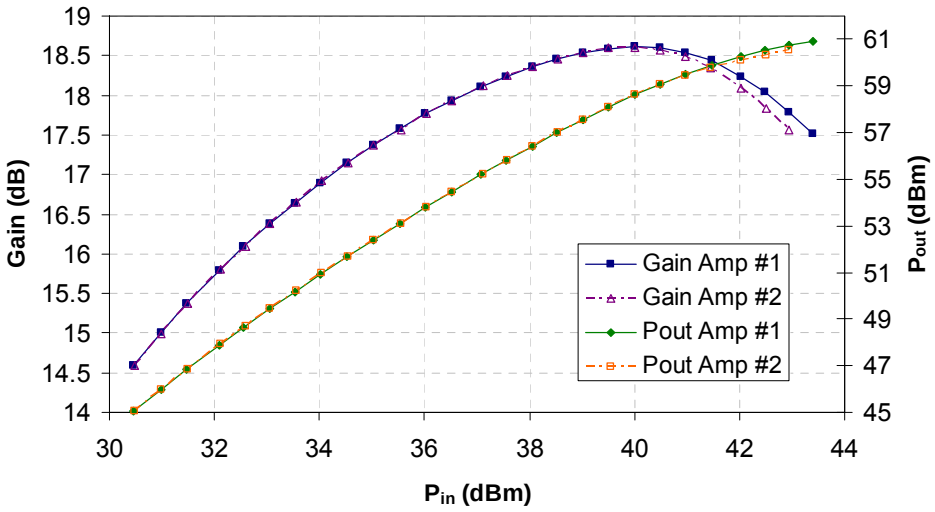

Figure 5.7. Power sweeps for the two 1-kW push-pull PAs. Vdd=50V, Idq=40mA, I_{peak} = 40A, $I_{average}$ = 4A. Best operating point is with Pout = 61 dBm (1200W), gain = 17.5 dB, drain efficiency = 63%.

5.3 Scaling 1-kW Module to Other Frequencies

Since the high power 1-kW transistors from NXP and Freescale can operate in the 10-500 MHz frequency range, the 1-kW module can be redesigned so that it can operate at other frequencies in this range. Operation above 500 MHz would require selection of a different transistor and significant changes to the other circuit elements. At UHF frequencies and higher, circuits can not be designed with the lumped element components used at lower HF and VHF frequencies. Microstrip designs are primarily used at UHF and microwave frequencies. Few changes would be required to operate in the 400-500 MHz range, since this would be within about 10% of the design frequency. These changes would involve tuning the input and output matching networks to maximize gain, output power, and efficiency. Below 400 MHz, more significant changes would be required including redesigns of the bias tees, input and output matching networks as well as the module printed circuit board. Operation at lower frequencies has the advantage of higher gain, higher efficiency, and also the capability of CW operation. For example, the NXP BLF578 can be used as a transmitter in the FM broadcast band (88-108 MHz) with 1 kW CW output power, 26 dB gain, and 75% drain efficiency, Figure 5.8 from [105]. At this frequency, the input and output baluns consist of coaxial lines that are longer in length. The DC bias tees have a different design with 3-turn hand wound wire inductor for the drain bias tee and the gate bias provided through a low value resistor.

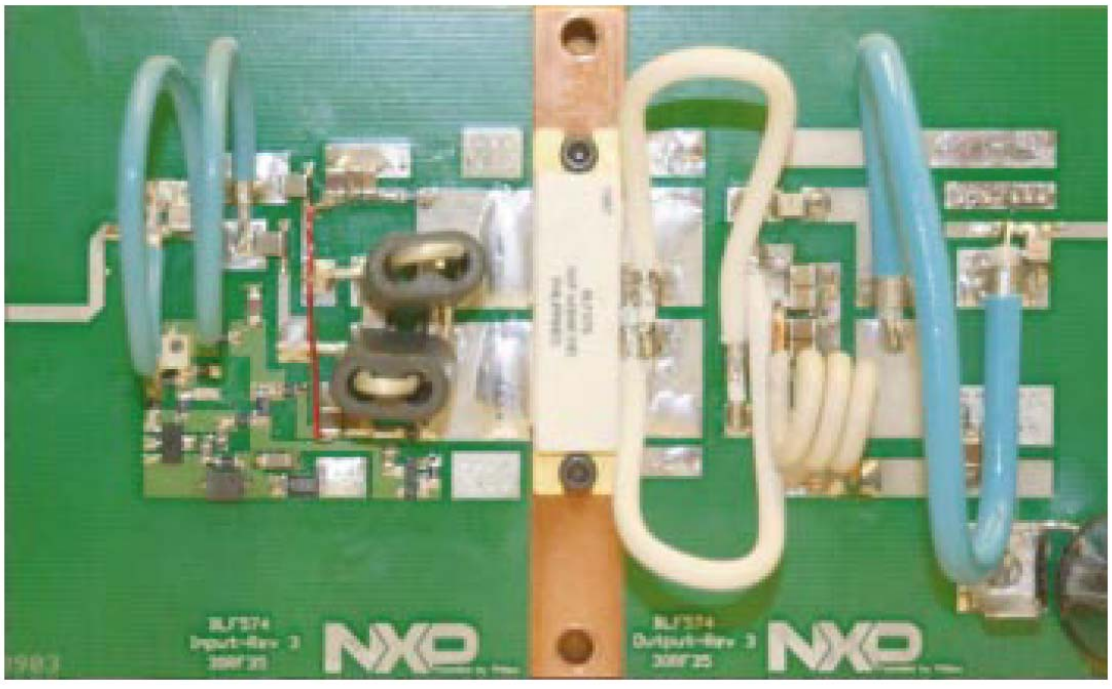

Figure 5.8. NXP BLF 578 transistor used as a transmitter in the FM broadcast band (88-108 MHz) from [105].

5.4 2.5-kW Module Measurements

After making measurements on each amplifier, the two amplifiers were combined with a commercially available 449-MHz reactive splitter/combiner (from RF Hamdesign). Another identical splitter/combiner was used to combine both signals on the output. Each amplifier is clamped to a water cooled heatsink plate.

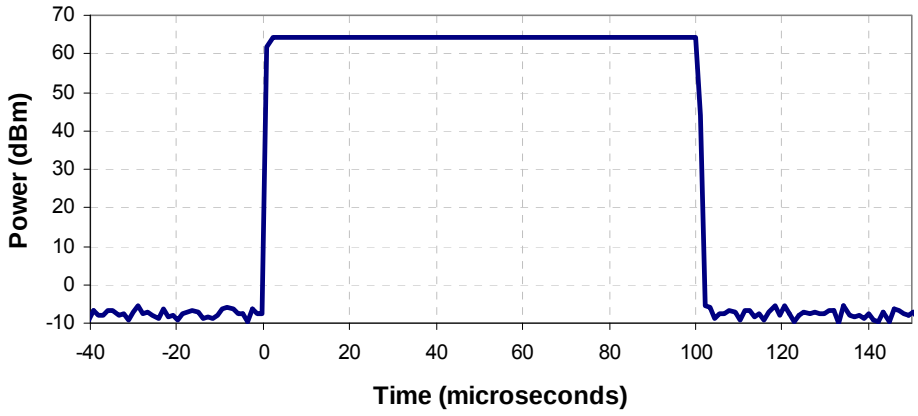

(a)

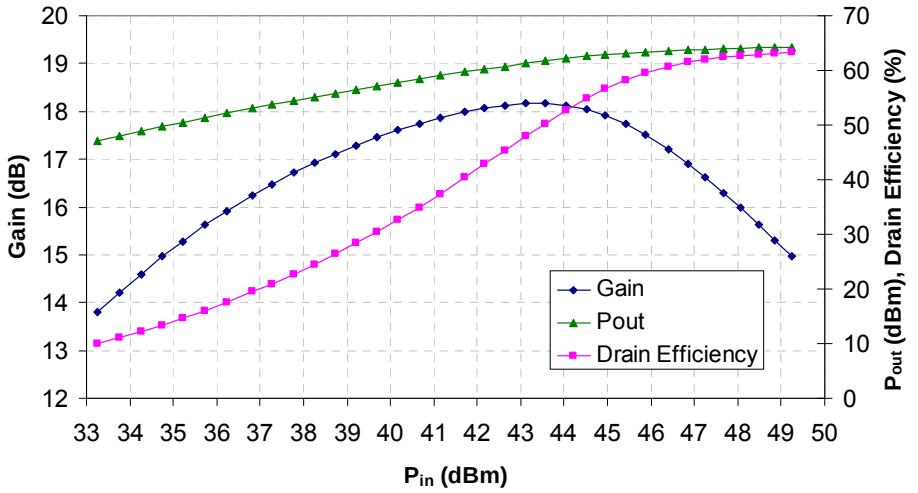

(b)

Figure 5.9.(a) Measured envelope of 2.5 kW amplifier pulse output. A flat pulse top is desirable for best radar performance. (b) Power sweep at 449 MHz for the 2.5 kW amplifier: Gain, Drain Efficiency, and Pout vs. Pin. The P_{3dB} point is 64 dBm (2640W) at the output, with 63% drain efficiency, 15 dB gain, I_{peak} = 83.5A, $I_{average}$ = 8.35A, Vdd=50V, Idq=40mA.

Figure 5.9(a) is a plot of the measured envelope of the combined 2.5-kW pulse output with a 10% duty cycle. For wind profiler radar use, a flat top of the pulse envelope is desired with minimal overshoot or ringing. This measurement is taken with a 100 μs pulse because of instrument limitations, while normal wind profiler radar pulses are 1-4 μs long. Figure 5.9(b) shows a power sweep of the two combined amplifiers. Note that these measurements are taken up to the 3 dB compression point. This measurement is at 449 MHz with Vdd = 50V, and quiescent current Idq = 40 mA. The P_{3dB} point is at 2640W output, drain efficiency is 63%, gain is 15 dB, PAE = 61.74%.

5.5 Conclusions

This chapter demonstrates a 1 kW pulse amplifier module based on LDMOS transistor technology with a parts cost of under US50¢/W. Pulsed large signal S-parameters were measured for each module and confirm an input match with better than -12 dB $|S_{11}|$ and $|S_{21}|$ gain better than 17 dB. Two modules were combined to achieve an output power of 2.6 kW, with 63% drain efficiency, and 15 dB gain. In the future more of the 1-kW modules will be combined for a 10-15 kW transmitter. These amplifiers will be used to power the next generation of 449 MHz wind profiler radars. The results of this work are presented in [67].

Chapter 6

Conclusions and Future Work

6.1 Summary

This thesis presents a new 449 MHz spaced antenna wind profiler radar. A number of aspects of the system are described in this thesis including: system design, antenna design, sidelobe level reduction techniques, high power transmitter design, wind measurements and comparisons to the 915 MHz wind profiler radar. The following topics have been described in this thesis in detail:

(1) The new 449 MHz spaced antenna wind profiler radar antenna design including modularity of the 18-element hexagonal subarrays which can be scaled to a 3, 7, or 19-hexagon array. The system design and horizontal wind computation using Full Correlation Analysis were presented. Optimal receiver spacings were found by simulating the cross-correlation for various 3 and 7-antenna receiver spacing configurations.

(2) High power amplifier designs for a 54% efficient 1 kW (peak, 10% duty cycle) UHF power amplifier with a 57 cents/Watt transistor cost [47] and more recently a 63% efficient 2.5 kW amplifier with a 23 cents/Watt transistor cost [67]. Both of these amplifiers are used sucessfully as a transmitter for the above system.

(3) Measurements of wind and system comparisons using data from the DYNAMO project in the Indian Ocean and the PCAPS project in Salt Lake City, Utah. Wind measurements are taken with the 915 MHz wind profiler during the PCAPS and DYNAMO projects. The 915 MHz wind profiler antenna sidelobe levels are simulated to determine the effectiveness of the clutter fence and edge treatments.

6.2 Future Work

There are a number of possibilities for future work in the area of wind profiler radar.

Increasing the transmit power is in progress. This involves scaling the power amplifiers from Chapter 5 to a 16 kW transmitter using the previously described 1.2 kW modules. Simple low-cost 8-way reactive power combiners are used to combined two 8 kW rack mount modules together into a 16 kW transmitter, Figure 6.1. In the event of a failure, the new ruggedized LDMOS transistors such as the NXP BLF578XR are capable of withstanding a VSWR of up to 65:1.

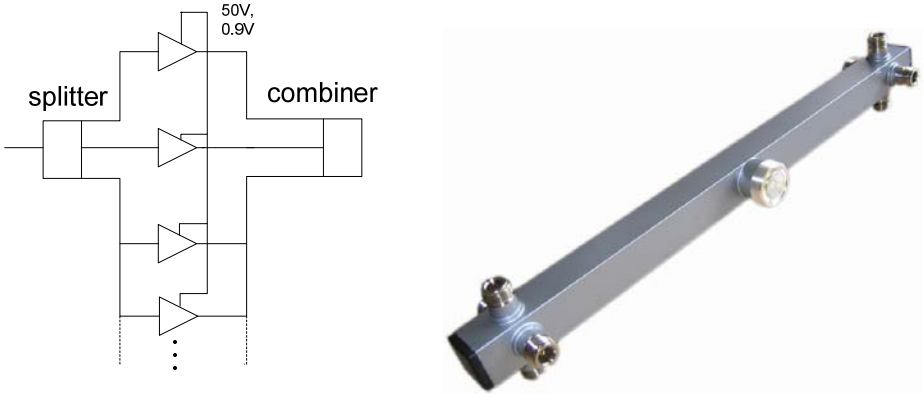

Figure 6.1. Using splitters and combiners, a multi-kW transmitter can be built. Low-cost 8-way and 2-way splitter/combiners will be used to build a 16 kW transmitter.

It is also of interest to increase the array size, to that end, a 7-hexagonal array system is under construction. This system will have 126 elements and use optimized receiver spacing, as discussed below. This system may eventually use the clutter fence that was simulated in Chapter 5 and the hexagons may be positioned at a low height above the ground in order to minimize sidelobe levels. Later implementations of this system may have 19 hexagons (see Figure 6.2).

Since some amplitude and phase variations can be expected across a larger array due to environmental changes, it would be useful to integrate a power amplifier with phase/amplitude adjustment behind each antenna element or subarray (see Figure 6.3). This will require evaluation of individual 1 kW amplifiers for phase stability vs. temperature. An amplitude and phase sensor could be integrated into each patch to sense that the proper amplitude and phase is being transmitted.

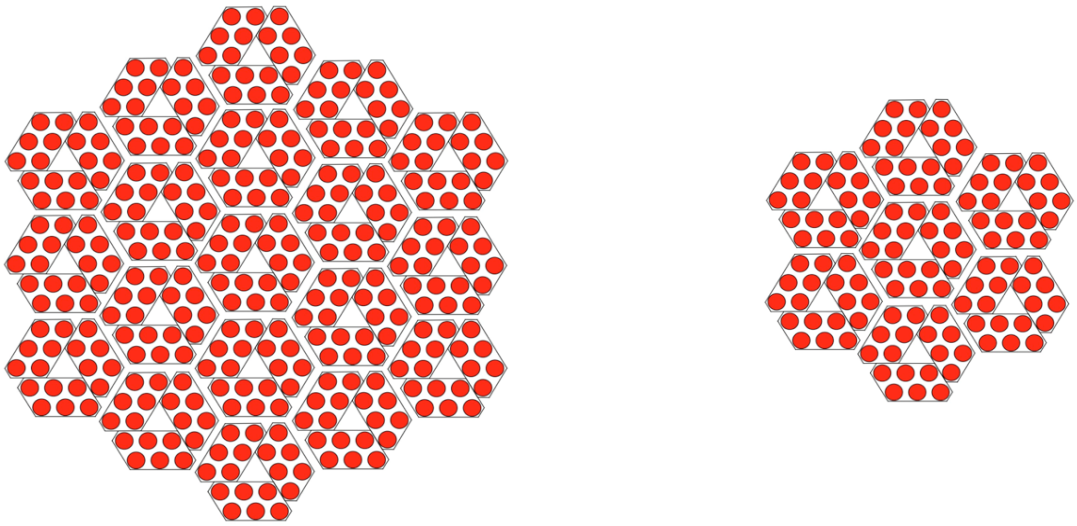

Figure 6.2. Future 19-hexagon (342 element) and 7-hexagon (126 element) systems. With added gain, these will provide altitude coverage up to 15 km and 7 km respectively.

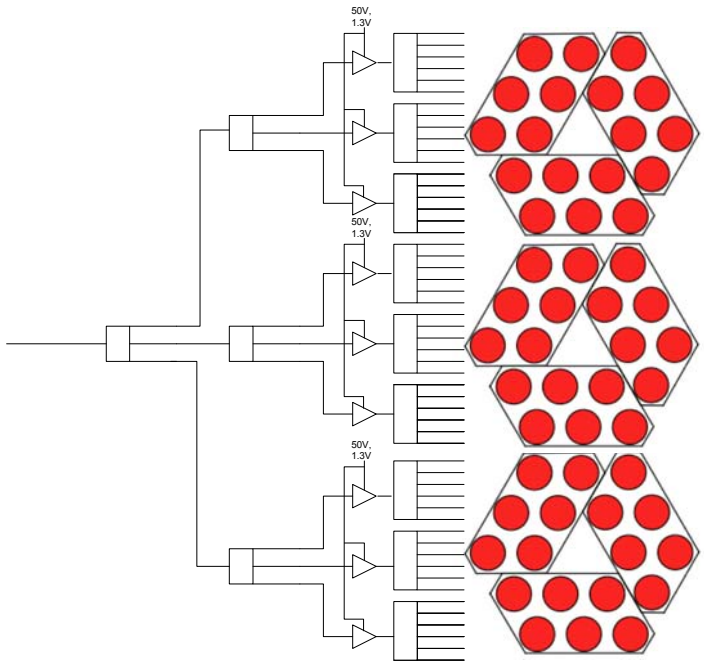

Figure 6.3. Future antenna array feed network showing a transmitter energizing each six-element subarray.

A mobile version of the 449 MHz system mounted on a trailer is planned. This may involve a single hexagon or only involve a group of the six-element parallelograms that make up a normal hexagon. In the case of a single hexagon, a receiver would be dedicated to each 6-element parallelogram subarray.

Designing a ship-based version of the 449 MHz system is also of interest. This is a technical challenge because of the sea clutter and constantly moving ship. There are two solutions to the movement problem. The first solution is a mechanical stabilizer which is currently used for the NCAR 915 MHz ship system. The stabilizer currently used in the NCAR system does not keep up with ship movements. There are newer mechanical systems which can compensate correctly for ship movement. The other solution is an electronic beam steering system which compensates for movements by changing the phase of the elements. This was used on the NOAA Ron Brown wind profiler [14], but was too difficult to maintain and has been decommissioned, a similar idea is now being explored by Detect, Inc.

6.3 Seven Hexagon 449 MHz Wind Profiler Radar

For portable deployable wind profilers, it is of interest to investigate how scaling of the antenna size affects the cross-correlation of spaced-antenna array receiver signals, as well as the sidelobe level. A seven hexagon system built from hexagonal elements identical to those shown in the photograph in Figure 4.5(a) is simulated as a function of sub-array spacing. An earth ground (soil) was also simulated for this case as with the three hexagon radar. Figure 6.5 shows the transmit antenna pattern for this system simulated with FEKO using the full wave MLFMM technique. The antenna has a simulated gain of 28 dBi.

Because each hexagonal array is a separate module that can be positioned independently, optimum receiver spacing was calculated. Because of the smaller transmit beamwidth of the seven antenna array, the cross-correlation between receiver signals is higher, above 0.6, implying that for larger elements of sub-arrays there is flexibility in separation allowing reduction of sidelobes while keeping the optimal system parameter c_{12}. Figure 6.6(a) shows a simulation of cross-correlation at zero lag ($c_{12}(0)$) and 3 dB transmit beamwidth vs. antenna spacing. Figure 6.6(b) shows the cross-correlation at zero lag compared with the average sidelobe level at 10 degrees elevation from horizontal. The beamwidth and sidelobe level were computed using a MLFMM simulation in FEKO while varying the edge-to-edge spacing for each simulation.

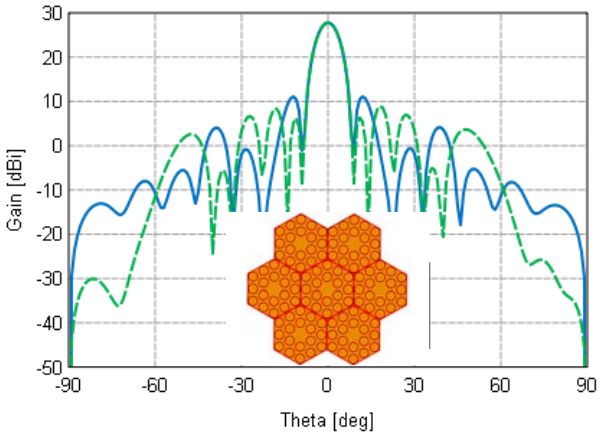

Figure 6.5. Simulated sidelobe levels in the E-plane and H-plane of a 126-element 7-hexagon array with edge-to-edge antenna spacing, shown in inset. The array has a diameter of 5.6m.

Because of the narrow transmit beamwidth, the values of $c_{12}(0)$ are above 0.6 for all spacings. The full correlation analysis method is optimized for $c_{12}(0)=0.5$. Since this value cannot be achieved for reasonable edge-to-edge spacings, the spacing will be optimized for lowest sidelobe level. The spacing simulations show that an edge-to-edge spacing of 0.4m will result in average sidelobe levels at 10 degrees elevation of better than -47 dB down from the main beam gain. These sidelobe levels are 2-4 dB lower than other spacing values. The study of the future seven-hexagon system will be reported in [69].

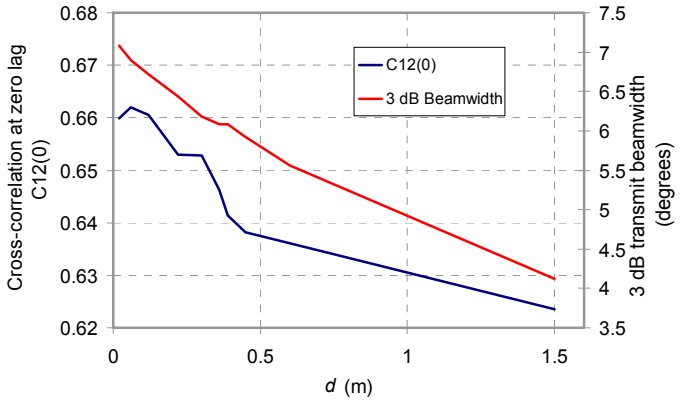

(a)

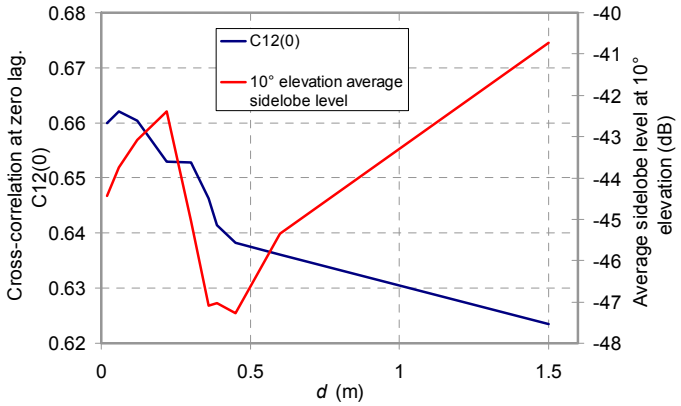

(b)

Figure 6.6.(a) Seven antenna cross-correlation and 3 dB transmit beamwidth as a function of edge-to-edge spacing of the 7-antenna array. (b) Same cross-correlation plot compared with average sidelobe level at 10 degrees elevation.

6.4 Contributions

The following are the specific contributions of this thesis:

- A new 449 MHz wind profiler radar with low sidelobe level modular antenna design. This is the first wind profiler radar using the spaced antenna wind computation method in the 400 MHz frequency bands [47,81-86].

- Sidelobe level reduction techniques for the 915 MHz and 449 MHz wind profiler radars. This is the first systematic study of wind profiler clutter fence and edge treatment antenna improvements using full-wave electromagnetic simulation techniques. Sidelobe reduction by varying height above simulated earth ground (soil) is also studied [69].

- Wind measurements and system comparisons at the Persistent Cold-Air Pool Study (PCAPS) and Dynamics of the Madden-Julian Oscillation (DYNAMO) projects with the 915 MHz wind profiler, 449 MHz wind profiler, radiosondes, and Doppler lidar [47]. Because of observed sea and land clutter in these measurements, they provided motivation for simulations of 915 and 449 MHz antenna sidelobe reduction technques [69].

- Analysis of optimal spaced antenna receiver spacing using full-wave electromagnetic simulation [69]. For the 3-hexagon system, edge-to-edge spacing is optimal because of the wider beamwidth and therefore lower cross-correlation at zero lag ($c_{12}(0)$=0.45). For the 7-hexagon system, the spacing can be optimized for low sidelobe levels because of the narrower beamwidth and higher cross-correlation at zero lag ($c_{12}(0)$=0.6).

- High power amplifier design using a Freescale 50V LDMOS device for a 54% efficient 1 kW (peak, 10% duty cycle) UHF power amplifier with a 57 cents/Watt transistor cost [47]. These amplifiers were successfully used at the PCAPS field project to run the radar.

- High power amplifier design using an NXP 50V LDMOS device for a 63% efficient 2.5 kW amplifier with a 23 cents/Watt transistor cost. This amplifier won first prize in the 2011 NXP High Performance RF Design Challenge at the International Microwave Symposium in Baltimore, MD and is reported in [67]. These amplifiers can be built for about $500 in parts costs compared with

the $30,000 cost of a commercial transmitter. This is one of the first wind profiler radar power amplifiers to use low-cost LDMOS transistors for the transmitter. Previous transmitters have used BJTs. These amplifiers are currently used to run the radar.

In addition, initial research described in Appendix A presents a portable low-cost chip-scale atomic magnetometer with sensitivity of 6 pT/Hz^{-1} and dimensions on the order of a few millimeters with a power consumption of less than 200mW [91,93-97]. This magnetometer was applied to measurement of the heart magnetic field of a mouse [92], which was the first demonstration of a practical measurement using a portable atomic magnetometer.

Appendix A

Mx and Bell-Bloom Atomic Magnetometers and Applications

This chapter presents a survey of Rubidium-87 atomic magnetometer approaches and the underlying principles. Two different Rubidium-87 atomic magnetometer modulation approaches are considered, schemes: Mx and Bell-Bloom. First, the underlying principles are discussed, then the specific Mx and Bell-Bloom experimental setup is described.

A simplified model of an atom used to understand behavior of an atom is called the shell model, which is based on the Bohr model. This model was proposed about 100 years ago, and is somewhat outdated, but it can be useful when thinking about an atom in a hands-on way. This model assumes that electrons have stable orbits at a fixed radius from the nucleus. The electron is contained within a shell at this fixed radius. Figure A.1 shows the shell model for a carbon atom.

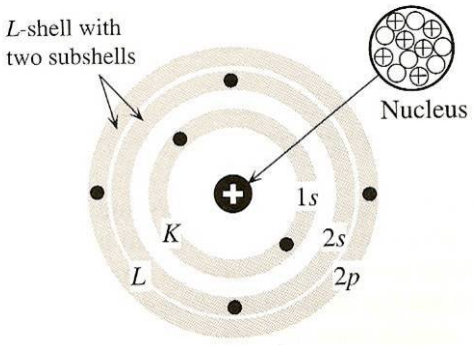

Figure A.1. Historical shell model of a carbon atom (From [87]).

The principal quantum number n characterizes total energy of an electron within an atom. n is an integer with values 1, 2, 3, 4… these values correspond with the K, L, M, and N shells respectively.

Subshells are characterized by the orbital angular momentum quantum number l. Subshells l=0,1,2,3, are labeled s, p, d, and f, respectively, which comes from the historic spectroscopic labels: sharp, principal, diffuse, and fundamental. This quantum number specifies the magnitude of orbital angular momentum of the electron. Figure A.2 is a simplified classical representation depicting the electron orbital angular momentum, the orbiting electron, orbital magnetic dipole moment, and magnetic field B produced by the electron. Note that μ and B are not independent even though they are depicted separately.

The Schrodinger equation predicts the basic observable states at the atomic scale. The solutions to the Schrodinger equation can be characterized by the quantum numbers n, l, and m_l. m_l is the magnetic quantum number, it represents the quantized component of the angular momentum along the direction of an external magnetic field B_z.

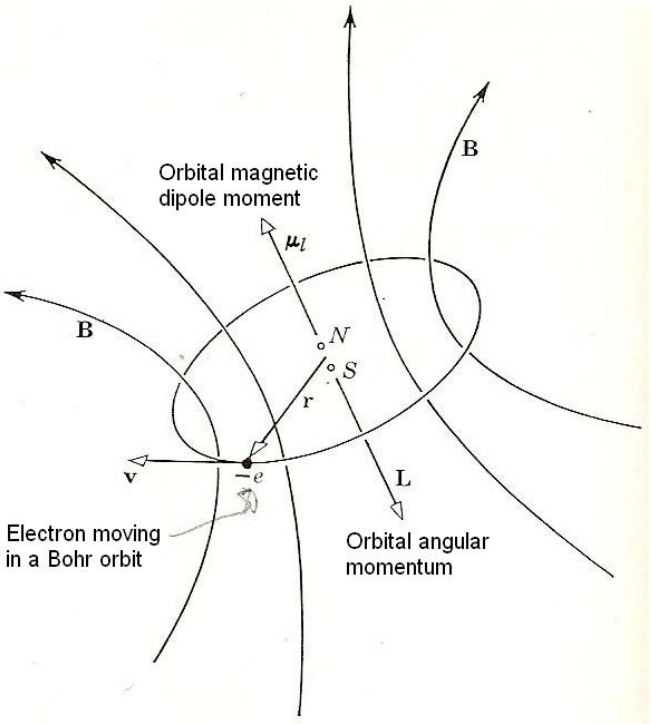

Figure A.2. Diagram of orbiting electron, orbital angular momentum vector, orbital magnetic dipole moment, and magnetic field B produced by the electron (From [88]).

A photon has an angular momentum with a constant magnitude given by ħ. When a photon is absorbed, the electron's angular momentum must change. For simple atoms and E1 dipole allowed transitions, the principal

quantum number n and the angular momentum quantum number l must change following absorption and emission. Selection rules govern which transitions are allowed from one state to another as a consequence of absorption or emission. As a result of absorption or emission:

$$\Delta l = +/- \ 1 \qquad \Delta m = 0,+/-1$$

In addition, the spin angular momentum of the electron is represented by **S**. **S** is a relativistic effect calculated by the Dirac equation. Therefore, the total angular momentum of the electron, **J**, is a vector that is a sum of the orbital angular momentum and the spin angular momentum:

$$\mathbf{J} = \mathbf{L} + \mathbf{S}$$

Another term, **I**, is a vector that represents the total nuclear angular momentum, also called nuclear spin. Nuclear spin is the basis for nuclear magnetic resonance (NMR) spectroscopy. The coupling of total nuclear angular momentum with total electron angular momentum results in hyperfine structure.

Total atomic angular momentum is a vector given by:

$$\mathbf{F} = \mathbf{J} + \mathbf{I}$$

The electron configuration of Rubidium-87 is $1s^2 2s^2 2p^6 3s^2 3p^6 3d^{10} 4s^2 4p^6 5s$. This means there are 37 total electrons, 36 of which are in closed shells and a single electron in the 5s shell. The Rubidium-87 ground state is described in spectroscopic notation as the $5^2S_{1/2}$ state. The form of this representation is $n^{(2\mathbf{S}+1)}l_J$. This means that n=5 and 2**S**+1=2. So the electron spin angular momentum **S**=1/2. Also, l=S, (sharp) which means that l=0 and J=1/2.

For Rubidium-87, nuclear spin I = 3/2. F can take on quantized values between | J + I | and | J – I |. So for J = 1/2, F = 2 or F = 1. The Rubidium-87 D1 hyperfine structure is shown in Figure A.3. The F=1 and F=2 states are the result of naturally occurring interactions between the nuclear spin and the electron angular momentum. Because of naturally occurring thermodynamic interactions, Rubidium-87 atoms have an equal probability of being in the F=1 or F=2 states.

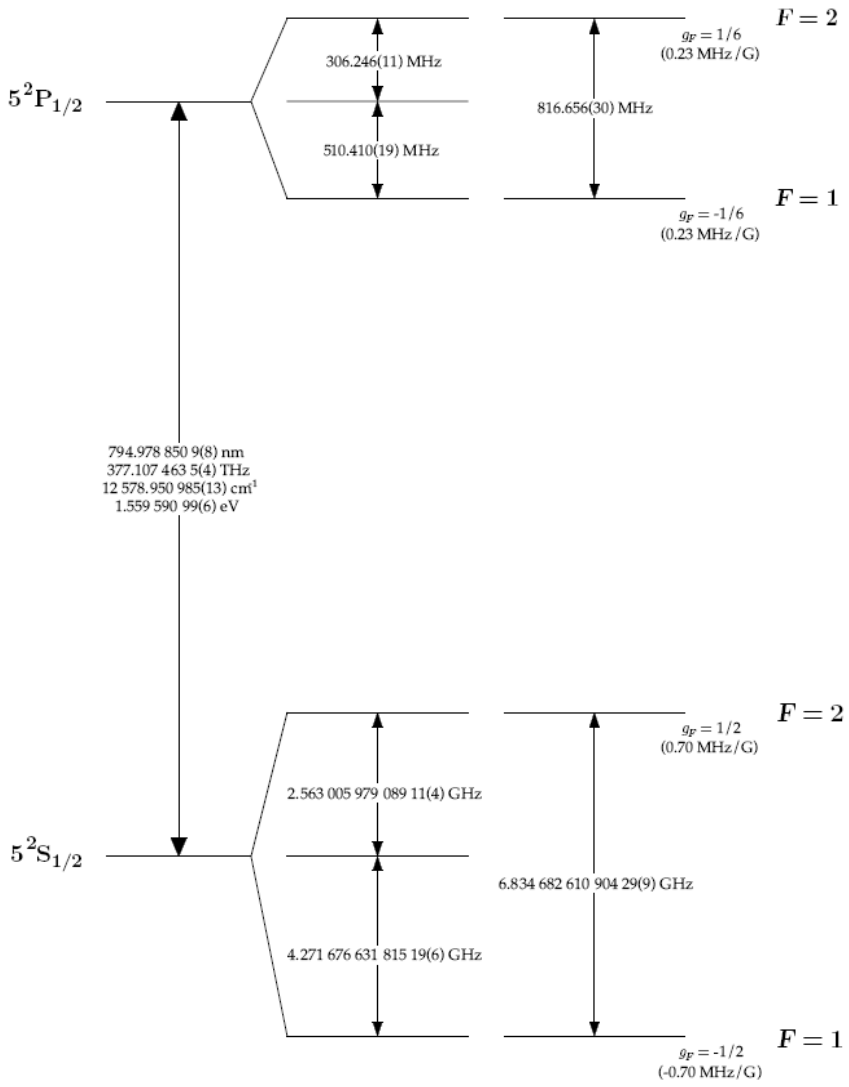

Figure A.3. Rubidium-87 D1 transition hyperfine structure (From [89]).

Because of the quantum theory of angular momentum, the projection of **F** in the z-direction is quantized. In an external magnetic field B_z, the energy of the atoms in this field will be:

$$E = g_l \mu_b \mathbf{B} \cdot \mathbf{F} = g_l \mu_b B F_z$$

Where g_l is the orbital g factor, a dimensionless quantity, and μ_b is the Bohr magneton = 9.274 x 10^{-24} J/T. The Bohr magneton is a unit for measurement of magnetic dipole moments. Since **F** is quantized, the energy will also be quantized.

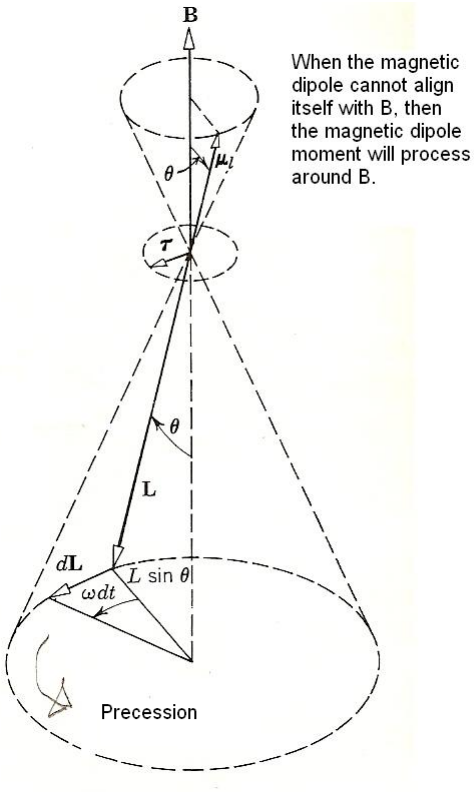

Figure A.4. Diagram illustrating Larmor precession of the magnetic dipole around a magnetic field (From [88]).

Because **F** and m_F are quantized:

$$E = g_l \mu_b B m_F$$

Where m_F has 2F + 1 different values. Therefore, each of the hyperfine states will be split into magnetic sublevels. This dependence on the magnetic field is called the Zeeman effect. When a magnetic field is applied to Rubidium-87, each F state splits into 2F + 1 Zeeman levels. An atomic magnetometer uses these magnetically sensitive sublevels to determine the magnetic field (see Figures A.5 and A.6). There are 2F + 1 Zeeman levels because of the naturally quantized precession rates. Greater angular momentum corresponds to more possible precession rates. It can be imagined that although a spinning top and other natural phenomena appear with the naked eye to have an infinite number of precession rates, it is possible that we are just unable to see the level of detail where the quantization is happening.

The magnetic field applied to the atoms interacts with the magnetic dipole moment. The atomic states will have more or less energy with greater magnetic field because the external field makes the magnetic dipole moment

precess faster (increase of the Larmor precession rate). This corresponds to an increase in orbital angular momentum (see Figure A.4).

There are selection rules that govern a change in the magnetic quantum number. The change in the quantum number depends on the polarization of the photons. Photons with angular momentum of $+\hbar$ are σ^+ polarized (left-hand circular). Photons with angular momentum of $-\hbar$ are σ^- polarized (right-hand circular). It is intuitive that absorption of σ^+ light will increase the level of m by 1 (an increase in angular momentum), while absorption of σ^- light will decrease m by 1 (a decrease in angular momentum).

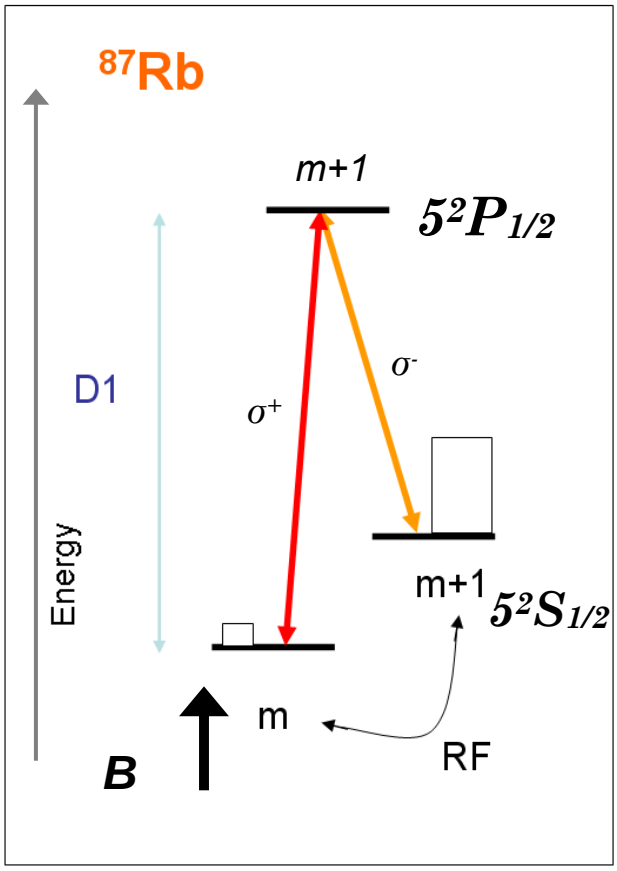

Figure A.5. Circularly polarized light pumps Rubidium-87 atoms, while RF balances the atoms between magnetically sensitive sublevels. This modulates the light for detection with a photodetector.

In an atomic magnetometer, left-hand circularly polarized light pumps the atoms into a higher energy magnetic sublevel. The laser light bandwidth is sufficiently large to pump atoms in all of the magnetic substates. Optical pumping will move atoms into the higher $5^2P_{1/2}$ state, however because the angular momentum of the photon and atom must be conserved, absorption of σ^+ light also requires that m increase by 1. Spontaneous decay will move atoms back into the lower $5^2S_{1/2}$ state within a very short time. A decay is subject to the rules $\Delta m = 0,+/-1$. This results in a pumping of all of the atoms into the highest $5^2S_{1/2}$ magnetic substate, the maximum m level. The magnetic dipole precesses around the applied magnetic field at a rate equivalent to the Larmor frequency.

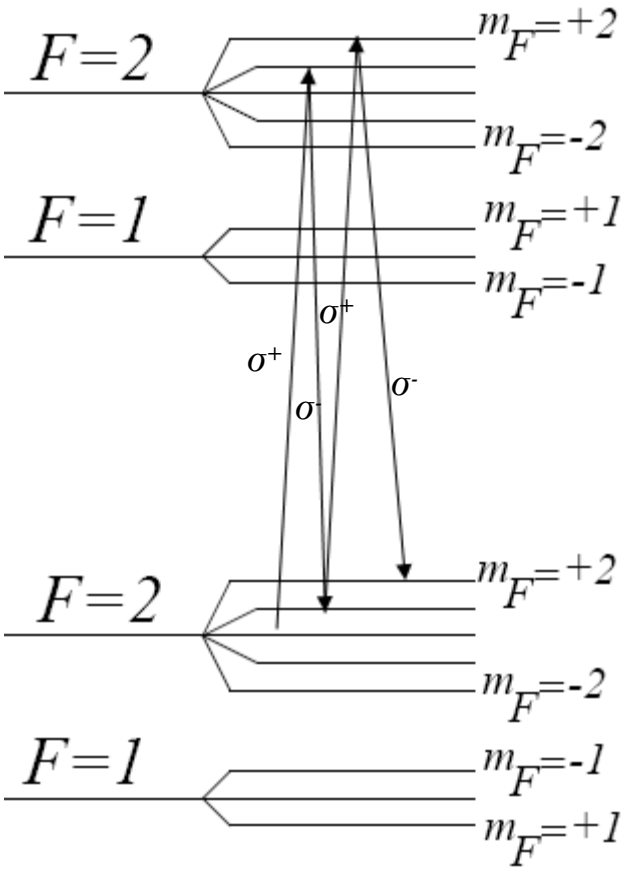

Figure A.6. Rubidium-87 hyperfine structure and magnetically sensitive sublevels. Typical transitions are shown for atoms undergoing optical pumping with σ^+ left-hand circularly polarized light under an applied magnetic field. While $5^2P_{1/2}$ to $5^2S_{1/2}$ decay transitions occur with $\Delta m = 0,+/-1$, because σ^+ light has angular momentum $+\hbar$, only $\Delta m = +1$ is allowed. This results in the atoms being pumped to the F=2, m_F=+2 level.

For the Mx technique, an applied AC magnetic field (RF) at the Larmor frequency of the measured field equalizes the population of atoms between magnetic sublevels. Because the higher energy atoms cannot absorb any more light, they are more transparent than the lower energy atoms. The light will be amplitude modulated at the Larmor frequency in this manner.

To prevent transition to other magnetic substates, collisions between the Rubidium-87 atoms can be limited with a Nitrogen buffer gas added to the vapor cell. The buffer gas has no magnetic substates in its ground state, and is unable to absorb the small levels of energy required for magnetic transitions. This addition of the buffer gas effectively increases the sensitivity of the device.

A.1 Mx Detection

The Mx technique was first described by Bloom [90]. For this technique, the laser frequency is tuned to the center of the optical absorption resonance. The diagram in Figure A.7 illustrates the Mx technique. This laser light is then circularly polarized. The laser light puts some Rubidium-87 atoms into the excited state. The Magnetic field of interest, B, is positioned at a 45 degree angle to the laser beam. An AC magnetic field at the Larmor frequency corresponding to the static B field is applied along the axis of the laser beam:

$$B = h\nu_L/\gamma$$

Where ν_L is the Larmor precession frequency, and γ is the gyromagnetic ratio for Rubidium-87 atoms (7 kHz per microtesla).

For Rubidium-87 atoms, this Larmor frequency can be calculated with the ~7 kHz per microtesla g-factor. As shown in the simulation, the blue AC magnetic field vector equalizes the population of atoms between magnetic substates, so the optical absorption is modulated. Thus, the transmission of light through the atoms is modulated at the Larmor frequency.

One of the consequences of the orientation of the Mx RF coils and the magnetic field of interest is a decrease in sensitivity at angles of 0 and 90 degrees with respect to the sensor. These are called polar and equatorial dead zones.

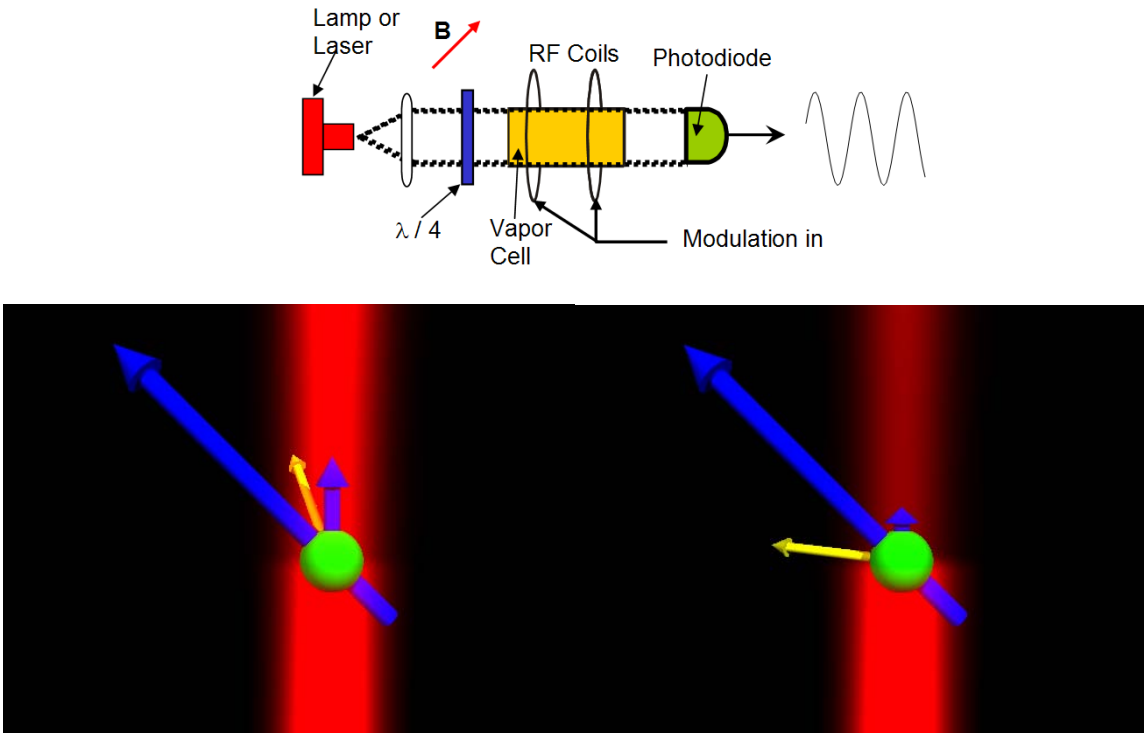

Figure A.7. Diagram illustrating the Mx technique. Simulation of laser light (red) absorption, static magnetic field (blue), AC magnetic field (blue arrow up), precessing atomic spin (yellow).

A.2 Bell-Bloom Modulation

The laser current is modulated for this technique. This results in the frequency of the laser varying on and off the optical absorption resonance. In the Bell-Bloom scheme, instead of an oscillating magnetic field driving the magnetic resonance in the atoms, the frequency modulated laser light drives the resonance, performing the same function as the AC magnetic field of the Mx technique. This creates magnetic field sensitivity similar to Mx.

The magnetic field of interest is perpendicular to the direction of the circularly polarized laser light. A diagram illustrating the Bell-Bloom configuration is shown in Figure A.8.

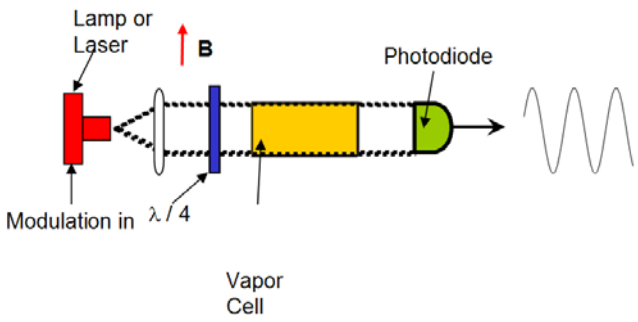

Figure A.8. Diagram of Bell-Bloom operation.

As the magnetic field is swept across the magnetic resonance, a phase shift in the Bell-Bloom modulation is seen. The atoms induce a phase shift in the FM modulated laser light. The phase shift is the result of increased or decreased absorption caused by a change in the magnetic field (Zeeman effect). This can be detected with a lock-in amplifier and the magnetic field value can be determined with high precision for values close to the resonance.

While Bell-Bloom mode is not as sensitive as Mx mode, an advantage to Bell-Bloom is the elimination of the need for an RF coil. In contrast to Mx mode, Bell-Bloom mode only has a polar dead zone. This is advantageous for geophysical applications where the sensor may have changing orientation to the field of interest, such as in an aircraft, or underwater.

A.3 Current Atomic Magnetometer Research and Applications

At the National Institute for Standards and Technology (NIST) in Boulder, Colorado there is active atomic magnetometer research, particularly in the form of chip-scale devices [91]. While commercially available atomic magnetometers have a sensor size of about 5x5x5 cm, the NIST Chip Scale Atomic Magnetometer (CSAM) sensor size is about 1.5x1.5x5 mm. Using MEMS fabrication techniques and a vertical-cavity surface-emitting laser (VCSEL), the size of an atomic magnetometer can be drastically reduced. Figure A.9 shows an example of a Mx mode chip-scale atomic magnetometer that was designed and built at NIST. This magnetometer is based on a chip-scale atomic clock design, with modifications made to allow accurate magnetic field measurement. The small size of the device and its components help reduce the amount of power needed to 194 mW. This is over 10 times less power than a commercial atomic magnetometer.

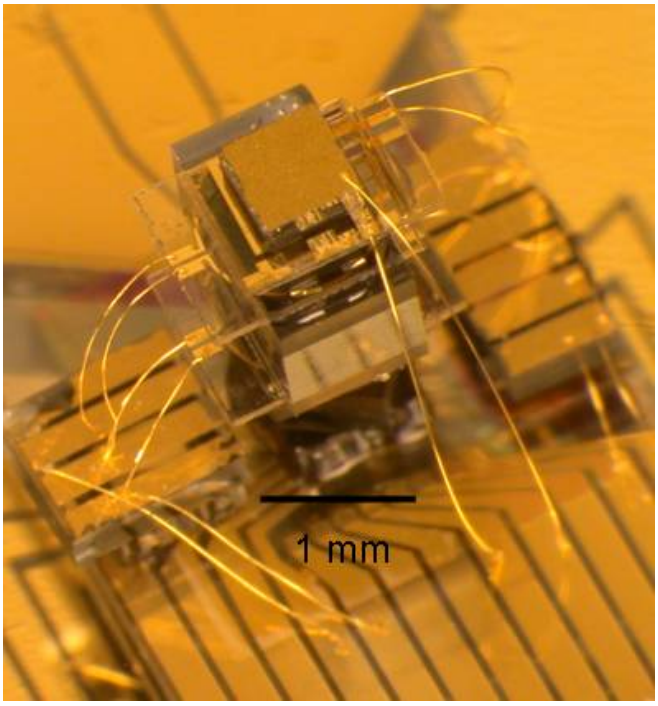

Figure A.9. A Rubidium-87 chip-scale atomic magnetometer designed at NIST and built by the author [91]. All of the optics described in Figure A.7 and quantum physics described in this chapter that are required for an atomic magnetometer are contained in this device with a size of a few millimeters.

The NIST Chip-Scale Atomic Magnetometer (CSAM) uses a VCSEL as the laser light source. This laser produces light at a wavelength that is temperature tunable around 795 nm. The light goes through a quarter-wave plate to produce left-hand circular polarized σ^+ light. This light interacts with Rubidium-87 atoms with Nitrogen buffer gas in a custom fabricated, anodicly bonded vapor cell.

The vapor is heated to improve absorption of the light. One of the challenges is to heat the vapor in a manner that does not produce a magnetic field to disturb the measurement. Heaters for the vapor cell were custom fabricated using Indium-Tin-Oxide, a transparent conductor (see Figure A.10). A thin resistive strip of Indium-Tin-Oxide was patterned into a zigzag pattern using a laser ablation technique. The zigzag pattern increases the resistance of the strip, thereby reducing magnetic field-producing currents. Two zigzag patterned heaters are sandwiched on top of each other in a way that cancels most of the magnetic field produced by the heaters.

The sensitivity of the NIST CSAM in Mx mode is approximately 6 picotelsa/√Hz. One advantage of these atomic magnetometers is their scalar mode of detection, measuring the same value regardless of orientation. The scalar mode of detection makes them ideal for weak signals such as subsurface geological fields or heart magnetic fields.

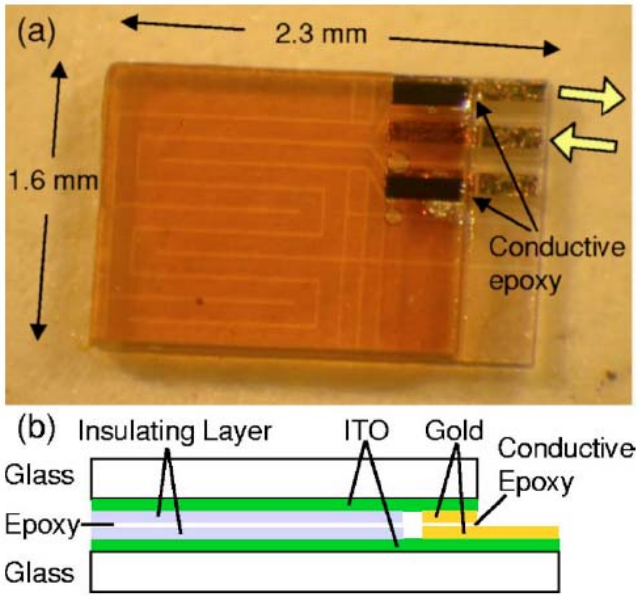

Figure A.10. (a). Picture of the transparent custom magnetic-field-cancelling Indium-Tin-Oxide vapor cell heater. (b). Diagram of heater construction (from [91]).

Current applications for atomic magnetometers include geophysical research and subsurface mapping of objects with magnetic signatures (see Figure A.11). Other future applications being researched include biomedical magnetic field measurement, such as measurement of heart magnetic fields (see Figure A.12).

Figure A.11. Example of subsurface magnetic field measurement using an array of commercial atomic magnetometers. (Geometrics, Inc.)

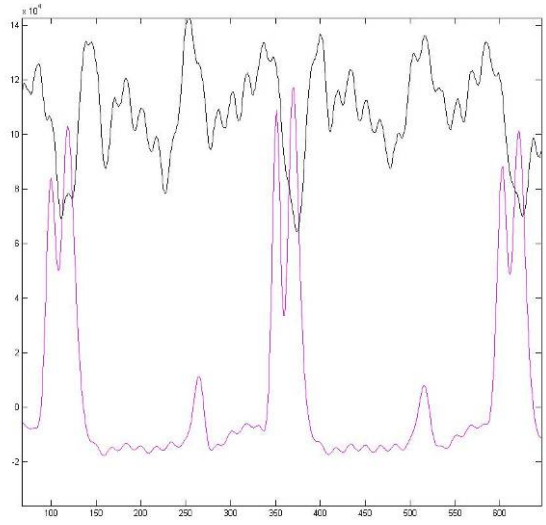

Figure A.12. Mouse heart magnetic field measurement using the CSAM (black trace). The well-known diagnostic tool, heart electrocardiogram, is shown in the pink trace for comparison.

The NIST CSAM was demonstrated by the author as a heart magnetic field sensor at University of Pittsburgh Medical Center in December 2006. Because laboratory mice have the same heart magnetic field waveform as humans, the mouse heart magnetic field was measured. In this experiment, a cover for the device was fabricated to protect the sensor, but keep it as close to the chest of the mouse as possible (within a few millimeters).

The heart magnetic field of the mouse is smaller than the 6 picotesla signals that can be measured in real-time, therefore averaging of the signal was required. Figure A.12 shows the averaged signal as the black trace. The electrical (electrocardiogram, ECG) signal is shown in pink. The magnetic signal averaging was triggered on the ECG signal. The averaged signal shows features with the same period as the ECG. Building on this demonstration, the magnetometer may be developed further to provide a non-invasive method of measuring heart magnetic field activity in addition to the standard ECG.

A.4 Conclusions

This chapter has provided an overview of the quantum physics principles of the Mx and Bell-Bloom magnetometers. It is important to know the principles of many atomic magnetometer operation schemes. This knowledge will allow

the choice of the best scheme for each application. In addition, various applications of atomic magnetometers were discussed. Because of the scalar mode of detection with Mx and Bell-Bloom, it is ideal for subsurface sensing of magnetic materials underground and detection of biological magnetic fields such as the heart magnetic field. New technologies such as MEMS fabrication techniques and microscopic VCSEL light sources have enabled the development of smaller atomic magnetometers with lower power consumption. It is anticipated that the new chip-scale sensors such as the CSAM at NIST could see a large market in years to come.

Appendix B

Full Correlation Analysis Method

In this Appendix, the Full Correlation Analysis method described by Briggs [28] is described. This method uses auto and cross-correlations instead of time delays between channels to compute the true velocity. For any number and arrangement of spaced sensors, the pair *i,j* have an x-component separation of $\xi_{ij,}$ a y-component separation of η_{ij}. The cross-correlation function as a function of relative time shift τ_{ij} is:

$$\rho(\xi_{ij},\eta_{ij},\tau_{ij}) = \rho(A\xi_{ij}^{\ 2} + B\eta_{ij}^{\ 2} + C\tau_{ij}^{\ 2} + 2F\xi_{ij}\tau_{ij} + 2G\eta_{ij}\tau_{ij} + 2H\xi_{ij}\eta_{ij})$$

The maximum value of this function is found by setting $\frac{\partial\rho}{\partial\tau} = 0$. Thus, the time shift for maximum correlation, τ_{ij}' is:

$$\tau_{ij}' = -\frac{F}{C}\xi_{ij} - \frac{G}{C}\eta_{ij}$$

τ_{ij}' is measured, ξ_{ij} and η_{ij} are known, so a linear regression is done to find $\frac{F}{C}$ and $\frac{G}{C}$. Now the time shift τ_{ij} is found at which the mean autocorrelation function averaged over all sensors has the same value. Since τ_{ij} is also measured, a linear regression is used to find the coefficients of the following equation:

$$\tau_{ij}^{\ 2} = \frac{A}{C}\xi_{ij}^{\ 2} + \frac{B}{C}\eta_{ij}^{\ 2} + \frac{2H}{C}\xi_{ij}\eta_{ij}$$

These coefficients can then be used to solve for the x and y components of the velocity using the following equations:

$$AV_x + HV_y = -F$$
$$BV_y + HV_x = -G$$

The degree of anisometry is described by the equation of the characteristic ellipse:

$$A\xi^2 + B\eta^2 + 2H\xi\eta = C{\tau_{0.5}}^2$$

The random changes over time can be described in terms of a "lifetime". This is the time at which the autocorrelation value falls to 0.5, $T_{0.5}$. This is related to the directly observed time at which the autocorrelation value falls to 0.5 by the following relation:

$$T_{0.5} = \tau_{0.5}\frac{C}{K}$$

The coefficient $\frac{C}{K}$ is computed with the following formula:

$$C = A{V_x}^2 + B{V_y}^2 + K + 2HV_xV_y$$

The separation $d_{0.5}^2$ between two sensors at which the correlation falls to 0.5 is given by:

$$\frac{{d_{0.5}}^2}{{T_{0.5}}^2} = \frac{({V_x}^2 + {V_y}^2)K}{A{V_x}^2 + B{V_y}^2 + K + 2HV_xV_y}$$

The above equations form the core of the spaced antenna winds computation. They are implemented in the processing code which generates wind data. Peformance of the spaced antenna method can be quantified by measuring the standard deviation of the wind estimate. Theoretically, the standard deviation of the wind estimate, $\hat{v}_{0x}$ has been shown by Zhang et al.[38] to be influenced as follows:

$$SD[\hat{v}_{0x}] = v_{0x}\left(\frac{\mathrm{var}[\hat{\tau}_p]}{\tau_p^2} + 4\frac{\mathrm{var}[\hat{\tau}_x]}{\tau_x^2}\right)^{1/2}$$

Where $\mathrm{var}[\hat{\tau}_p]$ is the variance of the time lag estimate to the correlation peak given below for an infinite SNR case of Briggs' FCA, and τ_x is the lag at which $|C_{11}(\tau)|=|C_{12}(0)|$.

$$\mathrm{var}[\hat{\tau}_p] = \frac{\tau_c^2}{4M_I}\frac{1-\rho_{12}^2(\tau_p)}{\rho_{12}^2(\tau_p)}$$

Where τ_c is the signal coherence time, M_I is the number of independent signal samples within the dwell time, and $\rho_{12}(\tau_p)$ is the signal cross-correlation coefficient.

$$\mathrm{var}[\hat{\tau}_x] = \frac{\tau_c^4}{\tau_x^2 M_I \rho_{12}^2(0)}\left(1 + \rho_{12}^2(0) - 2\rho_{12}^2(0)\cdot\exp\left(\frac{\tau_x^2+\tau_p^2}{4\tau_c^2}\right)\cosh\left(\frac{\tau_x\tau_p}{2\tau_c^2}\right)\right)$$

The effect of low SNR on the standard deviation of the wind estimate has been studied with another closely related method called Direct-FCA or D-FCA described in Zhang et al.[39] where τ_p and τ_x are estimated directly without assumption of the form of the correlation functions. This method has a different form for τ_p and τ_x estimates that also includes the effect of signal to noise ratio on the variance:

$$\mathrm{var}[\hat{\tau}_p] = \frac{\tau_c^2}{4M_I}\frac{1-\rho_{12}^2(\tau_p)}{\rho_{12}^2(\tau_p)} + \frac{\tau_c^4}{\tau^2 M\rho_{12}^2(\tau_p)}\frac{{P_n}^2}{{P_s}^2} + \frac{\tau_c^2}{M\rho_{12}^2(\tau_p)}\frac{P_n}{P_s}$$

Where τ is the time lag between signals, M is the total number of coherently averaged samples, P_n is the white noise power in the data in Watts, and P_s is the signal power in Watts.

$$\mathrm{var}[\hat{\tau}_x] = \frac{\tau_c^4}{\tau_x^2\rho_{12}^2(0)}\left[\frac{1}{M_I}\left(1+\rho_{12}^2(0)-2\rho_{12}^2(0)\cdot\exp\left(\frac{\tau_x^2+\tau_p^2}{4\tau_c^2}\right)\cosh\left(\frac{\tau_x\tau_p}{2\tau_c^2}\right)\right)+\frac{P_n}{MP_s}(2+\rho_{11}(2\tau_x)-\rho_{12}(\tau_x)-\rho_{12}(-\tau_x))+\frac{{P_n}^2}{M{P_s}^2}\right]$$

These equations give a theoretical analysis for the standard deviation of the wind estimate. In these final equations, the effect of signal to noise ratio on the variance can be directly seen. This is intuitive because the signal energy with a certain SNR that is Doppler shifted because of vertical velocity will contribute the same SNR to the cross-correlation computation. In [39] however it was found that using a multilag local least squares fit (LLSF) estimator for the cross-correlation ratio even in a low SNR condition results in wind estimates that are comparable with the result from a theoretical infinite SNR condition for a two-lag estimator. The best method is subject to debate.

Bibliography

[1] The Ozone Hole Inc., “Atmosphere.” Online, accessed 04/14/11, 2011.

[2] S. G. Benjamin, B. E. Schwartz, S. E. Koch and E. J. Szoke, "The Value of Wind Profiler Data in U.S. Weather Forecasting," *Bull. Amer. Meteor. Soc.,* vol. 85, pp. 1871-1886, 12/01; 2012/05, 2004.

[3] D. Hooper, “Atmospheric Radar Scattering Mechanisms,” MST 12 Radar Conference Summer School Notes, London, Ontario, Canada, May 12, 2009.

[4] R. F. Woodman and Y. Chu, "Aspect sensitivity measurements of VHF backscatter made with the Chung-Li radar: Plausible mechanisms," *Radio Sci.,* vol. 24, pp. 113-125, 1989.

[5] D.S. Zrnic and R.J. Doviak, Doppler Radar & Weather Observations, Academic Press, Orlando, FL, 1984.

[6] W. L. Ecklund, D. A. Carter, and B. B. Balsley, A UHF Wind Profiler for the Boundary Layer: Brief Description and Initial Results. *J. Atmos. Oceanic Technol.*, **5**, 432–441. 1988.

[7] Degreane Horizon Inc, “Wind Profiler PCL 1300” Online, accessed 04/05/11, 2011.

[8] Vaisala, Inc. Wind Profiling, The History, Principles, and Applications, 2004.

[9] S. A. Cohn, C. L. Holloway, S. P. Oncley, R. J. Doviak, and R. J. Lataitis, Validation of a UHF spaced antenna wind profiler for high-resolution boundary layer observations, *Radio Sci.*, 32(3), 1279–1296, 1997.

[10] R. F. Woodman and A. Guillen, "Radar Observations of Winds and Turbulence in the Stratosphere and Mesosphere," *J. Atmos. Sci.,* vol. 31, pp. 493-505, 03/01; 2012/05, 1974.

[11] D.T. Farley, B.B. Balsley, W.E. Swartz, and C. La Hoz, “Tropical Winds Measured by the Arecibo Radar,” *J. Appl. Meteorol*. vol. 18, pp. 227-230, 1979.

[12] S. Fukao, T. Sato, T. Tsuda, S. Kato, K. Wakasugi, and T. Makihira, The MU radar with an active phased array system: 1. Antenna and power amplifiers, *Radio Sci*., 20, 1155–1168, 1985

[13] J. B. Mead, G. Hopcraft, S. J. Frasier, B. D. Pollard, C. D. Cherry, D. H. Schaubert and R. E. McIntosh, "A Volume-Imaging Radar Wind Profiler for Atmospheric Boundary Layer Turbulence Studies," *J. Atmos. Oceanic Technol.,* vol. 15, pp. 849-859, 08/01; 2012/05, 1998.

[14] D. C. Law, S. A. McLaughlin, M. J. Post, B. L. Weber, D. C. Welsh, D. E. Wolfe and D. A. Merritt, "An Electronically Stabilized Phased Array System for Shipborne Atmospheric Wind Profiling," *J. Atmos. Oceanic Technol.,* vol. 19, pp. 924-933, 06/01; 2012/05, 2002.

[15] B. H. Briggs, G. J. Phillips, and D. H. Shinn, The analysis of observations on spaced receivers of the fading of radio signals, *Proc. Phys. Soc. London Sect. B*, 63, 106-121, 1950.

[16] B. L. Weber, and Coauthors, Preliminary Evaluation of the First NOAA Demonstration Network Wind Profiler. *J. Atmos. Oceanic Technol.*, **7**, 909–918. 1990.

[17] W.K. Hocking, P.A. Taylor, P.S. Argall, I. Zawadzki, F. Fabry, G. Mcbean, R. Sica, H. Hangan, G. Klaassen, J. Barron and R. Mercen, " A VHF wind profiler network in Ontario and Quebec, Canada: design details and capabilities", American Meterological Society conference, 2009.

[18] J. Nash, T. J. Oakley, Development of COST 76 wind profiler network in Europe, *Physics and Chemistry of the Earth, Part B: Hydrology, Oceans and Atmosphere*, Volume 26, Issue 3, 2001, Pages 193-199.

[19] V.K. Anandan, D.B.V.Jagannatham, "An Autonomous Interference Detection and Filtering Approach Applied to Wind Profilers," *IEEE Transactions on Geoscience and Remote Sensing*, vol.48, no.4, pp.1660-1666, April 2010.

[20] C-M Gan, Y.H.Wu, B.M. Gross, M. Arend, F. Moshary; S. Ahmed, "A comparison of estimated mixing height by multiple remote sensing instruments and its influence on air quality in urban regions," *Geoscience and Remote Sensing Symposium (IGARSS), 2010 IEEE International*, pp.730-733, 25-30 July 2010

[21] A. Muschinski, V. Lehmann, L. Justen and G. Teschke, "Advanced radar wind profiling," *Meteorol. Z.,* vol. 14, pp. 609-625, 2005.

[22] W.K. Hocking, "A review of Mesosphere–Stratosphere–Troposphere (MST) radar developments and studies, circa 1997–2008," *J. Atmos. Solar Terr. Phys.,* vol. 73, pp. 848-882, 6, 2011.

[23] F. M. Ralph, Using radar-measured radial vertical velocities to distinguish precipitation scattering from clear-air scattering. *J. Atmos. Oceanic Technol*., 12, 257-267.

[24] S. N. Mitra, "A radio method of measuring winds in the ionosphere," *Electrical Engineers, Journal of the Institution of,* vol. 1949, pp. 277, 1949.

[25] O. Røyrvik, "Spaced antenna drift at Jicamarca, mesospheric measurements," *Radio Sci.,* vol. 18, pp. 461-476, 1983.

[26] R. A. Vincent, P. T. May, W. K. Hocking, W. G. Elford, B. H. Candy and B. H. Briggs, "First results with the Adelaide VHF radar: spaced antenna studies of tropospheric winds," *J. Atmos. Terr. Phys.,* vol. 49, pp. 353-366, 4, 1987.

[27] J. V. Baelen, T. Tsuda, A. Richmond, S. Avery, S. Kato, S. Fukao and M. Yamamoto, "Comparison of VHF Doppler beam swinging and spaced antenna observations with the MU radar: First results," *Radio Sci.,* vol. 25, pp. 629-640.

[28] B.H. Briggs, The Analysis of Spaced Sensor Records by the Correlation Technique. Middle Atmosphere Program Handbook, Vol. 13, 1984.

[29] K. Le, R. Palmer, B. Cheong, T.-Y. Yu, G. Zhang, and S. Torres, “On the use of auxiliary receive channels for clutter mitigation with phased array weather radars,” *IEEE Transactions on Geoscience and Remote Sensing*, vol. 47, pp. 272-284, 2009.

[30] V.I. Tatarski, Wave Propagation in a Turbulent Medium, McGraw-Hill, New York, 1961.

[31] K. Wakasugi and S. Fukao, "Sidelobe Properties of a Complementary Code Used in MST Radar Observations," *Geoscience and Remote Sensing, IEEE Transactions on,* vol. GE-23, pp. 57-59, 1985.

[32] A. C. Riddle, L. M. Hartten, D. A. Carter, P. E. Johnston, and C. R. Williams, 2010: A minimum threshold for wind profiler signal-to-noise ratios. Journal of Atmospheric and Oceanic Technology, submitted.

[33] Linear Technology Corp., LTC2255 Datasheet, 2005.

[34] C. L. Martin, W. O. J. Brown, S. A. Cohn, and M. Susedik, Next generation spaced antenna wind profiler technology, 11th Symposium on Meteorological Observations and Instrumentation, American Meteorological Society, 16 January 2001.

[35] P. Chilson, “Spaced Antenna Methods,” MST 12 Radar Conference Summer School Notes, London, Ontario, Canada, May 12, 2009.

[36] G.I. Taylor, “The Spectrum of Turbulence,” *Proc. R. Soc. London A* 164: 476.

[37] D.D. Holm, “Taylor’s Hypothesis, Hamilton’s Principle, and the LANS-α Model for Computing Turbulence,” *Los Alamos Science* 29, 2005.

[38] G. Zhang, R. J. Doviak, J. Vivekanandan, W. O. J. Brown and S. A. Cohn, "Cross-correlation ratio method to estimate cross-beam wind and comparison with a full correlation analysis," *Radio Sci.,* vol. 38, pp. 8052, 03/27, 2003.

[39] G. Zhang, R. J. Doviak, J. Vivekanandan, W. O. J. Brown and S. A. Cohn, "Performance of correlation estimators for spaced-antenna wind measurement in the presence of noise," *Radio Sci.,* vol. 39, pp. RS3017, 06/26, 2004.

[40] F. H. Raab, “Idealized Operation of the Class E Tuned Power Amplifier,” *IEEE Transactions on Microwave Theory and Techniques,* Vol. CAS-24, pp. 725-735, 1977.

[41] T. B. Mader and Z. B. Popovic, "The transmission-line high-efficiency class-E amplifier," *Microwave and Guided Wave Letters, IEEE* , vol.5, no.9, pp.290-292, Sep 1995

[42] T. B. Mader, E. Bryerton, M. Markovic, M. Forman, and Z. Popovic, “Switched-Mode High-Efficiency Microwave Power Amplifiers in a Free-Space Power-Combiner Array,” *IEEE Transactions on Microwave Theory and Techniques*, Vol. 46, No. 10, October 1998

[43] Freescale Semiconductor, Inc., MRF6VP41KHR6 Datasheet, 2010.

[44] International Telecommunications Union, Recommendation ITU-R M.1085-1, Technical and operational characteristics of wind profiler radars for bands in the vicinity of 400 MHz. 1997.

[45] U.S. Dept. of Commerce, National Telecommunications and Information Administration. Manual of Regulations and Procedures for Federal Radio Frequency Management (Redbook), Radar Spectrum Engineering Criteria (RSEC), Section 5.5.5. 2011.

[46] J. Jordan, NOAA, private communication, 2009.

[47] B. Lindseth, J. R. Jordan, D. Law, T. Hock, S. A. Cohn and Z. Popovic, "A New Portable 449 MHz Spaced Antenna Wind Profiler Radar." *IEEE Trans. on Geoscience and Remote Sensing,* vol. PP, pp. 1-10, 2012.

[48] D. Law, NOAA, private communication, 2007.

[49] Ansoft HFSS (High Frequency Structural Simulator) User Guide, Ansys Inc., Canonsburg, PA, 2009.

[50] J. R. James and P. S. Hall, Editors, Handbook of Microstrip Antennas, Peter Peregrinus Press, London, 1989.

[51] B. Lindseth, W.O.J. Brown, S.A. Cohn, J.R. Jordan, D. Law, and T. Hock. “Engineering aspects for the 449 MHz Modular Wind Profiling Network (MPN).” The 12th MST Radar Conference, May 17-23, 2009, London, Ontario, Canada.

[52] B. Lindseth, W.O.J. Brown, S.A. Cohn, J. Jordan, T. Hock, N. Lopez, J. Hoversten, and Z. Popovic. “A New 449 MHz Wind Profiler Radar: Antenna and Amplifier Design,” URSI National Radio Science Meeting, January 6-9, 2010, Boulder, CO.

[53] National Center for Atmospheric Research, “NCAR/EOL/ISS site for CPS” Online, accessed 03/22/11, 2008

[54] University of Illinois, “PLOWS scientific goals” Online, accessed 05/06/12, 2010.

[55] C. S. Morse, R. K. Goodrich, and L.B. Cornman, "The NIMA Method for Improved Moment Estimation from Doppler Spectra", *J. Atmospheric and Oceanic Technology*, 19, p 274-295, 2002.

[56] United States Climate Variability and Predictability (CLIVAR), World Climate Research Program (WCRP), “US CLIVAR Pan American Research: A Science Prospectus and Implementation Plan” Online, accessed 05/06/12, 2000.

[57] NCAR Earth Observing Laboratory, “Dynamo Project Field Phase Interim Progress Report,” Online, accessed 05/06/12, 2011.

[58] C. Zhang, S. Rutledge, R. Johnson, R. Houze, “Experimental Design Overview, Dynamics of the MJO” Online, accessed 04/03/11, 2010.

[59] C.J. Grund, R.M. Banta, J.L. George, J.N. Howell, M.J. Post, R.A. Richter, A.M. Weickmann, High-Resolution Doppler Lidar for Boundary Layer and Cloud Research. *J. Atmos. Oceanic Tech*., 18, 376-393, 2001.

[60] C. A. Russell and J. R. Jordan, "Portable clutter fence for UHF wind profiling radars." in *Preprints, Seventh Symp. on Meteorological Observations and Instrumentation,* New Orleans, LA, 1991, pp. J152–J156.

[61] J. Becker and J. Sureau, "Control of radar site environment by use of fences," *Antennas and Propagation, IEEE Transactions on,* vol. 14, pp. 768-773, 1966.

[62] J. Ruze, F. I. Sheftman and D. A. Cahlander, "Radar ground-clutter shields," *Proceedings of the IEEE,* vol. 54, pp. 1171-1183, 1966.

[63] D. Hill and J. Wait, "Effect of edge reflections on the performance of antenna ground screens," *Antennas and Propagation, IEEE Transactions on,* vol. 21, pp. 230-231, 1973.

[64] J. Becker and R. Millett, "A double-slot radar fence for increased clutter suppression," *Antennas and Propagation, IEEE Transactions on,* vol. 16, pp. 103-108, 1968.

[65] F. Solheim, J. Jordan and J. Wilson, "Antenna system with edge treatment means for diminishing antenna transmitting and receiving diffraction, sidelobes, and clutter," US Patent 5963176, October 5, 1999.

[66] EM Software & Systems-S.A. Ltd., Feko 6.1 User's Manual, 2011.

[67] B. Lindseth, T. Kelly, W.O.J. Brown, T. Hock, S.A. Cohn, Z. Popovic, "Low-Cost 63% Efficient 2.5 kW UHF Power Amplifier for a Wind Profiler Radar," *Microwave Symposium Digest (MTT), 2012 IEEE MTT-S International,* Montreal, Canada, 2012.

[68] A. R. von Hippel, Ed., *Dielectric Materials and Applications*, Cambridge, MA: M.I.T. Press, 1954.

[69] B. Lindseth, W.O.J. Brown, T. Hock, S.A. Cohn, Z. Popovic, "Wind Profiler Radar Antenna Sidelobe Reduction," *IEEE Transactions on Antennas and Propagation*, to be submitted.

[70] S. F. Clifford, J. C. Kaimal, R. J. Lataitis and R. G. Strauch, "Ground-based remote profiling in atmospheric studies: an overview," *Proceedings of the IEEE*, vol. 82, pp. 313-355, 1994.

[71] Delta-Sigma Inc. High power RF amplifiers. 2011(11/25), Available: http://www.111rfpower.com.

[72] AR Inc. AR modular RF amplifier systems. 2011(11/25), Available: http://www.ar-worldwide.com/index.htm.

[73] A. Muschinski, V. Lehmann, L. Justen and G. Teschke, "Advanced radar wind profiling," *Meteorol. Z., vol. 14*, pp. 609-625, 2005.

[74] M. Hanczor and M. Kumar, "12-kW S-band solid-state transmitter for modern radar systems," *Microwave Theory and Techniques, IEEE Trans., vol. 41*, pp. 2237-2242, 1993.

[75] Ji-Yong Park, J. Burger and J. Titizian, "UHF-band long-pulse radar power amplifiers using push-pull and balanced configurations," in *Microwave Symp. Digest, 2007 IEEE/MTT-S International*, 2007, pp. 15-18.

[76] M. Mahalingam, E. Mares, W. Brakensiek, K. Burger and C. L. Hsu, "High power microwave device temperature measurement - methodology and applications for pulsed devices," in *Microwave Symp. Digest, 2007 IEEE/MTT-S International*, 2007, pp. 1189-1192.

[77] S. Hiura, H. Sumi and H. Takahashi, "High-efficiency 400 W power amplifier with dynamic drain voltage control for 6 MHz OFDM signal," in *Microwave Symp. Digest, 2010 IEEE MTT-S International*, 2010, pp. 936-939.

[78] NXP Semiconductors, BLF578 Datasheet, 2011.

[79] Fluke Corporation, Ti10 Thermal Imager Users Manual, 2007.

[80] American Technical Ceramics, 100B Series Data Sheet, 2010.

[81] W.O.J. Brown, S.A. Cohn, B. Lindseth, "The NCAR 449 MHz Modular Wind Profiler Development." Presented at 92nd American Meteorological Society Annual Meeting (January 22-26, 2012). 2012, Available: http://ams.confex.com/ams/92Annual/webprogram/Paper202875.html.

[82] W.O.J. Brown, S.A. Cohn, B. Lindseth, "The NCAR 449 MHz modular wind profiler—prototype deployment and future plans." Presented at 35th Conference on Radar Meteorology. 2011, Available: http://ams.confex.com/ams/35Radar/webprogram/Paper192002.html.

[83] B. Lindseth, W.O.J. Brown, J. Jordan, D. Law, T. Hock, S.A. Cohn, and Z. Popovic. "A 449-MHz Wind Profiler Radar With Low-Cost 2.5-kW Transmitter." URSI National Radio Science Meeting, January 4-7, 2012, Boulder, Colorado.

[84] S.A. Cohn, W.O.J. Brown, B. Lindseth, "A deployable Modular Profiling Network." 15th Symposium on Meteorological Observation and Instrumentation, American Meteorological Society, January 16-21, 2010, Atlanta, GA.

[85] B. Lindseth, W.O.J. Brown, S.A. Cohn, J. Jordan, D. Law, T. Hock. "A new 449 MHz wind profiler radar: evaluation of antennas, amplifiers and capabilities." 34th Conference on Radar Meteorology. American Meteorological Society. October 5-9, 2009, Williamsburg, VA.

[86] W.O.J. Brown, P.B. Chilson, S.A. Cohn, T. Hock, J. Jordan, D. Law, B. Lindseth, R.D. Palmer, M.K. Politovich, T.Y. Yu. "Development of a modular wind profiling network (MPN)." 88th Annual American Meteorological Society Conference, January 20-24, 2008, New Orleans, LA.

[87] S. O. Kasap, Prinicples of Electrical Engineering Materials and Devices, 1997.

[88] R. Eisberg and R. Resnick, Quantum Physics of Atoms, Molecules, Solids, Nuclei, and Particles, 1974.

[89] A. L. Bloom, *Appl. Opt.* 1, 1962.

[90] D. A. Steck, Rubidium 87 D Line Data, 2003.

[91] P. D. D. Schwindt, B. Lindseth, S. Knappe, V. Shah, J. Kitching, L. Liew, "Chip-scale atomic magnetometer with improved sensitivity by use of the Mx technique", *Appl. Phys. Lett.* 90, 2007.

[92] B. Lindseth, P. D. D. Schwindt, J. Kitching, D. Fischer, V. Shusterman. "Non-contact measurement of cardiac electromagnetic field in mice by use of a microfabricated atomic magnetometer." *Computers in Cardiology* 34:443-446, 2007.

[93] J. Kitching, S. Knappe, J. Moreland, L. Liew, V. Shah, V. Gerginov, P. D. D. Schwindt, L. Hollberg, A. Brannon, B. Lindseth, Z. Popovic. Chip-Scale Atomic Devices Based on Microfabricated Alkali Vapor Cells. Lasers and Electro-Optics, 2007 and the International Quantum Electronics Conference CLEOE-IQEC 2007 European Conference on:1-1.

[94] P. D. D. Schwindt, B. Lindseth, V. Shah, S. Knappe, J. Kitching. Chip-scale atomic magnetometer. Lasers and Electro-Optics, 2006 and 2006 Quantum Electronics and Laser Science Conference CLEO/QELS 2006 Conference on:1-2.

[95] B. Lindseth, P. D. D. Schwindt, S. Knappe, V. Shah, L. Liew, J. Moreland, J. Kitching. "A Microfabricated High Performance Magnetometer", Laser Science 2006, Rochester, NY.

[96] P. D. D. Schwindt, B. Lindseth, S. Knappe, V. Shah, L. Liew, J. Moreland, L. Hollberg, J. Kitching. Chip Scale Atomic Magnetometers. Magnetics Conference, 2006 INTERMAG 2006 IEEE International:386-386.

[97] B. Lindseth, P. D. D. Schwindt, S. Knappe, V. Shah, L. Liew, J. Moreland, J. Kitching. "Improved Sensitivity Rubidium-87 Chip-Scale Atomic Magnetometer using the Mx Technique" Contributed Poster, International Conference on Atomic Physics 2006, Innsbruck, Austria.

[98] D. Parsons, W. Dabberdt, H. Cole, T. Hock, C. Martin, A. Barrett, E. Miller, M. Spowart, M. Howard, W. Ecklund, D. Carter, K. Gage, and J. Wilson. "The Integrated Sounding System: Description and Preliminary Observations from TOGA COARE." *Bulletin of the American Meteorological Society*, April 1994.

[99] Bolgiano, R., Jr., The general theory of turbulence: Turbulence in the atmosphere, in Wind and Turbulence in the Stratosphere, Mesosphere and Ionosphere, edited by K. Rawer, pp. 371-400, North-Holland, New York, 1968.

[100] Gage, K. S., B. B. Balsley, 1978: Doppler Radar Probing of the Clear Atmosphere. *Bull. Amer. Meteor. Soc.*, 59, 1074–1093.

[101] S.A Cohn, C.L. Holloway, and R.J. Doviak, 1996: High time-resolution (30-second) wind profiling with the NCAR/ARM MAPR. Abstracts, *Atmospheric Radiation Measurement (ARM) Program Science Team Meeting*, San Antonio, March 1996, 24. [U.S. D.O.C., Springfield, VA 22161]

[102] G. Ochs. Antennas and Propagation Society International Symposium, Vol. 1 pp. 237 – 241, 1963.

[103] J. Röttger, and H. M. Ierkic. Postset beam steering and interferometer applications of VHF radars to study winds, waves, and turbulence in the lower and middle atmosphere, *Radio Sci.*, 20(6), 1985.

[104] Q. Rao, H. Hashiguchi, and S. Fukao, Study on ground clutter prevention fences for boundary layer radars, *Radio Sci*., 38(2), 1030, doi:10.1029/2001RS002489, 2003.

[105] NXP Semiconductor, Using the BLF578 in the 88 MHz to 108 MHz FM band, 2009.

[106] F. H. Raab, P. Asbeck, S. Cripps, P.B. Kenington, Z. Popović, N. Pothecary, J. F. Sevic, N. O. Sokal, Power amplifiers and transmitters for RF and microwave. IEEE Trans. Microwave Theory and Techn., Vol. 50, No. 3, pp. 814-826, March 2002.

[107] R. Harrington, *Field Computation by Moment Methods*, 1968.